

Wayne State University Dissertations

---


January 2019

## Engineering Of Gold Nanoparticles For Drug Delivery

Fangchao Liu

Wayne State University, fb2398@wayne.edu

Follow this and additional works at: [https://digitalcommons.wayne.edu/oa\\_dissertations](https://digitalcommons.wayne.edu/oa_dissertations)

 Part of the [Chemical Engineering Commons](#), and the [Materials Science and Engineering Commons](#)

---

### Recommended Citation

Liu, Fangchao, "Engineering Of Gold Nanoparticles For Drug Delivery" (2019). *Wayne State University Dissertations*. 2286.

[https://digitalcommons.wayne.edu/oa\\_dissertations/2286](https://digitalcommons.wayne.edu/oa_dissertations/2286)

This Open Access Dissertation is brought to you for free and open access by DigitalCommons@WayneState. It has been accepted for inclusion in Wayne State University Dissertations by an authorized administrator of DigitalCommons@WayneState.

**ENGINEERING OF GOLD NANOPARTICLES FOR TARGETED DRUG DELIVERY**

by

**FANGCHAO LIU**

**DISSERTATION**

Submitted to the Graduate School

of Wayne State University,

Detroit, Michigan

in partial fulfillment of the requirements

for the degree of

**DOCTOR OF PHILOSOPHY**

2019

MAJOR: MATERIALS SCIENCE AND  
ENGINEERING

Approved By:

---

Advisor

---

Date

---

---

---

## **ACKNOWLEDGEMENTS**

A special thanks to my advisor, my mentor, Dr. Guangzhao Mao, for her gratitude and kindness during guiding me in my graduate study period. Her insights inspired me both in my career and in my life.

I would like to thank my dissertation committee members, Dr. Guangzhao Mao, Dr. Harry Goshgarian, Dr. Steven Salley, and Dr. Zhiqiang Cao. Their recommendations, suggestions, and criticisms are the only reason I can approach.

I would like to thank Dr. Xiong, Ding, Dr. Yanhua Zhang, Dr. Janelle Walker, Dr. Minic Zeljka, and Dr. Zhi Mei. Without collaboration with them, I cannot achieve those good results.

At the last but not the least, I would like to thank my parents for all the support they provided without any hesitation. And also, to Dr. Lingxiao Xie, thank you for being with me the entire time.

## TABLE OF CONTENTS

<b>ACKNOWLEDGEMENTS</b> .....	<b>II</b>
<b>LIST OF FIGURES</b> .....	<b>VIII</b>
<b>CHAPTER 1 INTRODUCTION</b> .....	<b>1</b>
<b>CHAPTER 2 LITERATURE REVIEW</b> .....	<b>3</b>
2.1 FABRICATION AND FUNCTIONALIZATION OF GOLD NANOPARTICLES (AUNPs) .....	3
2.1.1 Synthesis of gold nanoparticles (AuNPs).....	3
2.1.2 Functionalization and characterization of AuNPs .....	4
2.2 APPLICATIONS OF AUNPs IN BIOMEDICAL AREA .....	7
2.2.1 Photothermal and photodynamic therapy .....	8
2.2.2 Bioimaging and visualization .....	9
2.2.3 Delivery of targeted biomolecules .....	10
2.3 CHALLENGES FOR DRUG DELIVERY USING AUNPs .....	10
2.3.1 Colloidal stability .....	11
2.3.2 Nanotoxicity of AuNPs.....	12
<b>CHAPTER 3 ENGINEERING OF GOLD NANOPARTICLES CAPABLE OF BYPASSING BLOOD-BRAIN BARRIER</b> .....	<b>20</b>

3.1 INTRODUCTION .....	20
3.2 EXPERIMENTAL METHODS.....	23
3.2.1 Materials.....	23
3.2.2 Nanoconjugate Synthesis and characterization.....	24
3.2.3 C2 Hemisection Surgery .....	28
3.2.4 Electromyography (EMG) Analysis .....	29
3.2.5 Nanoconjugate Administration .....	30
3.2.6 Post Procedure Care.....	31
3.2.7 Immunohistochemical Visualization of Nanoconjugate .....	32
3.2.8 Phrenic Nerve Recordings .....	33
3.2.9 Statistical Analysis .....	34
3.3 RESULTS .....	36
3.3.1 Characterizations of AuNP conjugates.....	36
3.3.2 Immunostaining.....	43
3.3.3 Electromyography (EMG) .....	46
3.3.4 Phrenic nerve recordings .....	51
3.4 DISCUSSIONS .....	56

3.5 CONCLUSIONS.....	63
<b>CHAPTER 4 ANTI-CANCER DRUG CONJUGATED NANOPARTICLES INDUCED CELL DEATH IN TRIPLE NEGATIVE BREAST CANCER CELLS .....</b>	<b>65</b>
4.1 INTRODUCTION .....	65
4.2 EXPERIMENTAL METHODS.....	68
4.2.1 Materials.....	68
4.2.2 Synthesis of gold nanoparticle (AuNP) and conjugation of Rad6 inhibitor SMI#9 to AuNP.....	68
4.2.3 Characterization of AuNP–drug conjugates .....	69
4.2.4 Cell lines and culture .....	70
4.2.5 SMI#9 and SMI#9-AuNP uptake and intracellular release of the free drug from AuNP conjugate .....	71
4.2.6 Mitochondrial assay .....	71
4.2.7 LC/MS-MS analysis of SMI#9.....	72
4.2.8 Inductively coupled plasma mass spectrometry analysis of gold .....	73
4.2.9 Statistical analysis.....	73
4.3 RESULTS .....	74
4.3.1 AuNP conjugates characterization .....	74
4.3.2 Intracellular SMI#9-AuNP uptake and releases .....	78

4.3.3 In vivo evaluation of SMI#9 and SMI#9-AuNP .....	81
4.3.4 Biodistribution of SMI#9-AuNP .....	85
4.4 DISCUSSIONS .....	88
4.5 CONCLUSIONS.....	90
<b>CHAPTER 5 SIZE-DEPENDENT TOXICITY OF GOLD NANOPARTICLES.....</b>	<b>91</b>
5.1 INTRODUCTION .....	91
5.2 EXPERIMENTAL METHODS.....	95
5.2.1 Materials.....	95
5.2.2 AuNP Synthesis and Characterization .....	96
5.2.3 Cell culturing and assay study .....	98
5.3 RESULTS .....	106
5.3.1 AuNP characterization.....	106
5.3.2 AuNP size effect on hESC viability .....	108
5.3.3 AuNP cell uptake by hESC.....	110
5.3.4 AuNP effect on hESC pluripotency and differentiation.....	112
5.4 DISCUSSIONS .....	115
5.5 CONCLUSIONS.....	118

<b>CHAPTER 6 CONCLUSIONS .....</b>	<b>119</b>
<b>REFERENCES .....</b>	<b>121</b>
<b>ABSTRACT .....</b>	<b>149</b>
<b>AUTOBIOGRAPHICAL STATEMENT .....</b>	<b>151</b>



## LIST OF FIGURES

- Figure 3-1 Synthesis schematic of transporter protein WGA-HRP and drug THP conjugated to the AuNPs.....28
- Figure 3-2 Characterization of transporter protein and drug-conjugated AuNPs. A) UV-vis spectra measured at room temperature. B-D) TEM images of AuNP conjugates. E-G) Sized distributions of AuNP conjugates.....38
- Figure 3-3 Zetasizer measurements of A) pro-THP nanoconjugates and B) pro-DPCPX nanoconjugates. All samples were measured in PBS buffer (pH=7.4) at 37°C. ....39
- Figure 3-4 TGA data of weight loss for A)MSA-AuNPs, AuNP-pro-THP, and WGA-HRP-AuNP-pro-THP; B) MSA-AuNPs, AuNP-proDPCPX, and WGA-HRP-AuNP-pro-DPCPX.....41
- Figure 3-5 WGA identified in the phrenic nuclei in the cervical spinal cord and rostral ventral respiratory groups in the medulla 72 hours after intradiaphragmatic injection. Scale bar is 50  $\mu$ m. P (in A and E) notes pinhole to mark side contralateral to the injection. ....46
- Figure 3-6 EMG traces 2 days and 14 days post injection 0.7 mg/kg nanoconjugate. Both recordings were obtained from the same rat. A) 2 days post injection of the dose 0.07mg/kg nanoconjugate there is a return of the bursting pattern in the left hemidiaphragm (top trace). The bursts in the left hemidiaphragm match those in the right hemidiaphragm (bottom trace). B) 14 days post injection; the activity has persisted in the left hemidiaphragm (top trace) and remains synchronous with the right hemidiaphragm (bottom trace). In both traces an augmented breath is demonstrated (arrows) followed by a short period of apnea. The augmented breath shows the crossed phrenic pathway is functional. ....48
- Figure 3-7 Percent of Rats with EMG Recovery of the Left Hemidiaphragm. The chart displays the percentage of rats in each group that had an incidence

of recovery detected by EMG of the left hemidiaphragm. Statistical analysis consisted of data from 112 rats. A Chi-square test was performed, and significance was found between the proportions of observations (Yes/No) and the groups,  $\chi^2 (13, N = 112) = 27.075, p = 0.012$ . Treatment with the 0.03mg/kg nanoconjugate resulted in significantly greater (#) incidence of recovery compared to 0.01mg/kg ( $P = 0.015$ ); WGA-HRP-AuNP ( $P = 0.015$ ); and 0.07mg/kg AuNP-proTHP ( $P=0.003$ ). Treatment with the 0.07mg/kg nanoconjugate resulted in significantly greater (†) incidence of recovery compared to 0.01mg/kg ( $P = 0.021$ ); WGA-HRP-AuNP ( $P = 0.021$ ); and 0.07mg/kg AuNP-proTHP ( $P = 0.010$ ). Treatment with the 0.12mg/kg nanoconjugate resulted in significantly greater (‡) incidence of recovery compared to 0.07mg/kg AuNP-proTHP ( $P = 0.029$ ). .....50

Figure 3-8 Day 3 Phrenic Nerve Recordings Analysis. The average percent integrated (AUC) and average percent maximum amplitude (MAX) of the LPN compared to the RPN. Statistical data consisted of neurograms from 18 rats. One way ANOVA showed significant drug effect (#) on day 3 between the 0.12mg/kg dose group and the remaining two groups, 0.03mg/kg dose and 0.07mg/kg dose for the AUC ( $p<0.001$ ). No significance was detected from the MAX. ....53

Figure 3-9 Day 7 Phrenic Nerve Recordings Analysis. The average percent integrated (AUC) and average percent maximum amplitude (MAX) of the LPN compared to the RPN. Statistical data consisted of neurograms from 18 rats. One way ANOVA showed significant drug effect on day 7 for the AUC between the 0.07mg/kg dose and the following; 0.03mg/kg ( $p<0.001$ ), 0.12mg/kg ( $p<0.001$ ), WGA-HRP-AuNP ( $p<0.001$ ), 0.07mg/kg AuNP-ProTHP ( $p<0.001$ ). There was significant drug effect for the MAX between the 0.07mg/kg dose and the following; 0.03mg/kg ( $p=0.013, *$ ), WGA-HRP-AuNP ( $p=0.027, **$ ), 0.07mg/kg AuNP-ProTHP ( $p=0.013, ***$ ). .....54

Figure 3- 10 Day 14 Phrenic Nerve Recordings Analysis. The average percent integrated (AUC) and average percent maximum amplitude (MAX) of the LPN compared to the RPN. Statistical data consisted of neurograms from 18 rats. One way ANOVA showed significant drug effect (#) on day 14 for the AUC between the 0.03mg/kg dose and the 0.12mg/kg dose ( $p=0.030$ ). There

was also significant drug effect (†) for the MAX between the 0.03mg/kg dose and the remaining two doses 0.12mg/kg (p=0.001) and 0.07mg/kg (p=0.049).  
.....55

Figure 4-1 SMI#9-AuNP characterization. A) thermogravimetric analysis. B) UV-vis spectroscopy. C) Transmission electron microscopy. D) Atomic force microscopy (AFM). (a) AFM height of SMI#9-AuNP, Z-range = 5 nm. Inset in panel D(a) shows a white line from where the AFM sectional height profile in panel D(b) was taken and shows 39 nm particle width (two arrows). .....77

Figure 4-2 FTIR spectra of A) chloroform/methanol (11:1, v/v) without (green) and with SMI#9 (red). And of B) SMI#9-AuNP treated and control MDA-MB-231 lysates spiked with parent SMI#9. Arrow indicates nitro banding. ....78

Figure 4-3 LC-MS/MS analysis of SMI#9 release. A) (a) Chemical structures of parent SMI#9 (MW = 366.1), and AuNP-conjugated hydroxymethylated SMI#9 (MW = 396.3). (b) Predicted fragmentation pathway of SMI#9 under the MS condition. (c) Proposed mechanism of SMI#9 release from AuNP conjugate. B) and C) Chromatograms of SUM1315 extracts prepared at 8 or 24 h from untreated (control), or cells treated with blank-AuNP (blank NP), 5 µM SMI#9 (B), or 5 µM SMI#9-AuNP (C, 9-NP). Samples were monitored at m/z 366.69 → 150.1 for SMI#9 (B) or m/z 381.3 → 150.1 for SMI#9 released from AuNP (C). .....80

Figure 4-4 SMI#9-AuNP inhibits TNBC growth. Pharmacokinetic analysis of unconjugated SMI#9 (A) and PEGylated SMI#9-AuNP (B) administered intravenously at 5 mg/kg body weight. C) In vitro activities of SMI#9-AuNP and PEGylated SMI#9-AuNP on SUM1315 cell proliferation. Results are mean ± SD of triplicates from two independent experiments. Tumor volumes (mean ± SEM; n = 6 mice/group) of MDA-MB-468 (D) or SUM1315 (F) xenografts treated with unconjugated SMI#9 (1.5 mg/kg body weight), PEGylated SMI#9-AuNP (0.85 mg/kg body weight), or controls. P < 0.0001 by one-way ANOVA. Vertical scatter plots of excised tumor mass of MDA-MB-468 (E) and SUM1315 (G) xenografts.....84

Figure 4-5 SMI#9 and gold biodistribution analysis. LC/MS-MS analysis of SMI#9 tumor levels and corresponding vertical scatter plots of SUM1315 (A) or MDA-MB-468 (B) excised tumor mass at sacrifice. C) ICP-MS analysis of accumulated gold in the indicated tissue. Data were analyzed by one-way ANOVA and two-tailed Student *t* test; NS, no significant difference. ....87

Figure 5-1 A) TEM images of AuNPs of average core diameters 1.5, 4, and 14 nm; B) DLS measurements of AuNP1.5, AuNP4, and AuNP14 in deionized water; and C) AuNP4 and AuNP14 after incubated with BSA in PBS buffer for 24 hours..... 107

Figure 5-2 Exposure of hESC to AuNPs. A) WA09 hESC cell colonies on MEF feeder layer following 24 h exposure to vehicle, or 10  $\mu\text{g mL}^{-1}$  of AuNP1.5, AuNP4, and AuNP14. Only colonies exposed to AuNP1.5 exhibited altered morphology suggestive of cell death. Arrows indicate MEFs with visible intracellular uptake of AuNPs in the case of AuNP4 and AuNP14. AuNP1.5 was too small to be seen. The scale bar is 160  $\mu\text{m}$  in the bright field microscopic images; B) Cell viability analysis of hESCs exposed for 24 h to 10  $\mu\text{g mL}^{-1}$  of the different sized AuNPs using Trypan blue assay; C) Measurement of mitochondrial activity in hESCs exposed for 24 h to 10  $\mu\text{g mL}^{-1}$  of the different sized AuNPs by the MTT assay. .... 109

Figure 5-3 Uptake of AuNPs by MEFs but not hESCs. A) Cell cultures stained with the nuclear marker DAPI showing the bright heterochromatin foci characteristic of MEFs (long arrows), which allow to distinguish them from hESCs (arrowheads). Uptake of B) AuNP4 and C) AuNP14 was clearly visible in MEFs, but not in hESC colonies (region marked by \*) delineated by dotted lines. D) Uptake of AuNP1.5 by MEFs was only visible following intensification with GoldEnhance<sup>TM</sup> (arrows). The scale bar length in (D) valid for (A)–(C) is 50  $\mu\text{m}$ . .... 111

Figure 5- 4 Characterization of the effects that 14 d exposure to AuNP1.5 (0.6  $\mu\text{g mL}^{-1}$ ), AuNP4 (10  $\mu\text{g mL}^{-1}$ ), and AuNP14 (10  $\mu\text{g mL}^{-1}$ ) has on the capability of hESCs to passively differentiate into cells of the three germ layers. .... 113

Figure 5 5 Formation of embryoid bodies and neural rosettes by control and AuNP-exposed hESCs. .... 115

## CHAPTER 1 INTRODUCTION

Nanoscaled materials are structures with a size of less than 200 nm, and they show different physical and chemical properties compared with their bulk correlatives. Application of Gold nanoparticles (AuNPs) has a long history which can be tracked back to centuries B.C. by ancient scientists.(1) AuNPs are particularly attractive in modern biomedical area due to their versatile surface chemistry, ease of imaging, low toxicity, and engineerability to take advantage of blood-brain barrier transport mechanisms.(2, 3) AuNPs are being widely investigated for sensing, immunoassays, bioimaging for diagnostics, targeted delivery of drugs, genetic materials, antigens, and diagnostic agents.(4) For example, in combination with radiation, AuNPs have proven successful at dissolving deposits of beta-Amyloid, the protein involved in Alzheimer's disease.(5-8) And as a result of the surface plasmon resonance (SPR) effect, AuNPs can have a wide range of excitation upon receiving wavelength from visible to infrared, which gives a great potential of optical applications.(9)

This dissertation described a method of utilizing gold nanoparticles (AuNPs) with various surface modifications in order to adapt various use in

drug delivery systems. The main system involved is a tripartite nanoconjugate consists of drug, targeting protein, and AuNP as vehicle, and the nanoconjugate has been used to treat respiratory malfunction after spinal cord injury and recovery has been obtained after a single intramuscular injection. Besides, this dissertation also described using AuNPs to increase solubility of drugs by conjugating the poorly-soluble drug with AuNPs. The drug-conjugated AuNPs caused cell death and shrink of tumors after administration. This dissertation also discussed the cytotoxicity of AuNPs in biomedical applications. Different sized AuNPs has been tested using human embryonic stem cells (hESCs), and the size-dependent toxicity of AuNPs were observed and discussed.

In chapter 2, a literature review will be presented to show currently used methods of AuNPs fabrication and modification based on different aspects of applications. Then a detailed description of application of AuNPs in biomedical area will be included, and the safety of AuNPs will also be discussed.

Chapter 3 will focus on an engineered nanoconjugates aiming to bringing recovery of respiratory after spinal cord injury in an established animal

model. Various characterization methods were used to determine the composition, size, shape, and stability of the nanoconjugates. And the recovery of breathing was detected based on electromyography (EMG) technique. Dosage optimization were also included in this chapter.

Chapter 4 describes an increase of solubility was introduced by conjugating an anti-cancer drug with AuNPs through chemical bonding. The nanoconjugate were injected locally and cell death were observed.

Chapter 5 describes a size-dependent toxicity study involving AuNPs with core size of 1.5 nm, 4 nm, and 14 nm. All three types of AuNPs were modified with surfactants to achieve better biocompatibility, but a considerable toxicity was observed for 1.5 nm sized AuNPs when treating with hESCs. In the meanwhile, AuNPs with size of 4 nm and 14 nm show no toxicity in this study.

Chapter 6 concludes this work in gold nanoparticle engineering aiming to obtain a biocompatible drug delivery system without introducing toxicity.

## **CHAPTER 2 LITERATURE REVIEW**

### **2.1 Fabrication and functionalization of gold nanoparticles (AuNPs)**

#### **2.1.1 Synthesis of gold nanoparticles (AuNPs)**



With the reduction of gold chloride by phosphorus, Michael Faraday is believed to be one of the first who reported the synthesis of stable gold nanoparticle back in year 1857.(10) Today well established preparation protocols have been developed for AuNPs with various size, shape, and surface modification.(11) With ease of adjusting ratio between gold salt (for example,  $\text{HAuCl}_4$ ), reducing agent, and capping/protecting agent, wet chemical synthesis is mostly used to prepare AuNPs with diameters ranged from  $\sim 2\text{nm}$  to  $50\text{nm}$ .(12-15) Also, a cetyltrimethylammonium bromide (CTAB)-assisted two-step method was raised by Murphy(16) and El-Sayed(17) for gold nanorods synthesis, a seed solution with gold clusters in size of less than  $2\text{nm}$  is used in the first step followed by addition of surfactant CTAB. Besides simple oxidation-reduction based chemical methods, photoreduction, electrochemical synthesis, and plasmon-driven synthesis are also developed.(11) In the mind of “green chemistry”, Mukherjee, P., et al.(18)reported that  $\text{AuCl}_4^-$  ions are reduced by the fungus *Verticillium* sp. to obtain monodispersed AuNPs which was the first report the use of eukaryotic organisms in AuNP biosynthesis.

### 2.1.2 Functionalization and characterization of AuNPs

In the purpose of introducing both biocompatibility and intracellular stability, proper surface functionalization is obviously necessary. Capping ligands including but not limited to thiolates(19), dithiolates(20), amines(21), and carboxylates(21) are all reported in preparation of AuNPs based on different reaction mechanisms(22). Coupled with the binding, the shift of surface plasmon resonance (SPR), change of redox activity, and change of conductivity are observed, which can be used for clinical diagnosis and biosensing.(23-25) By acting as “spacer” and “linker”, thiolated non-toxic long chain polymers such as thiolated polyethylene glycol (PEG-SH) has been used widely with the favor of strong Au-S bonds(26) and flexibility of subsequent functionalization on the other end. However in order to fully take advantage of the Au-S bonding: alkanethiolate-stabilized gold nanoparticles are very stable in aqueous solution as well as organic solvent, a lot efforts have been put in altering the structures of thiolates used to stabilize the nanoparticle surface.(27-31) Besides, serum proteins, for example, bovine serum albumin (BSA), are also proven effective in providing good stability for nanoparticle dispersion in culture medium by forming

protein corona.(32, 33) All the functionalization also contribute to decreasing or/and avoiding toxicity of AuNPs when introduced into physiological models.

The surface modification can not only modify properties of AuNPs, fate of small molecules within physiological environment would also be altered after bonded with AuNPs. Such as CTAB, one of the normally used surfactant in AuNP synthesis, which is cytotoxic while as free molecules, will become nontoxic after binding to gold nanorods.(34) A more practical use of the surface modification is engineering of therapeutic molecule delivery devices. One recent example is that conjugating a small molecule inhibitor SMI#9, which is specific designed for killing cancerous cells, with mercaptosuccinic acid coated AuNPs results in a high therapeutic efficiency combined with good selectivity.(35)

Nanoparticle properties and functionalization completeness can be qualitatively tested by spectroscopy (e.g. IR, Raman, UV-Vis), electron spectroscopy (e.g. TEM, SEM), dynamic light scattering (DLS), thermogravimetric analysis (TGA). However, the disadvantages of these methods are not ignorable. TEM and SEM are having resolution problems especially when experiment was conducted evolving cell samples and ultra-

small sized AuNPs or gold nanocluster.(36) Because of the correlation model it based on, DLS can only be used to measure relative pure spherical particles with narrow size distribution.(37) TGA needs sample amount to be at least 1mg, which is considered a large amount in nano-scale study.

In order to quantify the composition of AuNPs, Rotello, et al. suggested that with a combination of laser desorption/ionization (LDI) and inductively coupled plasma (ICP) mass spectrometry both amount of functional ligands and conjugate stability can be measured. (38) A fluorescence-based method was developed which can be used to quantitatively assess surface coverage and hybridization efficiency of gold films.(39)

## 2.2 Applications of AuNPs in biomedical area

The application of AuNPs has been broaden widely with the development of various detection techniques. This involves detection and photothermolysis of cancer cells, biosensing of both microorganisms and cells, optical imaging, X-ray enhancement, and targeted delivery of various biomolecules. Among these applications AuNPs were used solely or after a conjugation with different compounds.

### 2.2.1 Photothermal and photodynamic therapy

Nanostructures have a higher accumulation among cancerous tissues because of a disordered vessel structure and a porous membrane. This enhanced permeability and retention(EPR) effect has been utilized for passive delivery of nanoparticles for a long time.(40) AuNPs, upon absorption of light with certain wavelength in visible and near-IR region, will heat up rapidly, and as a result, this high temperature will kill the cells around or containing AuNPs. This is the basic concept of photothermal therapy using AuNPs.(41)

Using AuNPs in photothermal therapies is rising great interest especially after combining with laser radiation which offers a better penetration with a limited, controllable damage to cancer cells.(42) This is proved to be promising for effective therapy towards chemotherapy-resistant cancerous types.

Despite the heat created by the absorption of certain wavelength, AuNPs will also undergo a different photochemical mechanism to generate highly reactive radicals, which will also introduce necrosis and apoptosis in

cells. This photodynamic method using AuNPs has been applied to oncological diseases and skin diseases for decades.(43, 44)

The main problems for photonic therapies involving AuNPs are that 1) the colloidal stability of the particles that are used in the methods, and 2) the enhancement of delivery or accumulation of AuNPs in the targeted sites.(45) But it is promising due to the favor of great tunability of AuNPs and the ease of fabrication without using of certain compounds other than the particle itself.

#### 2.2.2 Bioimaging and visualization

Thanks to its high electron density as a heavy metal, gold nanoparticles have a good resolution under transmission electron microscope (TEM) and has been studied since 1970s.(46) High resolution TEM has been used to determine the cellular uptake of AuNP and interactions between AuNP and various biomolecules, microorganisms, and microstructures. However, particularly in biomedical area, optical microscopy methods using AuNPs are becoming more popular recent years.

After combining with label molecules such as fluorescent dye or antibody, penetration and localization of nanoparticles can be monitored at

a real-time style with confocal.(47-49) Especially, with its plasmonic property, AuNP can enhance the contrast of target molecules or structures inside cells result from the multi-photon resonance.(50-52)

AuNPs are also proved to have a higher magnitude comparing with fluorescence under dark-field microscopy because of smaller scattering cross section.(53) After conjugation with antibodies, AuNPs can only bind to cancer cells through an antibody-antigen interaction solely between the nanoconjugates and the cancerous cells, with dark-field microscopy this specific binding can be seen and used to pinpoint cancer cell from normal cell at a single-cell resolution.(54)

### 2.2.3 Delivery of targeted biomolecules

As described above, biomolecules can bind to AuNPs through both chemical conjugation and the binding type can be tuned to be biodegradable or biostable.(55) In most of the study, the biomolecules are anti-cancer molecules, and are proved to be effective thanks to EPR effect.

Other than anti-cancer therapy, AuNP is also a potential candidate for gene therapy after conjugation delivery of genetic materials.(56-59)

### 2.3 Challenges for drug delivery using AuNPs

### 2.3.1 Colloidal stability

AuNPs easily aggregate when encountering with high-ionic-strength environment, and in order to make it biocompatible, colloidal stability of AuNPs should be carefully engineered, considering the physiological condition involves high concentration of salts and a wide range of biomolecules such as proteins and enzymes.

A standard method to guarantee dispersibility, uniformity, and biocompatibility is to use surfactants to modify the surface of AuNPs. Currently thiol compounds such as glutathione, mercaptopropionic acids, cysteine, dihydrolipoic acid, thiolated polyethylene glycol, and their derivatives are considered as the most biocompatible surfactants to be applied to AuNPs.(60-63) The reason is that Au-S bond is more stable than most of the other type of bond between the surface of AuNP and surfactant, and the variability of the thiol compounds is offering possibility of further modification depending on the demand of the conjugate. Even with a good coverage of surfactant, after introduction of physiological condition, the stability of AuNPs will still vary from case to case, and there has not been a



standardized investigation of the colloidal stability of AuNPs in commonly studied aqueous environment.

### 2.3.2 Nanotoxicity of AuNPs

As a well-established yet highly active area, AuNPs are being widely used as imaging enhancer, therapeutic agents alone by themselves, and engineered targeted delivery carriers for drugs, oligonucleotides, antigens, and diagnostic agents.(4, 64-67) AuNP has also been used in consumer market for decades considered non-toxic and inert same as its bulk compartment. Both scientific research and marketing field have an urgent need for systematic nanotoxicity assessment concerning influence of AuNPs on human health.

Cytotoxicity assessment has been one of the most active area considering the amount of various of products applied into market especially those related with human health. *In vitro* assays haven been proven to be commonly used due to ease of reproducing, refining, and replacing.(68, 69) Here we briefly summarized several assays that are used in standard *in vitro* toxicity evaluation experiments based on different mechanisms.

#### 2.3.2.1 Cell growth inhibition

A very obvious and straightforward result after inducing analyte for toxicity assessment is change of cell growth speed, and/or cell death. By comparing cell counts between different treatments the influence of analyte can be evaluated. Both live cells counting methods such as hemocytometry and colorimetric assays are used. Well established assays such as the 3-(4,5-dimethylthiazolyl-2)-2,5-dephenyltetrazolium bromide (MTT) based on the reduction of tetrazolium dye by cellular mitochondrial dehydrogenase present only in viable cells, the purple formazan product is soluble under intracellular environment and is easy to be quantified by photometry. Similar assays utilizing tetrazolium dyes such as XTT, MTS and the WST-1 are all ready-to-use assays for cell viability and toxicity study via monitoring enzymatic activity of mitochondrial.(70) Another method, sulforhodamine B (SRB) assay, based on measuring cellular protein content can also provide comparable sensitivity coupled good reproducibility.(71)

#### 2.3.2.2 Membrane integrity lost

Toxicity inducing may also include membrane interfering which may result in permeability change and compound leakage. Among dye exclusion assays, trypan blue is commonly used which can only be uptaken by

nonviable cells lacking membrane functions.(72) The blue color staining by trypan blue can differentiate the viable cells from the dead and a subsequent cell counting can evaluate the viability quantitatively.(72, 73) Another reliable and simple assay is lactate dehydrogenase (LDH) leakage method. The intracellular loss of LDH and resulting leakage is an indicator of membrane dysfunction and measuring the activity of extracellular LDH can be used to assess the status of cells.(74)

#### 2.3.2.3 Metabolic activity decreasing

Cell metabolism can be also indicated by the concentration of either Adenosine triphosphate (ATP) or certain protein. ATP is playing a role in all metabolically activity inside cells. The bioluminescent assay can quantify ATP concentration using luciferase.(75) Enzymes are important in regulation gene expression, metabolic activity, and gene variation, such as Cytochrome P450.(76) Both common enzyme-linked immunosorbent assay (ELISA) and gel electrophoresis are used testing CYP450s.(76)

#### 3.3.2.4 Epigenetic affects

How cells express genes are obviously important in cell viability, and the change of gene expression is altered by epigenetic change.(77) Although

epigenetic change is natural, it is also affected with inducing of certain toxic materials such as gold nanoparticles.(36) Global DNA methylation status can be determined by immunoprecipitation based colorimetric assays.(36)

Most of *in vitro* assays are using immortalized cell lines or mature cell lines, this makes it difficult to correlate the results from cancerous cells or animal cells to healthy, human cells. The specificity of targets needed for each assay also increases its uncertainty when disruption of membrane and/or mitochondria may be caused by the particle induced. On the other hand, to avoid ethic issue and high expense, experimental cell lines and animal models are preferred. For example, zebrafish has less than 1% heterologous genes corresponded with early embryo development compared with that of human, which makes it an ideal model in AuNP cytotoxicity study.(78)

#### 2.3.2.5 Toxicity dependence

While strategies for cytotoxicity and cell uptake study of AuNPs are raised so differently between research labs, the dependence of toxicity is well agreed. Surface charge dependent toxicity is quite straightforward that positively charged AuNPs are more toxic due to the ease of disruption to the

negatively charged cell membrane.(79) Meanwhile several different mechanisms are postulated describing the size dependent cytotoxicity caused by AuNPs based on various experiment models and designs both *in vitro* and *in vivo*. (80-83)

First and one of the most common mechanism is intracellular reactive oxidative species (ROS) induced by nanoparticles. Pan, et al. (81) showed that triphenylphosphine monosulfonate (TPPMS)-capped AuNPs with a gold core of diameter 1.4nm is superb toxic result in necrosis caused by oxidative stress while 15nm-AuNPs of similar chemical composition are nontoxic. Furthermore, reduced toxicity after pretreating cells with anti-oxidants (e.g. glutathione) supported the ROS theory. Note that in the same study important role of capping ligands has been high-lightened that glutathione capped AuNPs with similar diameter (1.1nm) do not induce cell death. However, a newly reported thiolate-coated gold nanocluster Au<sub>55</sub> is highly toxic when treating human embryonic stem cells (hESCs).(36) Second mechanism states that cytotoxicity is due to the ultra-small size of Au<sub>55</sub> clusters enables irreversible coordination between the clusters and the major grooves of DNA molecule.(80) Among various cellular molecules, Au<sub>55</sub>

clusters surprisingly bind to DNA molecules in a large fraction, which is believed to affect transcription and/or duplication in the cell. This is due to a) the dimensional fitting between gold clusters of  $\sim 1.4\text{nm}$  and major grooves of DNA; b) the polydentate ligand system of nucleus provides higher stability compared to the monodentate capping ligands.(80) Third mechanism involves cell membrane interference. One study shows that  $\text{Au}_{55}$  clusters are extremely toxic to hESCs even after pretreatment with thiolate capping ligands, and without evidence of entering the cells they concluded that some disruptions towards cell membrane occurred.(36) Rotello group believes that the toxicity is related with the strong electrostatic interaction between the negatively charged bilayer with cationic ligand coated AuNPs, which can be addressed by anionic capping.(79) Another group is attributing the interference to blockage of membrane ion channels(84), note that in this case after thiol-stabilization the toxicity is reduced.

AuNP cytotoxicity, especially caused by  $\text{Au}_{55}$  clusters, appears to be capable of being reduced by modifying the AuNPs with proper capping ligands such as thiolates.(81, 82) While the toxicity study is mainly conducted in cell based experiments, in order to make the connection between in vitro

models and vertebrate animal models, the extended fish embryo test (FET) using zebrafish is applied.(83) In this study, toxicity of lethal triphenylphosphine monosulfonate (TPPMS) capped 1.4 nm AuNPs was reduced largely after addition of glutathione, which is due to replacement of capping ligand on the AuNP surface. Note that in the same study it also shows different toxicity compared with HeLa cells study conducted by the same group.(83)

However, there are some exceptions which are of great interest. As described above, a large number of toxicological studies are *in vitro* methods using immortalized cell lines, which may not provide information concerning biological barrier penetration, organ and/or cell specificity, embryonic development and subsequent differentiation. Another issue is that animal studies conducted using either zebrafish model or small rodent model make it hard to compare with human body. Instead of using cancerous cell lines, mouse embryonic stem cells are used to assess embryotoxicity in several experiments (85, 86), even more, a research of first use of human embryonic stem cells (hESCs) for embryotoxicity and neurotoxicity test has been reported.(36) hESCs is very suitable for cytotoxicity not only because it is a

normal cell lines, but also because of its pluripotency makes it extremely important to help determine the effects of AuNPs on differentiation process as well as on the differentiated neural progenitor cells (NPCs). Size-dependent cytotoxicity was observed when inducing AuNPs in 1.5nm, 4nm, and 14nm with coating of thiolate capping ligands, 1.5nm AuNPs is extremely toxic and killed most of the hESCs while 4nm- and 14nm-AuNPs showed nontoxic.(36) In the same study it also shows that when exposed to all three sizes of AuNPs under nontoxic dosage the in vitro differentiation potential would not be affected, however, during neural differentiation, 1.5nmAuNPs-treated group showed smaller embryo bodies which suggested that AuNPs in this size may cause negative influence even at sublethal concentration. After inducing 1.5nm AuNPs, NPCs were almost dead after 3 days referring to further toxicity of small size AuNPs. Note that cell uptake analysis shows that AuNPs in 1.5nm cannot enter hESCs in a noticeable amount instead a large amount of accumulation in the feeder layer cells was found.(36) This indicates that uptake of AuNPs varies among different cell lines, and this difference may lead to different toxicity mechanisms.



## **CHAPTER 3 ENGINEERING OF GOLD NANOPARTICLES CAPABLE OF BYPASSING BLOOD-BRAIN BARRIER**

**This chapter is reproduced with permission from the *Scientific reports* 6 (2016): 25794. Yanhua Zhang, Janelle Buttry Walker, Zeljka Minic, Fangchao Liu, Harry Goshgarian, and Guangzhao Mao. "Transporter protein and drug-conjugated gold nanoparticles capable of bypassing the blood-brain barrier." And the *Journal of Spinal Cord Medicine*, accepted on 3th January 2019. Fangchao Liu, Yanhua Zhang, Janelle L. Buttry Walker, Guangzhao Mao, and Harry G. Goshgarian. " Diaphragmatic Recovery in Rats with Cervical Spinal Cord Injury Induced by a Theophylline Nanoconjugate: Challenges for Clinical Use".**

### **3.1 Introduction**

The leading causes of death among persons with spinal cord injury (SCI) since 1973, according to the National SCI Database, are from pneumonia and septicemia due to damage to respiratory muscle function caused by SCI(87). The major therapeutic challenge in the treatment of respiratory dysfunction caused by SCI, similar to other neurological diseases, is the inability of many drugs to go across the blood-brain barrier (BBB). The BBB is a natural defense

system for the brain and generally only permits diffusion of neutral, lipophilic, and low molecular weight (smaller than 400-600 Da) molecules into the central neuron system (CNS) from blood(88, 89). Wheat germ agglutinin (WGA) is a lectin recognized by *N*-acetylglucosamine and sialic acid located on most neuronal cell membranes(90, 91). WGA, in a few studies, has been used to enhance intranasal delivery of peptides to the brain through the olfactory route due to its affinity to the olfactory mucosa(92, 93). However, to our knowledge, this is the first study to use wheat germ agglutinin-horseradish peroxidase (WGA-HRP) as a targeting moiety to transport drug-bound nanoconjugates of tens of nanometers in size exclusively to the phrenic motoneurons that control respiratory function, effectively bypassing the BBB. When injected into muscle, WGA bound conjugates undergo retrograde transport to the motoneuron cell bodies and is then transsynaptically transported to the pre-motor neurons(94, 95). We synthesized a three-part nanoconjugate consisting of WGA-HRP chemically bound to AuNPs, which were also chemically bound to drugs previously shown to induce recovery of the diaphragm paralyzed by SCI. Following intramuscular injection into the diaphragm, the WGA-HRP component of the

nanoconjugate engages in receptor-mediated endocytosis resulting in retrograde transport of the nanoconjugate within motoneurons to the phrenic nuclei in the cervical spinal cord and transsynaptically to the rostral ventral respiratory groups (rVRGs) in the medulla. The drug, 1,3-dimethylxanthine (theophylline or THP), is an adenosine receptor antagonist clinically used for the treatment of respiratory dysfunctions such as asthma, bronchitis, and respiratory muscle paralysis resulted from SCI(96-98). In rats with a spinal cord hemisection at the second cervical spinal segment (C2Hx), systemic (oral or intravenous) administration of THP or another adenosine receptor antagonist, 1,3-dipropyl-8-cyclopentylxanthine (DPCPX), resulted in an increase in respiratory output and recovery of the respiratory related activity by stimulating the crossed phrenic pathway (CPP)(97, 98). The CPP is a latent pathway, which crosses the midline below the level of SCI injury to synapse on the ipsilateral phrenic nuclei (PN) in the 3<sup>rd</sup> through 6<sup>th</sup> segments of the cervical spinal cord while the primary descending pathway, between the neuronal connection from the rVRG in the medulla to the ipsilateral phrenic nucleus, has been severed by a high cervical SCI(94). However, in humans the therapeutic dose of methylxanthines causes intolerable side

effects including nausea and seizures(99, 100). These side effects are associated with nonspecific biodistribution and neuronal hyperactivity induced by the drug. Therefore, we designed a nanoconjugate in which the drug and the transporter protein are chemically linked through a nanoparticle carrier, the AuNPs, in order to reduce side effects of the drug by delivering it selectively to the respiratory neurons in the cervical spinal cord and medulla. A biodegradable bond between the drug and the nanoparticle carrier enables drug release at the targeted sites. The effectiveness of the nanoconjugate drug delivery was verified by the return of diaphragm muscle function previously paralyzed due to SCI. AuNPs were selected as the drug carrier due to their biocompatibility, tunable colloidal chemistry, and quality control through a wide range of analytical methods(101, 102).

## 3.2 Experimental methods

### 3.2.1 Materials

Chemicals used in the following experiments: gold(III) chloride trihydrate ( $\text{HAuCl}_4 \cdot 3\text{H}_2\text{O}$ , 99% metal trace); sodium citrate tribasic dehydrate (98%); mercaptosuccinic acid (MSA, 97%); sodium borohydride ( $\text{NaBH}_4$ , 98%);

4-dimethylaminopyridine (DMAP, 99%); dimethyl sulfoxide (DMSO, 99.8%); 37% formaldehyde solution; tetrahydrofuran (THF, 99%); N-hydroxysuccinimide (NHS, 98%); dipropylcyclopentylxanthine (DPCPX, 97%); theophylline (THP, 97%) triethylamine (Et<sub>3</sub>N, 99%); lectin from triticum vulgaris (WGA-HRP) (Sigma-Aldrich, St. Louis, MO); 1-Ethyl-3-(3-dimethylaminopropyl) carbodiimide (EDC, 98%) (Sigma-Aldrich, St. Louis, MO).

### 3.2.2 Nanoconjugate Synthesis and characterization

The detailed synthesis of the nanoconjugate (WGA-HRP-AuNP-proTHP) has been published elsewhere (103). Briefly, to link theophylline to the AuNP via an ester bond, a hydroxymethyl group was added to theophylline creating 7-(hydroxymethyl) theophylline or “proTHP”, using the Mannich reaction (103, 104). The reaction product was analyzed by proton nuclear magnetic resonance (<sup>1</sup>H NMR) to verify the formation of proTHP. Gold chloride (HAuCl<sub>4</sub>) was reacted with tri-sodium citrate to synthesize AuNPs. Mercaptosuccinic acid (MSA) was added as the capping ligand for the AuNPs. Then proTHP was attached to the MSA-capped AuNPs via a biodegradable ester bond to enable *in vivo* drug release (105). WGA-HRP was coupled to the MSA-capped AuNPs

via an amide bond (106). Each step of the synthesis was verified by UV-*vis* spectroscopy, transmission electron microscopy, dynamic light scattering, and thermogravimetric analysis (TGA). Due to the instability of the synthesized proTHP, proTHP was stored in argon to prevent hydrolysis of the hydroxymethyl group by moisture in room air. In addition, to limit variation due to the biodegradable nature of the ester bond linking the AuNP to 7-(hydroxymethyl) theophylline, the final solutions were only used up to 30 days after synthesis.

A variation of the nanoconjugate synthesized with hydroxyethyl theophylline (Sigma-Aldrich) in place of the 7-(hydroxymethyl) theophylline was also produced. The hydroxyethyl theophylline variation was tested to determine if the ester bond between theophylline and AuNPs could be further stabilized.

UV-*vis* absorption spectroscopy (Varian Cary 50) was used to determine the AuNP size based on the Beer-Lambert law. The scan range was 200–800 nm.

The transmission electron microscope (TEM) images were taken on a JEOL JEM-2010 electron microscope. Samples were prepared by placing a

droplet of the nanoconjugate solution on a Formvar-coated copper TEM grid. Excess liquid was removed by filter paper under the grid and the sample was air-dried. The working voltage was 200 keV and the current was 109 mA. For each image, 30 particles were randomly selected and measured to give the nanoparticle size distributions.

The nanoparticle size was determined by dynamic light scattering (DLS) (Zetasizer Nano ZS, Malvern). A one ml solution of nanoparticle in PBS buffer was placed in a 2.0 ml polystyrene cuvette. The backscattering angle  $\Theta$  was fixed at  $180^\circ$  with a laser wavelength  $\lambda = 633$  nm. The size measurement range was set between 1 nm and 6  $\mu\text{m}$ . The electrophoretic mobility of the nanoparticles was measured using the laser Doppler velocimetry and phase analysis light scattering technique of the Malvern Zetasizer. The electrophoretic mobility was converted into a zeta potential using the Smoluchowski equation using the Malvern software.

TGA analysis was used to quantify the chemical composition of the nanoconjugate. TGA was performed on the SDT-Q-600 instrument using air as the working gas. The temperature range was 100–800  $^\circ\text{C}$  with a heating rate of 10  $^\circ\text{C}/\text{min}$ .

The LDI-MS measurements were carried out on a Bruker UltrafleXtreme MALDI-TOF/TOF Mass Spectrometer (Lumigen Instrument Center, Detroit). The samples were analyzed by LDI-MS after being transferred onto a MALDI target for LDI-MS analysis without adding any organic matrix. All mass spectra were acquired in the reflection mode and represent an average of 500 laser shots at a repetition frequency at 500 Hz. The accelerating voltage was set to 20 kV. The laser power was optimized in the range of 70–90% for each sample. The Bruker software flexAnalysis (version 3.4) was used for data analysis. Each sample was measured 10 times by LDI-MS.



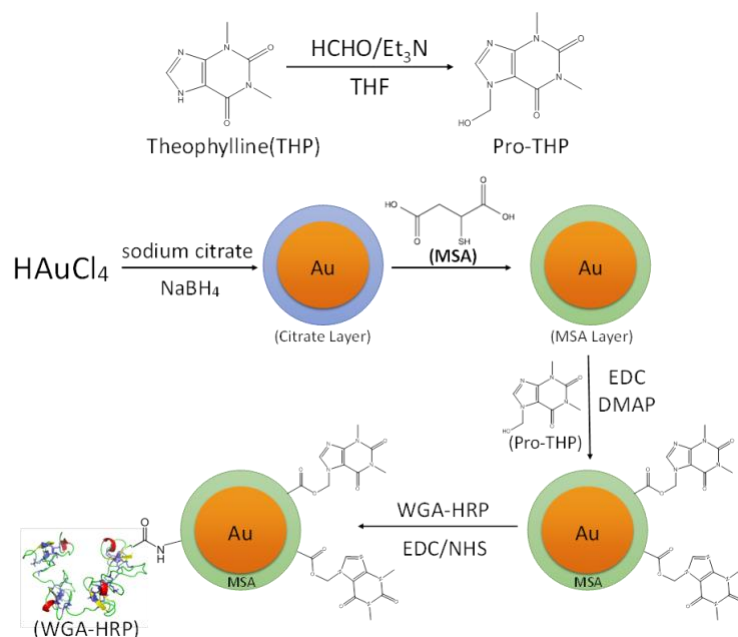


Figure 3-1 Synthesis schematic of transporter protein WGA-HRP and drug THP conjugated to the AuNPs.

### 3.2.3 C2 Hemisection Surgery

All animal studies were approved by the Wayne State University School of Medicine Institutional Animal Care and Use Committee. In addition, all experiments were carried out in accordance with the Code of Ethics of the World Medical Association for experiments involving animals. Adult male Sprague Dawley rats were used in these studies (N=123). The rats were injected with atropine sulfate (0.04 mg/kg, im) 10 min prior to anesthesia induction to reduce mucus secretions during the subsequent aseptic survival surgery. The initial dose of anesthesia was a mixture of ketamine (70 mg/kg,

ip) and xylazine (7 mg/kg, ip). After anesthesia induction, bupivacaine (2 mg/kg, sc), a local anesthetic, was injected into the dorsal neck. The neck was then shaved and prepared for aseptic surgery. A left C2Hx surgical procedure was carried out as previously described (94). The dorsal neck muscles were closed using 4–0 absorbable sutures (Vicryl) followed by wound clips (Reflex® 9 mm) for the skin.

#### 3.2.4 Electromyography (EMG) Analysis

In all rats, immediately after C2Hx, paralysis of the ipsilateral hemidiaphragm was confirmed by EMG analysis. The previous study by Moreno and colleagues (94) correlated the loss of EMG activity in the ipsilateral hemidiaphragm to the lesion extent damaging the ipsilateral lateral and ventral funiculi of the cervical spinal cord where the descending respiratory drive is located, which was used here to ensure a complete hemisection (94). The abdominal surface of the diaphragm was exposed by a 6–8 cm horizontal incision made approximately 0.5 cm caudal and parallel to the costal margin. Bipolar platinum wire electrodes (Grass F-E2) were placed in each side of the diaphragm. Signals were amplified (20,000×) and band pass-filtered (30 Hz–3 kHz) by Grass amplifiers (model P511 AC, Astro-

Med, Inc., West Warwick, RI) and raw EMG signals were recorded by a Cambridge Electronic Design (CED, Cambridge, England) data acquisition system integrated with CED Spike 2<sup>®</sup> software. Recordings were taken from three areas of the left hemidiaphragm: anterior (sternal), lateral (costal) and posterior (crural). C2Hx rats that showed a complete absence of activity in all three areas and could produce an augmented breath were included in the study. An augmented breath is a confirmation that the CPP is intact and functional (94, 107).

To observe the course of effect of theophylline following nanoconjugate injection subsequent EMGs were sampled from day 2 post injection up to and including day 14. Each rat underwent at minimum 1 EMG and no more than 3 separate EMGs with a minimum of 1 day between surgeries. The days selected for EMG were determined based on the time course for each rat and how many surgeries had already occurred; days 2 through 7 each had a minimum of 7 rats used for data on each day. Subsequent EMG recordings were performed under ketamine/xylazine anesthesia while spontaneously breathing.

### 3.2.5 Nanoconjugate Administration

Following EMG confirmation of hemidiaphragm paralysis immediately after the C2Hx, intradiaphragmatic injections were administered. Groups received injections based on their weight of one of the following solutions; i) nanoconjugate (WGA-HRP-AuNP-proTHP) 0.0005 mg/kg N=3, ii) nanoconjugate 0.0008 mg/kg N=4, iii) nanoconjugate 0.0025 mg/kg N=4, iv) nanoconjugate 0.005 mg/kg N=7, v) nanoconjugate 0.0075 mg/kg N=7, vi) nanoconjugate 0.01 mg/kg N=6, vii) nanoconjugate 0.03 mg/kg N=19, viii) nanoconjugate 0.07 mg/kg N=25, ix) nanoconjugate 0.12 mg/kg N=23, x) WGA-HRP-AuNP N=6, xi) AuNP-proTHP 0.07 mg/kg N=8. Investigation of the hydroxyethyl theophylline nanoconjugate consisted of 2 groups; 0.002 mg/kg N=5, and 0.3 mg/kg N=6. Injections (10 $\mu$ l maximum volume per injection site) were spread equally from the posterior to anterior areas of the diaphragm using a Hamilton syringe. The needle was inserted parallel to the muscle fibers such that the tip of the needle was visualized by eye before administration of the injections, the needle was held in place for 5–10 seconds before it was slowly withdrawn from the muscle to prevent leakage(108).

### 3.2.6 Post Procedure Care

Incisions were cleaned and the rats were given yohimbine (2mg/kg, ip) to reverse the xylazine, and buprenorphine (0.01mg/kg, sc) in 10mL saline for pain management. The rats were recovered on a heating blanket in a supine position to limit pressure on the diaphragm. Once rats could ambulate, they were returned to clean soft litter-lined cages with food and water provided ad libitum on the floor of the cage. The rats were also given cereal (Fruit-Loops®) as an enticement to eat. For the following 48-hours post-operative period, injections of buprenorphine (0.01mg/kg, sc) were given every 8-12 hours for pain management. Rats survived for 3, 7, or 14 days' post injection depending on the timeline for each experimental group.

### 3.2.7 Immunohistochemical Visualization of Nanoconjugate

72 hours after intradiaphragmatic injection of the nanoconjugate 0.12mg/kg (N=3) into the left hemidiaphragm, rats were euthanized and underwent transcranial perfusion using heparinized saline followed by 4% formaldehyde (Fisher, F-79) (108). The cervical spinal cord (C3-C6) and medulla were removed and post fixed in 4% formaldehyde for 24 hours followed by 72 hours in 30% sucrose for cryoprotection. Tissues sections 50 microns thick were cut transversely on the cryostat and collected in PBS.

Tissue sections containing the phrenic nuclei and rVRGs underwent the immunohistochemistry protocol as described by Minic *et al.* (108); sections were washed three times in the immuno-buffer (PBS with 0.3% Triton) and then blocked using 10% normal horse serum (Invitrogen) in the immuno-buffer. Sections were incubated in primary antibody goat anti-WGA (1:200, AS-2024, Vector Laboratories), diluted in 10% normal horse serum immuno-buffer solution for 72 h, and then washed in PBS. Sections were then incubated in the biotinylated secondary antibody, donkey anti-goat overnight (1:400, Jackson Immuno Research Laboratories). Sections were then incubated in streptavidin-tagged-Cy3 for 4 h and then mounted wet on the slides and coverslip. Tissue sections were examined on a Zeiss Axioimager.M2 fluorescent microscope. Images were captured using the Zen 2 pro Blue edition program. Off-line processing was used to acquire high-power views of the phrenic nuclei and the rVRGs.

### 3.2.8 Phrenic Nerve Recordings

Bilateral phrenic nerve recordings were sampled at day 3, 7, and 14 under standardized conditions. The rats were injected with atropine sulfate (0.06mg/kg, im) 10 minutes prior to anesthesia induction to reduce mucus

secretions during the procedure. The anesthesia was a mixture of ketamine (70mg/kg, ip) and xylazine (7mg/kg, ip), a supplement was provided as needed. Phrenic nerves were accessed from the ventral surface of the neck and cut distally to eliminate afferent activity. Each nerve was positioned on platinum bipolar electrodes and coated with mineral oil to prevent fluid interference with the signal and to reduce electrical noise. Before acquiring nerve activity data, the following standardizing conditions were performed: (1) animals were bilaterally vagotomized; (2) animals were paralyzed using pancuronium bromide (0.5 mg/kg, iv); and (3) animals were placed on a ventilator set at 3–5mmHg above the apnea threshold (108). The procedure for determining the apnea threshold has been described previously (109). The unprocessed recording was amplified 5000 times using Grass P511 amplifiers (Grass Technologies), filtered at 0.3–1 kHz. The recordings were digitized, rectified, and integrated in 0.1 s intervals using the Cambridge Electronic Design data acquisition system and the Spike 2 software.

### 3.2.9 Statistical Analysis

As described by Minic *et al.* (108), EMG analysis was intended to only analyze the *incidence* of recovery not to determine the *amount* of recovery.

Treatment groups were divided into a “Yes” or “No” category based on the following criteria described by Minic *et al.* (108); Recovery of the left hemidiaphragm was considered positive/Yes in each rat only if the following conditions were met: (1) the EMG activity was detected in at least two of the three diaphragm areas (posterior, lateral, or anterior); and (2) if the activity persisted for the duration of the study. In each treatment group, rats were then divided into those having recovery or not, and the Fisher exact test was performed to determine whether the proportion of rats with an incidence of recovery in the treated groups was statistically different from the ratio of control animals with an incidence of recovery. The Fisher’s exact test was followed by the Bonferonni adjustment to correct for the number of comparisons tested. A  $\alpha$  level of 0.016 was considered statistically significant (SigmaPlot 13.0). Groups that demonstrated a significantly higher incidence of recovery during the initial screening process, to determine optimal drug dose, were further investigated using phrenic nerve recordings to quantify recovery observed.

Terminal bilateral phrenic nerve recordings were used to estimate the increase in phrenic nerve output after nanoconjugate injections as described



by Minic *et al.* (108). The areas under 10 consecutive integrated waveforms (INT) in the right phrenic nerve (RPN) and left phrenic nerve (LPN) activity were averaged and expressed as mean  $\pm$ SE. Activity of the LPN was used as an index of the recovered respiratory activity in the THP nanoconjugate-treated rats. Both maximum (MAX) LPN amplitude activities as well as the areas under the curves (AUC) were expressed as the percentage of the RPN whose signal was set to be 100%. Then the average % INT and the average % MAX for each group was averaged and subjected to statistical examination using SigmaPlot 13.0. All groups underwent One-way ANOVA followed by Holm-Sidak pairwise comparison to determine the effect of the injected solution. A  $\alpha$  level of 0.05 was considered statistically significant.

### 3.3 Results

#### 3.3.1 Characterizations of AuNP conjugates

The nanoconjugates from each stage of synthesis were characterized by UV-*vis* spectroscopy, transmission electron microscopy (TEM), dynamic light scattering (DLS), and thermogravimetric analysis (TGA). **Figure 3.2A** shows the UV-*vis* spectra of MSA-capped AuNP, AuNP-pro-THP, and WGA-HRP-AuNP-pro-THP obtained in deionized water (pH = 5.8) at room

temperature. The UV-*vis* spectra of a constant absorption peak at 508-510 nm are in the expected range for AuNPs with 4 nm core diameter and they also indicate a high degree of colloidal dispersion stability at all stages of the synthesis. **Figure 3.2B-D** show TEM images of MSA-capped AuNPs, AuNP-pro-THP, and WGA-HRP-AuNP-pro-THP. The particle size histograms of which are shown in **Figure 3.2E-G**, respectively. The AuNPs were well dispersed and the diameter of the AuNPs remained unchanged at  $4.1 \pm 0.3$  nm before and after conjugation with pro-THP according to TEM. The AuNPs size increased slightly to  $5.2 \pm 1.3$  nm. Here, there is uncertainty in particle core size determination due to the conjugated WGA-HRP and overlapping particles. Particle agglomeration, observed in WGA-HRP-AuNP-pro-THP samples, is likely caused by the TEM sample preparation step (**Figure 3.2C**).

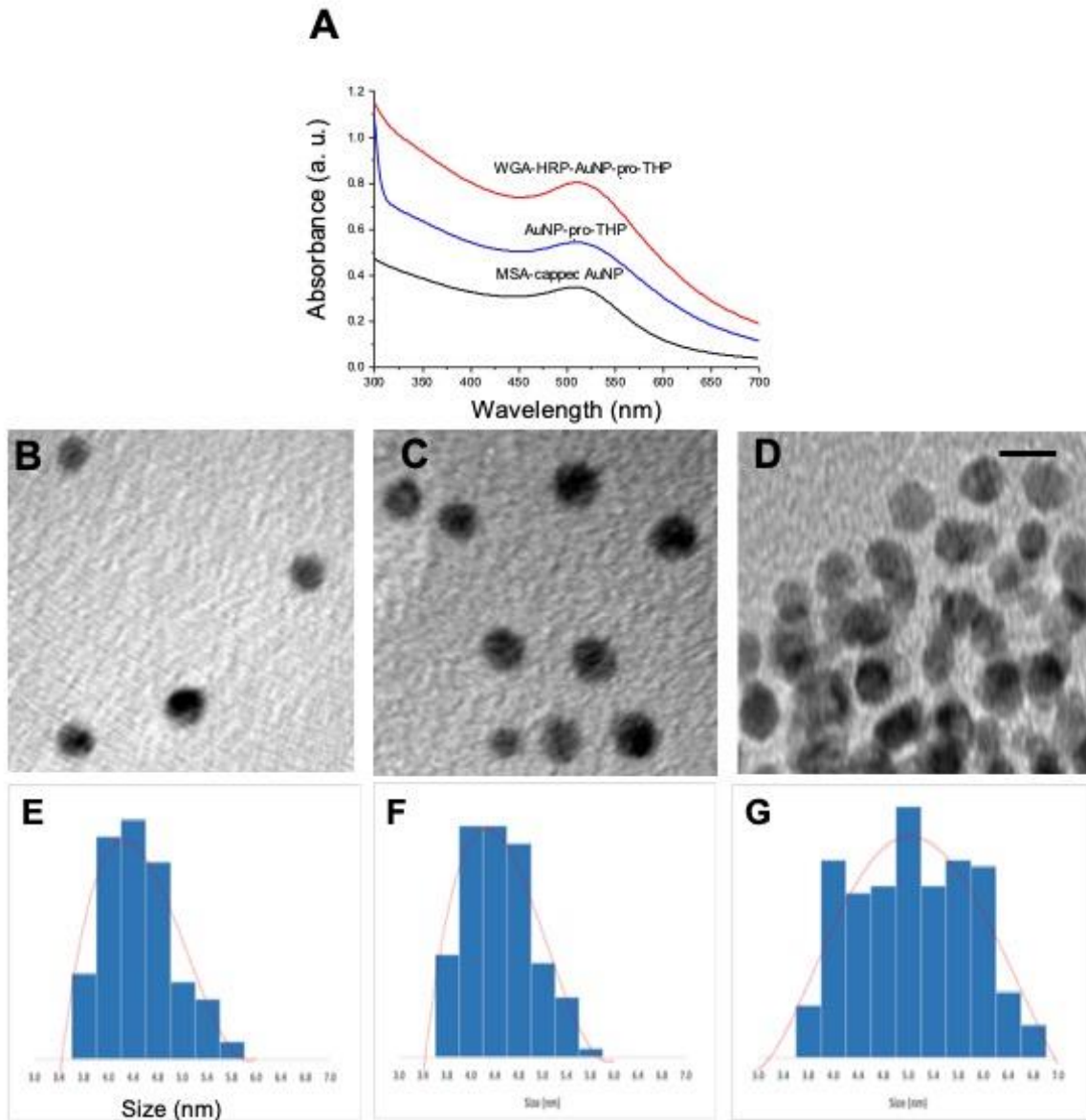


Figure 3-2 Characterization of transporter protein and drug-conjugated AuNPs. A) UV-vis spectra measured at room temperature. B-D) TEM images of AuNP conjugates. E-G) Sized distributions of AuNP conjugates

The zetasizer provided measurements of the particle hydrodynamic size by DLS and the zeta potential by electrophoresis. The hydrodynamic

diameters are 4.8 nm (zeta potential = -28.5 mV) for MSA-capped AuNP, 11.7 nm (zeta potential = -36.6 mV) for AuNP-pro-THP, and 37.8 nm (zeta potential = -35.6 mV) for WGA-HRP-AuNP-pro-THP. The zeta potential measurements were conducted in PBS buffer (pH = 7.4) at 37°C. The hydrodynamic size of different nanoconjugates are shown in **Figure 3.3**. The size increase after each conjugation reaction is consistent of successful coupling of the drug or protein to the AuNP. The negative surface charge characteristic of all the nanoparticles provides the necessary electrostatic repulsion to ensure aqueous dispersion stability of the nanoparticles.

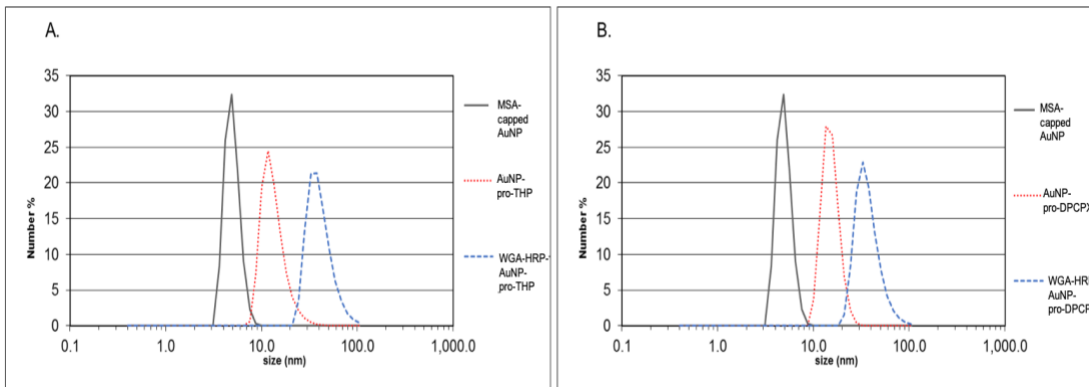


Figure 3-3 Zetasizer measurements of A) pro-THP nanoconjugates and B) pro-DPCPX nanoconjugates. All samples were measured in PBS buffer (pH=7.4) at 37°C.

The chemical compositions of the intermediate and final nanoconjugates were analyzed by TGA (**Figure 3.4A**). Based on the

percentages of weight losses at different stages of synthesis, we were able to estimate that in the final nanoconjugate, there are 204 pro-THP molecules conjugated to one 4 nm MSA-capped AuNP and 2 MSA-capped AuNPs conjugated to one WGA-HRP. The numbers of drug molecules conjugated correspond to 60% occupation for pro-THP of all available carboxyl provided by MSA. The detailed calculations can be found in the SI 1.3. We observed that the number of conjugated drug molecules remained unchanged with increasing drug to Au molar feed ratio in the reaction indicating that a surface saturation was reached possibly due to a steric effect. It is interesting to note that in both THP (**Figure 3.4A**) and DPCPX (**Figure 3.4B**) cases we obtained similar protein to AuNP molar ratio of 1 to 2. This nanostructure configuration is consistent with the TEM and DLS results.

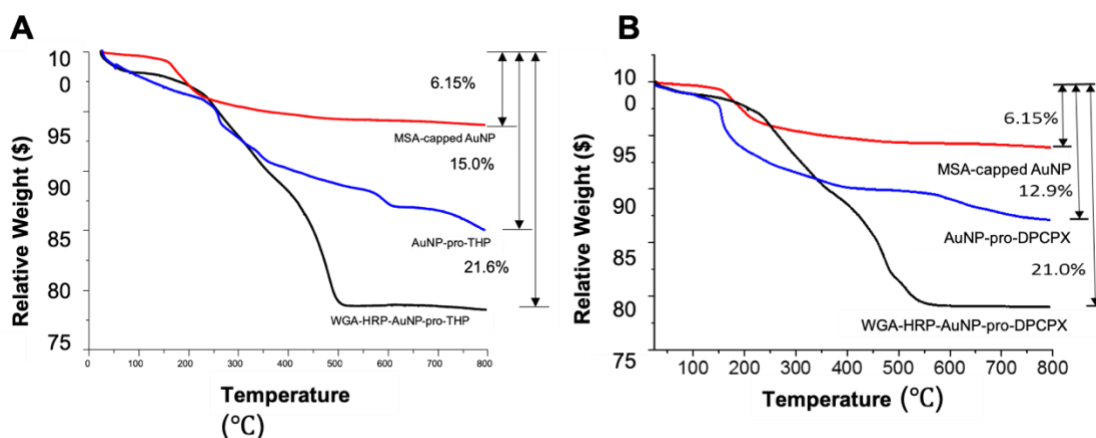


Figure 3-4 TGA data of weight loss for A) MSA-AuNPs, AuNP-pro-THP, and WGA-HRP-AuNP-pro-THP; B) MSA-AuNPs, AuNP-proDPCPX, and WGA-HRP-AuNP-pro-DPCPX.

Calculations of nanoconjugate drug and protein loading amounts based on TGA and TEM results are shown below.

The weight of one molar AuNP ( $W$ ) with a diameter ( $D = 4$  nm based on the TEM measurements) was estimated using the following formula using the bulk density of gold ( $\rho = 19.3$  g/cm<sup>3</sup>):

$$W = \rho \times \frac{1}{6} \pi D^3 \times 6.022 \times 10^{23} = 19.3 \frac{\text{g}}{\text{cm}^3} \times \frac{1}{6} \pi (4 \times 10^{-7} \text{ cm})^3 \times 6.022 \times 10^{23} = 3.89 \times 10^5 \text{ g/mol}$$

The molecular weight of MSA (C<sub>4</sub>H<sub>6</sub>O<sub>4</sub>S) and pro-THP are 150 g/mol and 210 g/mol, respectively. The weight loss, 100:6.6 = AuNP:MSA,

corresponds to 171 MSA molecules per AuNP as calculated below. As a result, each MSA-AuNP has 342 maximum reactive sites.

$$\text{No. of MSA molecules} = \frac{6.6}{150} \times \frac{3.89 \times 10^5}{100} = 171.16$$

The area of MSA coverage on AuNP ( $A$ ) is calculated below:

$$A = \frac{\pi D^2}{\text{No. of MSA molecules}} = \frac{\pi (4\text{nm})^2}{171.16} = 0.294\text{nm}^2 = 29.4\text{\AA}^2$$

The weight loss of 15.0% (AuNP: MSA: pro-THP = 100: 6.6: 11.1) shows that 205.6 pro-THP molecules are conjugated to one AuNP as calculated below:

$$\text{No. of pro-THP molecules} = \frac{11.1}{210} \times \frac{3.89 \times 10^5}{100} = 205.6$$

This means that 60% of all possible reactive sites provided by MSA are occupied by pro-THP.

The total weight loss for the three-part nanoconjugate is 21.6% (AuNP: MSA: pro-THP: WGA-HRP = 100: 6.6: 11.1: 11.5) indicates that each WGA-HRP is conjugated to 2 AuNPs as calculated below:

$$\text{No. of WGA-HRP molecules} = \frac{11.5}{22367} \times \frac{3.89 \times 10^5}{100} \approx 2$$

For pro-DPCPX drug (TGA spectra shown in Supplementary Fig. 3), the weight loss of 12.9% (AuNP: MSA: pro-DPCPX = 100: 6.6: 8.2) corresponds to 96 pro-DPCPX molecules conjugated to one MSA-capped AuNP. This means that 28% of MSA reactive sites are occupied by pro-DPCPX as calculated below:

$$\text{No. of pro-DPCPX molecules} = \frac{8.2}{332} \times \frac{3.89 \times 10^5}{100} = 96$$

The total weight loss for the three-part nanoconjugate is 21.0% (AuNP: MSA: pro-DPCPX: WGA-HRP = 100: 6.6: 8.2: 11.8) indicates that each WGA-HRP is conjugated to 2 AuNPs as calculated below:

$$\text{No. of WGA - HRP molecules} = \frac{11.8}{22367} \times \frac{3.89 \times 10^5}{100} \approx 2$$

### 3.3.2 Immunostaining

Three rats underwent intradiaphragmatic injections of the nanoconjugate following a C2Hx to visualize the locations of the nanoconjugate. An immunohistochemical technique was utilized to visualize the WGA component of the nanoconjugate. The WGA-HRP-AuNP bond is a relatively long-lasting amide bond whereas the AuNP-proTHP bond is a transient ester bond. Therefore, we can assume that the location of WGA



should also identify where the AuNPs are but not necessarily the proTHP. All 3 rats produced identical results verifying what was reported in (103). WGA positive label was identified in the ipsilateral PN in the cervical spinal cord and bilaterally in the rVRGs in the medulla (**Figure 3.5**). The bilateral rVRGs labeling was notably less intense compared to the label in the PN. These results suggest that at minimum, the WGA-HRP-AuNP portion of the nanoconjugate is capable of being transported to the PN and subsequently transsynaptically to the rVRG following intradiaphragmatic injection.

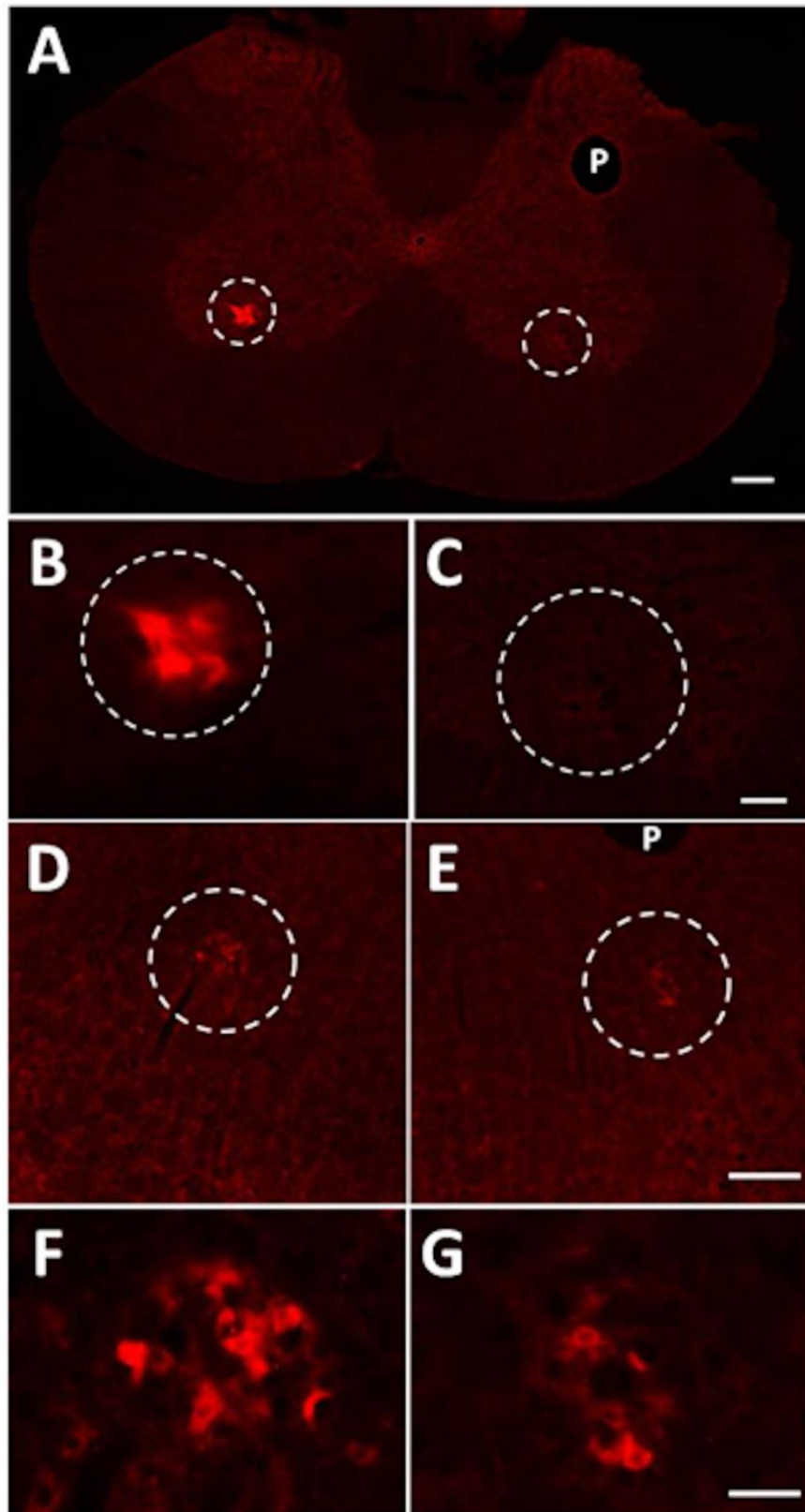


Figure 3-5 WGA identified in the phrenic nuclei in the cervical spinal cord and rostral ventral respiratory groups in the medulla 72 hours after intradiaphragmatic injection. Scale bar is 50  $\mu\text{m}$ . P (in A and E) notes pinhole to mark side contralateral to the injection.

### 3.3.3 Electromyography (EMG)

Based on the criteria described by Minic et al. (108), results from EMG analysis were used as a Yes/No screening tool to determine which doses should undergo further analysis using the phrenic nerve recording technique. Starting with the lowest tested dose, functional recovery of the diaphragm after a one-time injection of the nanoconjugate dose 0.0005mg/kg was detected in 66% of the rats (N=3). Diaphragm activity was detected as early as day 3 and persisted to day 14, the longest time point tested. However, the duration of the burst was less than the non-injured side. Therefore, in each subsequent group, the dose was incrementally increased to find an optimal therapeutic dose.

The doses 0.0008mg/kg and 0.0025mg/kg both resulted in a return of diaphragm activity that occurred in 50% of the rats (N=4 and N=4, respectively). Both doses resulted in diaphragm recovery lasting the full 14 days. The doses of 0.005mg/kg and 0.0075mg/kg resulted in the incidence of

recovery in only 0.14% of the rats (N=7 and N=7, respectively) and the dose 0.01mg/kg resulted in no observable recovery (N=6).

When the dose was increased to 0.03mg/kg recovery was observed in 63% of the rats (N=19). Similarly, the dose 0.07mg/kg, resulted in the incidence of recovery as early as day 2 post nanoconjugate injection and lasted up to day 14 in 56% of the rats (N=25) (**Figure 3.6**), and the 0.12mg/kg dose resulted in the incidence of recovery in 45% of the rats (N=20). Interestingly, in 3 rats from the 0.12mg/kg dose group the LHD burst frequency was minimal but sporadic and sometimes off rhythm compared to the right side, a possible effect of over stimulation (97). Thus, we did not go beyond the 0.12mg/kg dose in this study.

Injection of a control solution containing a conjugate of just AuNP-proTHP 0.07mg/kg (no WGA-HRP) (N=8), or WGA-HRP-AuNP (no proTHP) (N=6) never produced recovery of the LHD.

Investigation of the hydroxyethyl theophylline nanoconjugate consisted of 2 groups; 0.002 mg/kg N=5, and 0.3 mg/kg N=6. The group that received 0.002mg/kg never produced recovery of the LHD. The group that

received 0.3 mg/kg had a 33% occurrence of recovery, however the bursting patterns were sporadic in respect to the pattern produced by the RHD.

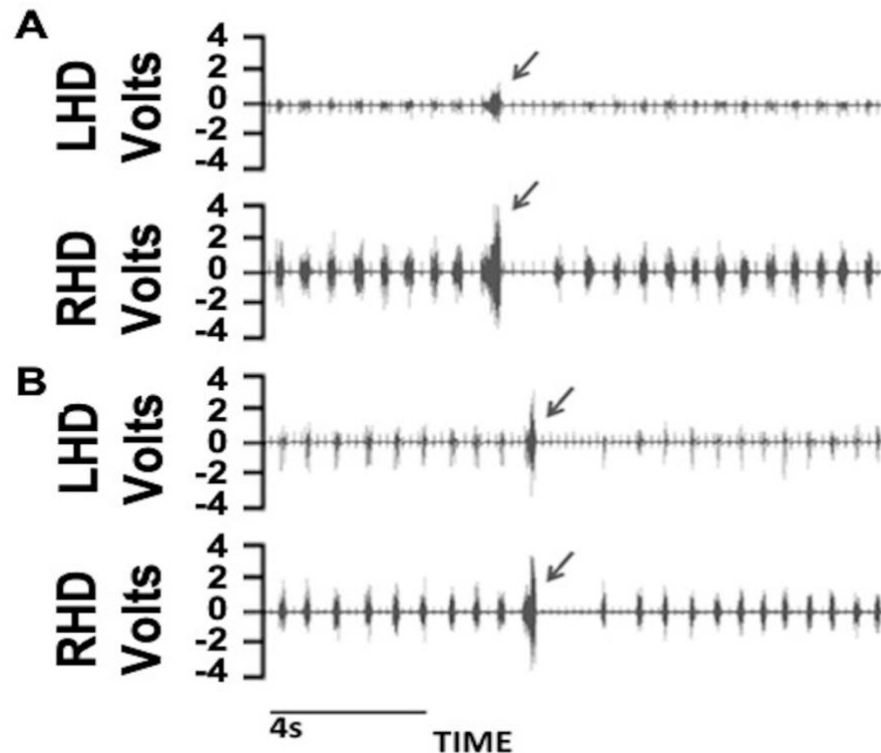


Figure 3-6 EMG traces 2 days and 14 days post injection 0.7 mg/kg nanoconjugate. Both recordings were obtained from the same rat. A) 2 days post injection of the dose 0.07mg/kg nanoconjugate there is a return of the bursting pattern in the left hemidiaphragm (top trace). The bursts in the left hemidiaphragm match those in the right hemidiaphragm (bottom trace). B) 14 days post injection; the activity has persisted in the left hemidiaphragm (top trace) and remains synchronous with the right hemidiaphragm (bottom trace). In both traces an augmented breath is demonstrated (arrows) followed by a short period of apnea. The augmented breath shows the crossed phrenic pathway is functional.

Statistical significance of the incidence of functional recovery detected with the EMG analysis was determined using the Chi Square-Fisher's exact test followed by the Bonferroni adjustment (**Figure 3.7**). Treatment with 0.03mg/kg, 0.07mg/kg, or 0.12mg/kg of the nanoconjugate via intradiaphragmatic injection resulted in a significantly greater proportion of rats achieving functional recovery when compared to the control 0.07mg/kg AuNP-proTHP;  $p=0.003$ ,  $p=0.010$ ,  $p=0.029$  respectively. Treatment with 0.03mg/kg or 0.07mg/kg of the nanoconjugate resulted in a significantly greater proportion of rats achieving functional recovery when compared to the dose 0.01mg/kg;  $p=0.015$ ,  $p=0.021$  respectively. In addition, treatment with 0.03mg/kg or 0.07mg/kg of the nanoconjugate resulted in a significantly greater proportion of rats achieving functional recovery when compared to the control WGA-HRP-AuNP;  $p=0.015$ ,  $p=0.021$  respectively. However, with lone EMG data it is unclear as to whether this is isolated muscle activity stimulated by the injection containing proTHP (110-115), or if it is a return of function mediated by the bulbospinal pathway via the phrenic nerve.

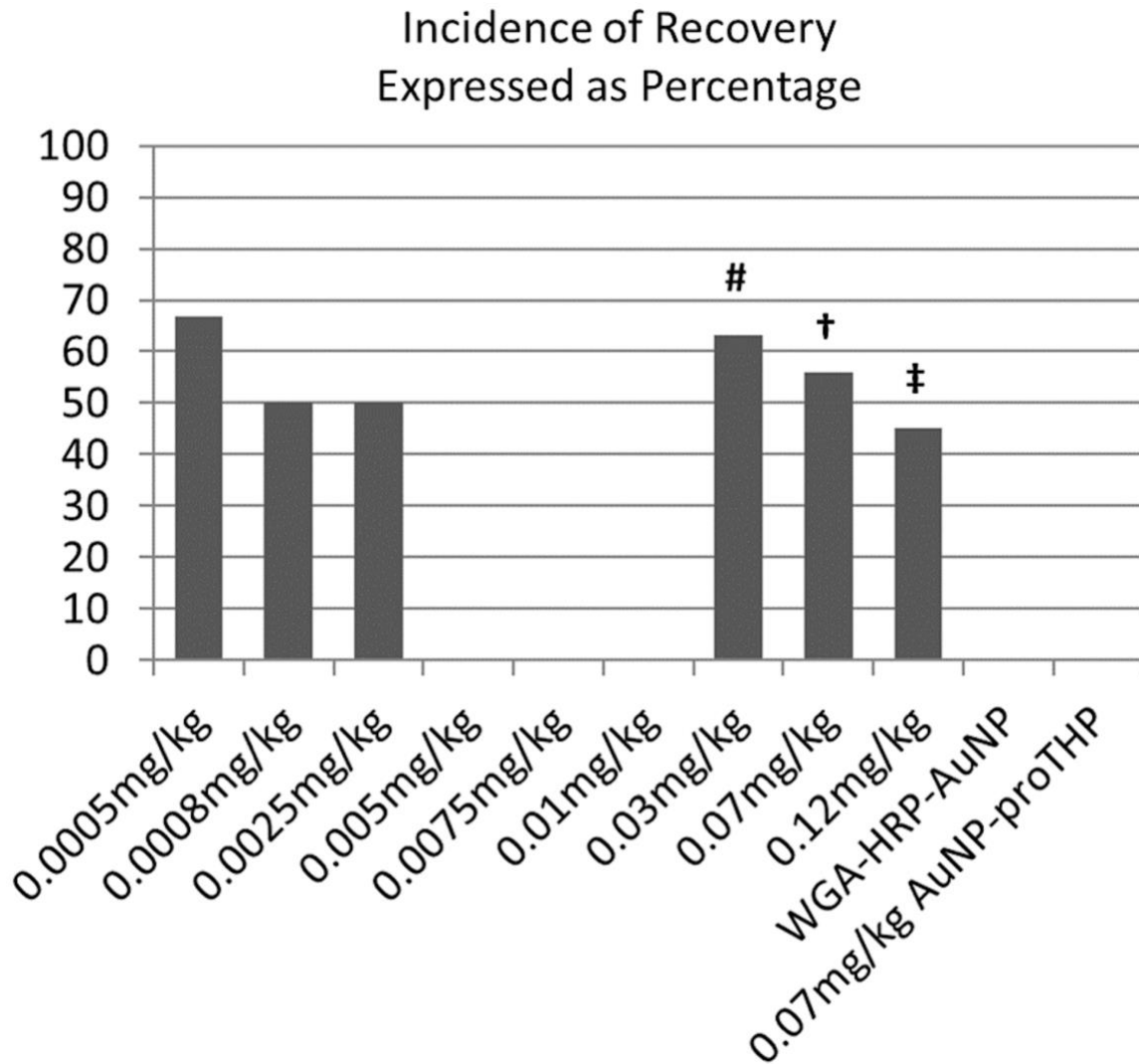


Figure 3-7 Percent of Rats with EMG Recovery of the Left Hemidiaphragm. The chart displays the percentage of rats in each group that had an incidence of recovery detected by EMG of the left hemidiaphragm. Statistical analysis consisted of data from 112 rats. A Chi-square test was performed, and significance was found between the proportions of observations (Yes/No) and the groups,  $\chi^2 (13, N = 112) = 27.075, p = 0.012$ . Treatment with the 0.03mg/kg nanoconjugate resulted in significantly greater (#) incidence of recovery compared to 0.01mg/kg ( $P = 0.015$ ); WGA-HRP-AuNP ( $P = 0.015$ ); and 0.07mg/kg AuNP-proTHP ( $P=0.003$ ). Treatment with the 0.07mg/kg nanoconjugate resulted in significantly greater (†) incidence of recovery

compared to 0.01mg/kg ( $P = 0.021$ ); WGA-HRP-AuNP ( $P = 0.021$ ); and 0.07mg/kg AuNP-proTHP ( $P = 0.010$ ). Treatment with the 0.12mg/kg nanoconjugate resulted in significantly greater ( $\ddagger$ ) incidence of recovery compared to 0.07mg/kg AuNP-proTHP ( $P = 0.029$ ).

#### 3.3.4 Phrenic nerve recordings

Based on the screening data obtained from the EMG analysis the doses 0.03, .0.7, and 0.12mg/kg were selected to analyze the amount of recovery based on the output of the phrenic nerves at days 3, 7, and 14. A representative recording from each day. The nanoconjugate induced recovery was quantified by analyzing 10 consecutive breaths from bilateral phrenic nerve recordings sampled at days 3, 7, and 14. Controls solutions were sampled on day 7. The area under the curve (AUC) from the right and left integrated (INT) waveforms were calculated and the percent recovery of the left compared to the right was calculated for both the INT and maximal amplitude (MAX). The data used in the following statistical analysis was obtained once physiologically standardized conditions were established (108, 109, 116-119). One-way ANOVA with Holm-Sidak pairwise comparison was performed to determine the effect of the nanoconjugate or control solution on the amount of left phrenic nerve (LPN) recovery.



One-way ANOVA showed a significant drug effect on day 3 between the 0.12mg/kg dose and the remaining two groups, 0.03mg/kg dose and 0.07mg/kg dose for the AUC ( $p < 0.001$ ) but not the MAX (**Figure 3.8**).

One-way ANOVA showed a significant drug effect on day 7 for the AUC between the 0.07mg/kg dose and the following; 0.03mg/kg ( $p < 0.001$ ), 0.12mg/kg ( $p < 0.001$ ), WGA-HRP-AuNP ( $p < 0.001$ ), 0.07mg/kg AuNP-ProTHP ( $p < 0.001$ ). There was significant drug effect for the MAX between the 0.07mg/kg dose and the following; 0.03mg/kg ( $p = 0.013$ ), WGA-HRP-AuNP ( $p = 0.027$ ), 0.07mg/kg AuNP-ProTHP ( $p = 0.013$ ) (**Figure 3.9**). Interestingly all control solutions at day 7 resulted in detectable recovery of the phrenic nerve, however the level of recovery of the LPN in several groups was negligible.

One-way ANOVA showed a significant drug effect on day 14 for the AUC between the 0.03mg/kg dose and the 0.12mg/kg dose ( $p = 0.030$ ). There was also a significant drug effect for the MAX between the 0.03mg/kg dose and the remaining two doses 0.12mg/kg ( $p = 0.001$ ) and 0.07mg/kg ( $p = 0.049$ ) (**Figure 3.10**).

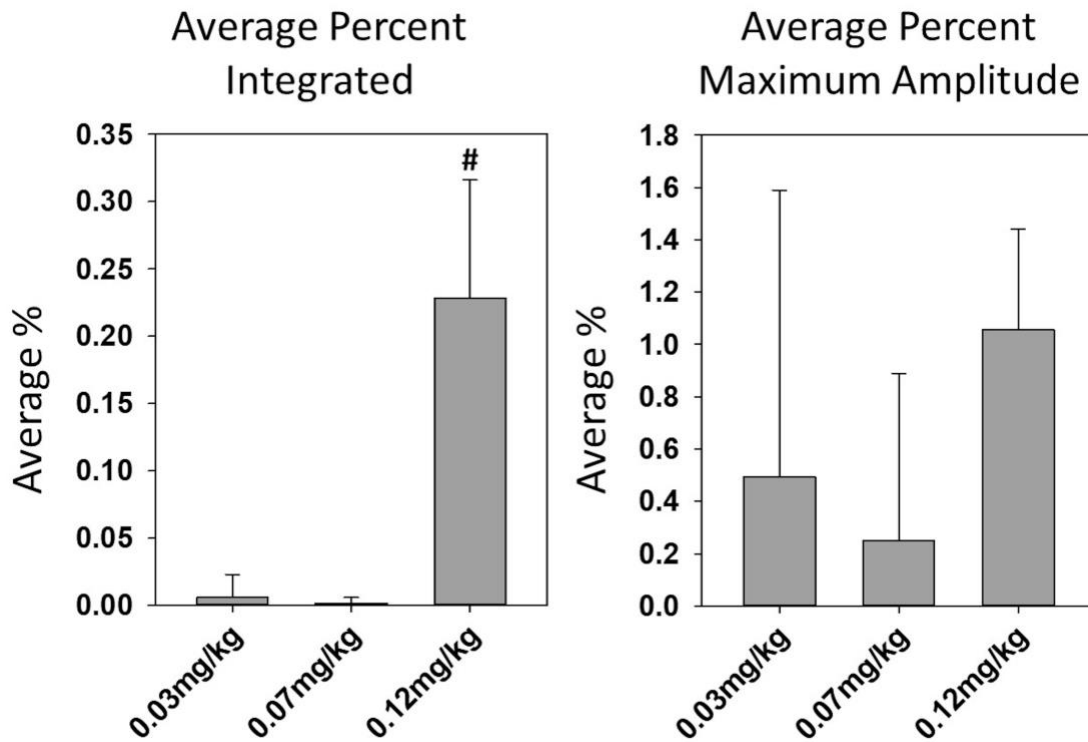


Figure 3-8 Day 3 Phrenic Nerve Recordings Analysis. The average percent integrated (AUC) and average percent maximum amplitude (MAX) of the LPN compared to the RPN. Statistical data consisted of neurograms from 18 rats. One way ANOVA showed significant drug effect (#) on day 3 between the 0.12mg/kg dose group and the remaining two groups, 0.03mg/kg dose and 0.07mg/kg dose for the AUC ( $p < 0.001$ ). No significance was detected from the MAX.

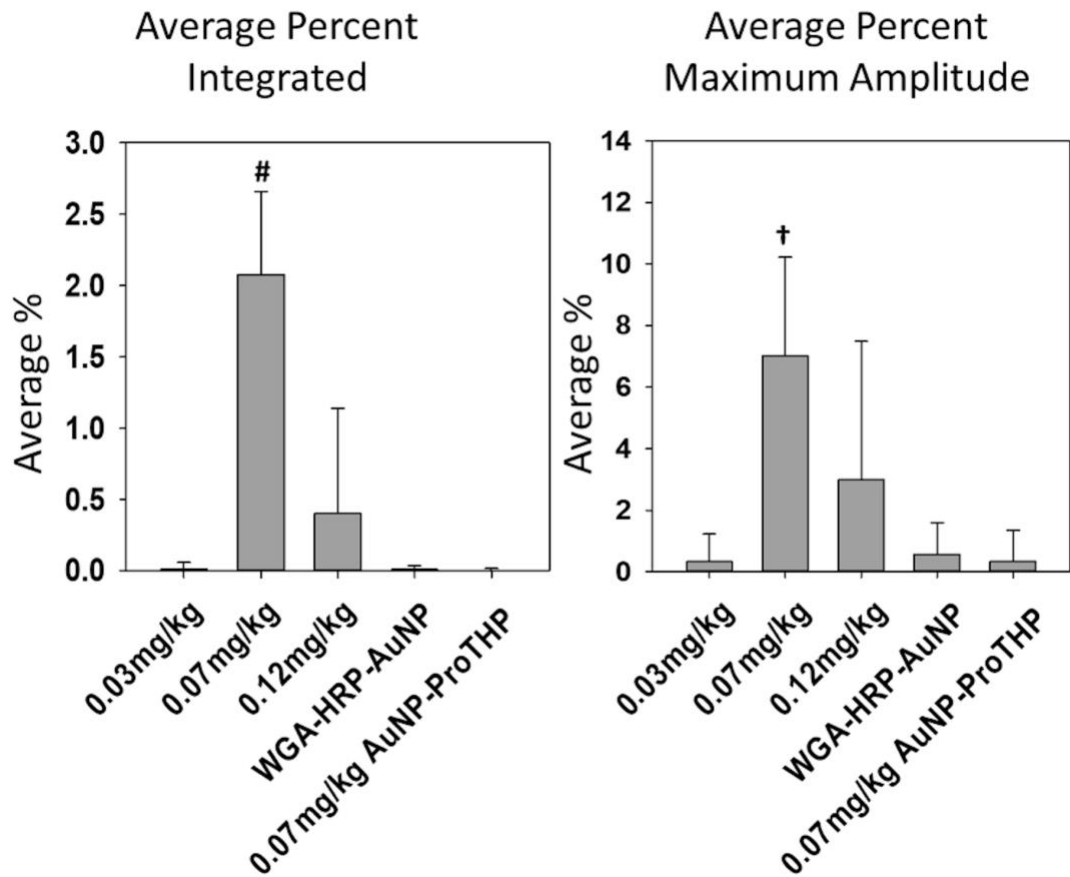


Figure 3-9 Day 7 Phrenic Nerve Recordings Analysis. The average percent integrated (AUC) and average percent maximum amplitude (MAX) of the LPN compared to the RPN. Statistical data consisted of neurograms from 18 rats. One way ANOVA showed significant drug effect on day 7 for the AUC between the 0.07mg/kg dose and the following; 0.03mg/kg ( $p < 0.001$ ), 0.12mg/kg ( $p < 0.001$ ), WGA-HRP-AuNP ( $p < 0.001$ ), 0.07mg/kg AuNP-ProTHP ( $p < 0.001$ ). There was significant drug effect for the MAX between the 0.07mg/kg dose and the following; 0.03mg/kg ( $p = 0.013$ , \*), WGA-HRP-AuNP ( $p = 0.027$ , \*\*), 0.07mg/kg AuNP-ProTHP ( $p = 0.013$ , \*\*\*).

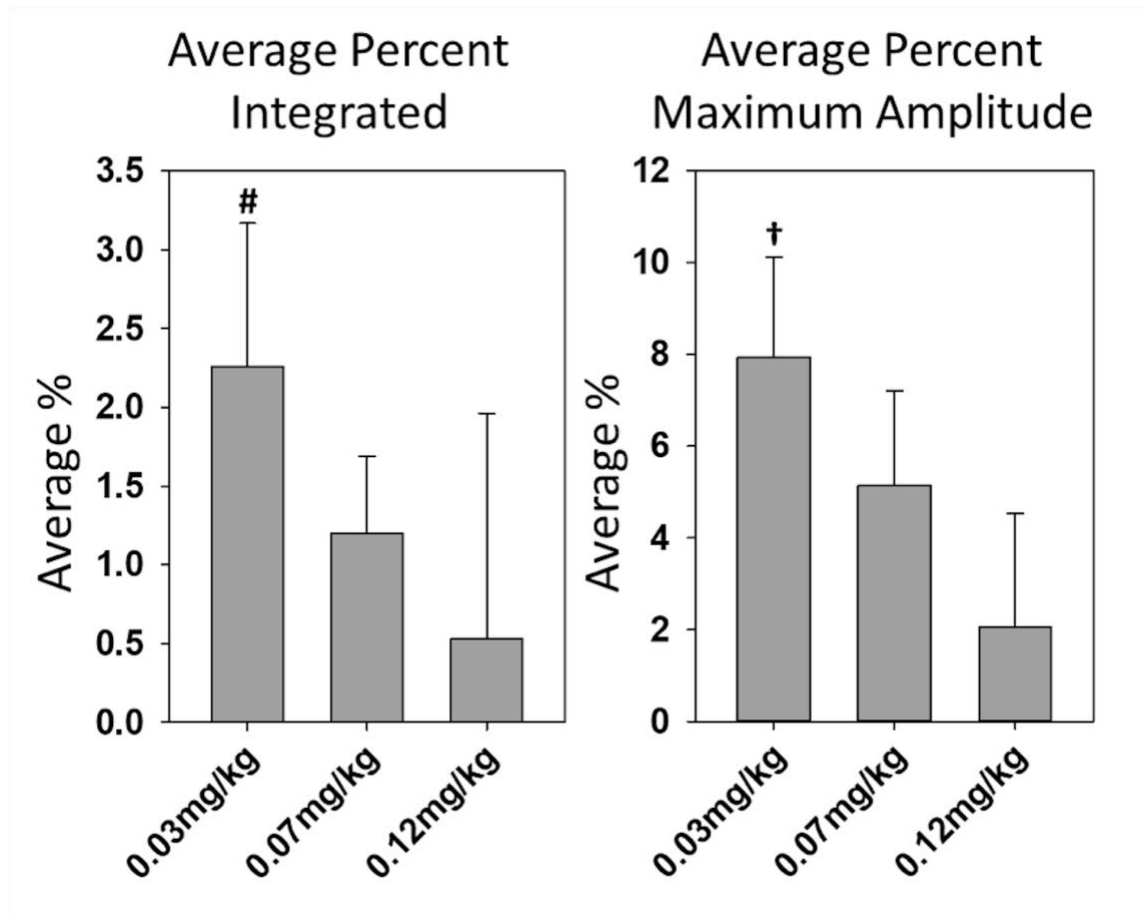


Figure 3- 10 Day 14 Phrenic Nerve Recordings Analysis. The average percent integrated (AUC) and average percent maximum amplitude (MAX) of the LPN compared to the RPN. Statistical data consisted of neurograms from 18 rats. One way ANOVA showed significant drug effect (#) on day 14 for the AUC between the 0.03mg/kg dose and the 0.12mg/kg dose ( $p=0.030$ ). There was also significant drug effect (†) for the MAX between the 0.03mg/kg dose and the remaining two doses 0.12mg/kg ( $p=0.001$ ) and 0.07mg/kg ( $p=0.049$ ).

Based on statistical analysis of the neurograms, each dose had a significant drug effect for the three different time points; 0.12mg/kg on day 3, 0.07 mg/kg on day 7, and 0.03 mg/kg on day 14. There was no single dose

tested that produced consistently significant recovery for all time points compared to the remaining doses. These data may reflect the inconsistent synthesis of the theophylline nanoconjugate.

### 3.4 Discussions

The WGA component of the nanoconjugate was identified by immunostaining in all three rats in the ipsilateral PN in the cervical spinal cord and bilaterally in the rVRGs in the medulla. This shows that the WGA-HRP component of the nanoconjugate was transported to the phrenic nucleus and transsynaptically to the rVRG. However, this technique does not confirm if theophylline is also located in the PN and rVRGs, which must occur for the theophylline to stimulate the CPP. This is due to the hydrolysable ester bond that enables the detachment of theophylline from the nanoparticle carrier. The primary drug release from ester-based drug linkers on nanomaterials is due to intracellular action of acid hydrolases in the acid compartments such as endosomes (pH 5.0-6.0) and lysosomes (pH 4.8). (120) Drug release from ester linkage to nanomaterials tends to be rather slow. For example, only 5% methotrexate was released over a period of 72 hours from

a dendrimer carrier in a serum medium at 37°C. (121) In another study, less than 5% of an antitumor drug SN38, a metabolite of irinotecan, released from its nanocarrier after 24 h in PBS buffer. (122) In a third study, the ester link of an immunosuppressive agent FK506 conjugated to dextran has a half-life of ~150 hours in a phosphate buffer (pH = 7.4). (123) We are currently conducting in vivo experiments to determine the biodistribution of the nanoconjugate as well as in vitro experiments simulating the in vivo environments to quantify the theophylline release profile from the nanocarrier.

The results from EMG analysis demonstrate that the nanoconjugate doses 0.0005, 0.0008, 0.0025, 0.03, 0.07, and 0.12mg/kg stimulate recovery of LHD activity detected as early as day 2 post injection and persisting up to 14 days. Again, based on literature it is likely significant amount of theophylline is still attached to the nanocarrier at the time of detection of LHD activity. Although current techniques are unable to confirm the presence of theophylline in the PN and rVRGs in this study, we confirmed the presence of WGA by immunostaining techniques. Recovery of the LHD

appearing by day 2 post injection corresponds with the time required for the uptake of WGA to the PN and rVRGs (94).

The control solutions, WGA-HRP-AuNP and 0.07mg/kg AuNP-proTHP did not produce LHD recovery in any of the rats tested. It is interesting to note that AuNP-proTHP was unable to produce LHD recovery even though proTHP was present. The explanation behind this remains unclear; however, without the WGA-HRP there is no transporter to initiate absorptive endocytosis at the phrenic nerve terminals following injection, therefore the drug should not have been delivered to the phrenic nuclei and rVRGs. It is possible for the theophylline to be released in the muscle and have a systemic effect but the dose administered via the nanoconjugate is a fraction of that needed to stimulate CPP recovery following systemic administration (97).

To better characterize the effect of the nanoconjugate, quantification of bilateral nerve recordings under standard conditions were compared between groups. The use of ketamine during a procedure to test for respiratory activity may appear problematic. However, in this study all recordings were sampled under the same protocol and there were no issues

detecting activity of the phrenic nerve on the non-injured side. Future, in the study by Giroux et al. (124), the effect of ketamine-xylazine anesthesia on respiration in SD rats was described. Rats used in the current study were 10-14 weeks of age (approximately 3 months) selected based on their weight. The study by Giroux et al. (124), demonstrates that the concern of respiratory depression following ketamine-xylazine use in younger adult rats (3 months) is only of valid within the first 15-30 minutes after intraperitoneal administration. At the 45-minute time point Giroux et al. (124), found that respiratory frequency had returned to pre-dosing levels in rats 3 months of age.

The variation of the AUC percent recovery observed for the 3 nanoconjugate doses over the course of the study might demonstrate the drug dose effect on respiration as the drug is metabolized and lasting effects over time. For all timepoints tested the 0.03mg/kg dose produced the highest percent of LPN activity with an AUC of 2.2%, however this is modest LPN recovery at best. Fortunately, in addition to theophylline there are multiple drugs known to enhance respiration following high SCI including DPCPX, a specific A<sub>1</sub> adenosine receptor antagonist (109, 125). Simultaneous



to this study AuNPs conjugated to WGA-HRP and DPCPX were being investigated (108). Injection of the DPCPX coupled nanoconjugate (0.15 $\mu$ g/kg DPCPX) produces an average percent recovery of 56.8% on day 7 and 72.4% on day 14 for the AUC of the LPN compared to the right phrenic nerve (108). Further investigation into the use of the DPCPX nanoconjugate is underway.

Throughout this work the chemical stability of the theophylline nanoconjugate for in vivo application became apparent. To chemically link theophylline to the AuNPs, a hydroxymethyl group was added to the theophylline creating proTHP, which then forms an ester bond with the capping agent, MSA, on the AuNPs following the Steglich reaction. The synthesized ProTHP was originally stored in vials in ambient air. We discovered that proTHP is reactive to moisture and hydrolyzes back to THP. When comparing 2 nanoconjugate batches (not used in the study), thermogravimetric analysis (TGA) detected a 5.7% weight variance, which is the difference of 105 molecules of proTHP attached to each AuNP. The hydrolysis tendency of proTHP poses significant challenges for the long-term storage of the product for in vivo applications. Following the discovery of the

apparent instability of proTHP we developed an experimental protocol to characterize the drug concentration for every batch with TGA to verify uniformity before in vivo use. The integrity of bond stability has been emphasized by others (126). It was decided to limit the use of the nanoconjugate for no longer than 30 days post synthesis. To further protect proTHP from hydrolysis we stored the newly synthesized proTHP in argon gas. We suggest that further investigation into the effects of the proTHP-bound nanoconjugate should take proTHP hydrolysis into consideration and carefully quantify the nanoconjugate chemical composition. Interestingly WGA-HRP-AuNP-DPCPX nanoconjugate used in the Minic et al. (108) study did not encounter the same issues stated above. In comparison to theophylline, DPCPX is more hydrophobic with an additional 5-carbon ring, a characteristic that may contribute to the chemical stability of pro-DPCPX against hydrolysis.

To increase the stability of the AuNP-proTHP bond, an alternative chemical bond was investigated. The nanoconjugate used in the work described herein used a methyl-binding site; we later identified a version of the proTHP compound that was coupled to the AuNPs using an ethyl-binding site. The

change in the binding site resulted in less proTHP molecules bound per AuNP requiring a higher AuNP concentration to maintain the same drug dosage. The effectiveness of the proTHP-coupled nanoconjugate via an ethyl bond was less than the methyl bond. Therefore, efforts to further investigate the ethyl version were abandoned due to low effectiveness.

There were notable differences in the AuNP concentration between solutions. To deliver an effective dose of proTHP, the AuNPs in solution were at a concentration of 0.8 mg Au/ml, but at this concentration, we noticed some degree of aggregation of the AuNPs. Nanoparticle aggregation in biological milieu occurs frequently and this limits nanoconjugate uptake by cells (e.g., via endocytosis). The concern of aggregation became evident during an ongoing biodistribution study, while euthanizing rats that received injections 8 weeks prior, the black appearance of the AuNPs, indicative of AuNPs aggregation, was still visible in the diaphragm. If the AuNPs are still visible in the muscle 8 weeks' post injection one must consider the likelihood of proTHP being delivered to the appropriate nuclei versus the proTHP bond degrading in the muscle. To explore this concern, the concentration of the AuNPs, along with the proTHP, was reduced in a stepwise manner to

determine if by lowering the AuNP concentration the probability of AuNP aggregation would be reduced and the probability of nanoconjugate uptake and proTHP delivery would increase. Reduction of the AuNP concentration in solution did result in a reduction of aggregation, as expected, which was confirmed visually by a color change from pinkish red to dark blue, however the effectiveness of proTHP failed to reach the level of recovery produced by the DPCPX-coupled nanoconjugate. Interestingly the therapeutic dose of DPCPX required only 0.1 mg Au/ml and therefore aggregation complications never arose during the DPCPX study.

### 3.5 Conclusions

WGA-HRP-AuNP-proTHP nanoconjugates are capable of significantly increasing the amount of LPN recovery when injected intradiaphragmatically immediately after C2Hx compared to the control treatments. Targeting delivery of theophylline reduces the therapeutic dose from 15mg/kg IV(97) to less than 0.2mg/kg. In doing so the restored left hemidiaphragm and left phrenic nerve function can be detected as early as 2 days and persists up to day 14 post injection. However, the WGA-HRP-AuNP-proTHP nanoconjugate used in this study fails to induce an equal amount of recovery following the

administration of the WGA-HRP-AuNP-DPCPX nanoconjugate (108). The clinical use of theophylline in humans led us to expend maximum effort to find a combination of the proTHP coupled nanoconjugate to reach the effectiveness of the DPCPX coupled nanoconjugate. However, the proTHP nanoconjugate continued to present stability concerns both in terms of its chemical stability in storage and colloidal stability post injection. The amount of proTHP per AuNP for effective recovery requires an AuNP concentration that is prone to aggregation, which limits the transport and cellular uptake of the nanoconjugate. While it is possible to overcome these stability issues by investigating alternative chemical conjugate chemistry, our lab has already yielded a more promising nanoconjugate, DPCPX-containing nanoconjugate (108). The effectiveness of the DPCPX coupled nanoconjugate well-surpassed those of proTHP, therefore all our future efforts will be directed towards the DPCPX-coupled nanoconjugate.

Lastly, the application of the WGA-HRP-AuNP nanoconjugate is not limited to the phrenic motor system. WGA-HRP has been applied over the decades to identify many neuromuscular pathways. In theory, injection of the WGA-HRP-AuNP nanoconjugate bound to a variety of substances could

hold promise for investigation and treatment of multiple disease and injury models.

## **CHAPTER 4 ANTI-CANCER DRUG CONJUGATED NANOPARTICLES INDUCED CELL DEATH IN TRIPLE NEGATIVE BREAST CANCER CELLS**

**This chapter is reproduced with permission from the Molecular cancer therapeutics 17, no. 12 (2018): 2586-2597. Saadat, Nadia, Fangchao Liu, Brittany Haynes, Pratima Nangia-Makker, Xun Bao, Jing Li, Lisa A. Polin, Smiti Gupta, Guangzhao Mao, and Malathy P. Shekhar. "Nano-delivery of RAD6/Translesion Synthesis Inhibitor SMI# 9 for Triple-negative Breast Cancer Therapy." And the Nanomedicine: Nanotechnology, Biology and Medicine 12, no. 3 (2016): 745-757. Haynes, Brittany, Yanhua Zhang, Fangchao Liu, Jing Li, Sarah Petit, Hend Kothayer, Xun Bao, Andrew D. Westwell, Guangzhao Mao, and Malathy PV Shekhar. "Gold nanoparticle conjugated Rad6 inhibitor induces cell death in triple negative breast cancer cells by inducing mitochondrial dysfunction and PARP-1 hyperactivation: Synthesis and characterization."**

### **4.1 Introduction**

The human homologues of yeast Rad6, HHR6A and HHR6B (referred as Rad6A and Rad6B) play a fundamental role in DNA damage tolerance pathway (127-130), and the ubiquitin conjugating activity of Rad6 is essential for this function (131). The Rad6B homologue is overexpressed in metastatic and chemo-resistant breast carcinomas (132-134). Constitutive overexpression of Rad6B in nontransformed human breast epithelial cells induces tumorigenesis and resistance to cisplatin and doxorubicin (132, 135, 136). Conversely, Rad6B silencing renders cells chemo-sensitive (136), implicating the relevance of Rad6 in transformation and drug resistance, and the potential therapeutic benefit of inhibiting Rad6. We have recently reported the development of a novel Rad6-selective small molecule inhibitor SMI#9 that inhibits Rad6 ubiquitin conjugating activity (137). SMI#9 treatment suppresses proliferation and migration and induces apoptosis in breast cancer cells but spares normal breast cells (137). However, SMI#9 has poor aqueous solubility that limits its therapeutic efficacy. Here we developed a drug delivery system that would improve its solubility and uptake.

Gold nanoparticles (AuNPs) are ideal drug delivery scaffolds because they are nontoxic and nonimmunogenic (138, 139), and have good biocompatibility and stability (140). Surface modification allows AuNPs to be readily functionalized with multiple agents including chemotherapy, oligonucleotides and proteins making them good delivery vehicles (141). Several AuNP-based drugs have been developed by CytImmune with their lead drug Aurimune (TNF $\alpha$  bearing PEGylated gold nanoparticles) in clinical trials.

This chapter will describe the synthesis of SMI#9-tethered AuNPs using a chemistry that allows intracellular release of SMI#9. SMI#9-AuNPs were characterized for size and ligand conjugation, and intracellular release of conjugated SMI#9 by Fourier transform infrared spectroscopy (FTIR) and liquid chromatography coupled tandem mass spectrometry (LC-MS/MS). Intracellular uptake, localization, cytotoxicity and molecular responses to AuNP-conjugated SMI#9 were evaluated in triple negative breast cancer (TNBC) cells as TNBC represents a heterogeneous disease with poor clinical outcomes and few targeted therapy options as they lack estrogen receptor, progesterone receptor and Her2/neu amplification. We analyzed the



responses to conjugated and free SMI#9 in two major subtypes of TNBC, mesenchymal and basal types (142) to authenticate the functionality of AuNP-tethered SMI#9. We show that the mesenchymal subtype is sensitive to SMI#9-AuNP and that modified SMI#9 released from AuNP acts similarly to unconjugated parent SMI#9.

## 4.2 Experimental methods

### 4.2.1 Materials

Sodium bicarbonate ( $\text{NaHCO}_3$ ), di-tert-butyl dicarbonate ( $(\text{Boc})_2\text{O}$ ), 37% formaldehyde (HCHO) solution, triethylamine ( $\text{Et}_3\text{N}$ ), tetrahydrofuran (THF), gold(III) chloride trihydrate ( $\text{HAuCl}_4 \cdot 3\text{H}_2\text{O}$ ), sodium citrate tribasic dihydrate, mercaptosuccinic acid (MSA), sodium borohydride ( $\text{NaBH}_4$ ), dimethyl sulfoxide (DMSO), 1-ethyl-3-(3-dimethylaminopropyl)carbodiimide (EDC), N-hydroxysuccinimide (NHS), and 4-dimethylaminopyridine (DMAP) were purchased from Sigma-Aldrich.

### 4.2.2 Synthesis of gold nanoparticle (AuNP) and conjugation of Rad6 inhibitor SMI#9 to AuNP

Mercaptosuccinic acid (MSA)-capped AuNP (MSA-AuNP) was synthesized as described as followed. Briefly, ice-cold 0.1 M  $\text{NaBH}_4$  solution

was added with vigorous stirring to a solution of 0.25 mM  $\text{HAuCl}_4 \cdot 3\text{H}_2\text{O}$  and 0.25 mM trisodium citrate. The pH was adjusted to 11, and 50 mg MSA was added. The final solution was concentrated to 2.5 g (gold)/L by centrifugation using 10,000 MW Amicon filters. SMI#9 was modified to enable AuNP conjugation via an ester bond. To modify SMI#9, 1.5 mg SMI#9 was dissolved in 0.5 ml tetrahydrofuran (THF; 50%, v/v) followed by addition of 10 mg of  $\text{NaHCO}_3$  and 2.6 mg di-tert-butyl dicarbonate  $(\text{Boc})_2\text{O}$ . After 30 min reaction, 5  $\mu\text{l}$  of HCHO and 5  $\mu\text{l}$  of triethylamine ( $\text{Et}_3\text{N}$ ) were added and the hydroxymethylation reaction was allowed to proceed for 48 h. The solution was then added to AuNP (2.5 g/L gold concentration) solution. The pH of the solution was adjusted to 4.7 with MSA, and 2 mg 1-ethyl-3-(3-dimethylaminopropyl) carbodiimide (EDC), 0.2 mg 4-dimethylaminopyridine (DMAP), and 2 ml dimethyl sulfoxide (DMSO) were added to catalyze the esterification reaction. After 40 h, the final solution was concentrated to 0.2  $\text{g mL}^{-1}$  by centrifugation using 10,000 MW Amicon filters and desalted by exchanges with deionized water.

#### 4.2.3 Characterization of AuNP–drug conjugates

SMI#9 conjugated to AuNP was characterized by thermogravimetric analysis (TGA) on an SDT-Q600 Thermo-Gravity Analyser using air as the supporting gas. The air flow rate was maintained at 100 ml/min, and sample heated from 25 to 800 °C at a rate of 10 °C/min. AuNP “solutions” were also characterized by UV–vis spectroscopy with a Varian Cary® 50 spectrometer in 2 mm optical path cells, and by transmission electron microscopy (TEM) at 200 kV with a JEOL JEM-2010 microscope equipped with a Gatan multiscan CCD camera.

Dynamic light scattering (DLS) and zeta potential were measured using a Malvern Nano-ZS. The Z-average hydrodynamic diameter (HD), polydispersity index (PDI), and zeta potential were measured at 25 °C. 15 scans were performed in each measurement.

#### 4.2.4 Cell lines and culture

MDA-MB-231 (BRCA1 wild-type) and MDA-MB-468 (BRCA1 wild-type) human TNBC cells were purchased from ATCC, and SUM1315 (BRCA1 mutant) TNBC cells were purchased from Asterand. All lines were maintained in DMEM/F12 (Invitrogen) containing 5% FBS. Following authentication by cell

bank (short tandem repeat PCR) and Mycoplasma screening (MycoAlert, Lonza), several aliquots of cells were frozen and used within 10 passages.

4.2.5 SMI#9 and SMI#9-AuNP uptake and intracellular release of the free drug from AuNP conjugate

MDA-MB-231 ( $3 \times 10^5$ ) cells were plated in 35 mm dishes and exposed to various doses of SMI#9-AuNP or untreated for 24-48 h. Cultures were rinsed, lysed by freeze-thaw cycles in cold hypotonic buffer, and clarified by centrifugation at 10,000g. Aliquots of clarified lysates were analyzed by FTIR spectroscopy using control lysates spiked with free SMI#9 as reference. To determine intracellular release of modified SMI#9 from nanoparticles, SUM1315 ( $2 \times 10^6$  cells/100 mm dish) cells were exposed for 8 or 24 h to 5  $\mu$ M free SMI#9, 5  $\mu$ M SMI#9-AuNP or the corresponding amount of blank-AuNP, or untreated. Cultures were rinsed in ice-cold phosphate buffered saline (PBS), lysed with cold 80% methanol and clarified by centrifugation at 10,000g for 10 min at 4 °C. Aliquots of supernatants were subjected to high performance liquid chromatography (HPLC) coupled with tandem mass spectrometry (LC-MS/MS) analysis.

4.2.6 Mitochondrial assay

The impact of free SMI#9 or SMI#9-AuNP on mitochondrial membrane potential ( $\Delta\psi_m$ ) on SUM1315 and HCC1937 TNBC cells was assessed using JC-1 (Mitocapture, Biovision, Mountainview, CA), a potentiometric green fluorescent dye that shifts to red fluorescence within mitochondria with a normal negative  $\Delta\psi_m$ . Briefly, cells were incubated with the MitoCapture reagent for 15 min at 37 °C and imaged by fluorescence microscopy. The percent of cells showing > 5 punctate J-aggregates was scored by counting three-five fields of 50-100 cells in each field. To quantitate mitochondrial membrane potential changes,  $20 \times 10^3$  SUM1315 or HCC1937 cells were seeded in 96-well plate and treated for 48 h with 5  $\mu$ M SMI#9-AuNP or blank-AuNP. Cells were then incubated with 10  $\mu$ M JC-1 for 30-60 min, and the red and green fluorescence intensities of JC-1 were measured at excitation/emission = 490/525 nm and 490/590 nm with a Synergy 2 fluorescence reader. Results were expressed as the ratio of red to green fluorescence.

#### 4.2.7 LC/MS-MS analysis of SMI#9

SMI#9 concentrations in the plasma and tumors were determined by LC/MS-MS. Briefly, tumors (50–100 mg) were homogenized, and plasma or

tissue homogenates were extracted with ethyl acetate. The organic phase was dried down and reconstituted in the mobile phase [methanol/0.45% formic acid in water (60:30, v/v)]. LC/MS-MS was performed on a Waters Xevo TQ-XS LC/MS-MS system with a Waters Xterra MS C18 column and isocratic elution with the mobile phase. SMI#9 was monitored at the positive electrospray ionization mode at  $m/z$  366.69 > 150.1 mass transitions.

#### 4.2.8 Inductively coupled plasma mass spectrometry analysis of gold

Organs and tumors were digested with aqua regia (hydrochloric acid: nitric acid, 3:1 v/v) and analyzed using an Agilent 7700× inductively coupled plasma mass spectrometry (ICP-MS) equipped with an Agilent ASX-500 series autosampler. External calibration using standards with internal standard correction of bismuth (Bi) was performed prior to the measurements. AuNP biodistribution data were expressed as a percentage of injected dose of gold/gram dry tissue.

#### 4.2.9 Statistical analysis

Each experiment was performed in triplicate and reproduced at least three times. Data are expressed as mean  $\pm$  S.D, and  $P < 0.05$  determined by Student's t-test was considered to be statistically significant.

### 4.3 Results

#### 4.3.1 AuNP conjugates characterization

The chemical compositions of AuNP and SMI#9-AuNP were determined by TGA. **Figure 4.1A** shows the TGA curves of MSA-AuNP (blank-AuNP) and MSA-AuNP conjugated SMI#9 (SMI#9-AuNP) with weight loss of 6.15% and 13%, respectively, at 800 °C. The number of gold atoms was based on size determined by transmission electron microscopy (TEM) and gold density. The weight of 1 molar AuNP (W) with a diameter (D) of 4 nm can be estimated using the following formula based on the bulk density of gold ( $\rho$ ):

$$W = \rho \times \frac{1}{6} \pi D^3 \times 6.022 \times 10^{23} = 19.3 \frac{\text{g}}{\text{cm}^3} \times \frac{1}{6} \pi (4 \times 10^{-7} \text{ cm})^3 \times 6.022 \times 10^{23} = 3.89 \times 10^5 \text{ g/mol}$$

The molecular weight of MSA ( $\text{C}_4\text{H}_6\text{O}_4\text{S}$ ) and SMI#9 ( $\text{C}_{17}\text{N}_6\text{H}_{14}\text{O}_4$ ) are 150 g/mol and 366 g/mol, respectively. The weight loss, 93.85%:6.15% = AuNP:MSA, corresponds to 170 MSA molecules per AuNP as calculated below:

$$\text{No. of MSA molecules} = \frac{6.15}{150} \times \frac{3.89 \times 10^5}{93.85} = 170$$

The area of MSA coverage on AuNP (A) is calculated below:

$$A = \frac{\pi D^2}{\text{No. of MSA molecules}} = \frac{\pi(4\text{nm})^2}{170} = 0.296\text{nm}^2 = 29.6\text{\AA}^2$$

The weight loss, 100%:6.6%:8.3% = AuNP: MSA:SMI#9, corresponds to 88.2 SMI#9 as calculated below:

$$\text{No. of SMI\#9 molecules} = \frac{8.3}{366} \times \frac{3.89 \times 10^5}{100} = 88.2$$

This means that 26% of all possible reactive sites (170 MSA molecules carrying 340 –COOH groups) are conjugated with SMI#9.

**Figure 4.1B** shows the UV-*vis* spectra of AuNPs before and after conjugation with modified SMI#9. The surface plasmon resonance (SPR) absorption peak of freshly prepared AuNPs is 508 nm, which corresponds to AuNP diameter range of 3-5 nm. However, upon conjugation with modified SMI#9, the SPR absorption peak broadened and shifted to 524 nm, which is indicative of particle aggregation. The size of SMI#9-AuNPs was also determined by TEM (**Figure 4.1C**) and AFM (**Figure 4.1D**) which showed a size of 32 nm and  $40.2 \pm 1.4$  nm, respectively, that is consistent with aggregation. DLS further verified the average size of SMI#9-AuNP nanoconjugate at 41 nm as compared to 4.8 nm for AuNP. The zeta potential of MSA-capped AuNP changed from -41 mV to -16.2 mV after conjugation with SMI#9. The



decrease in surface charge is the result of SMI#9 conjugation to highly charged MSA.

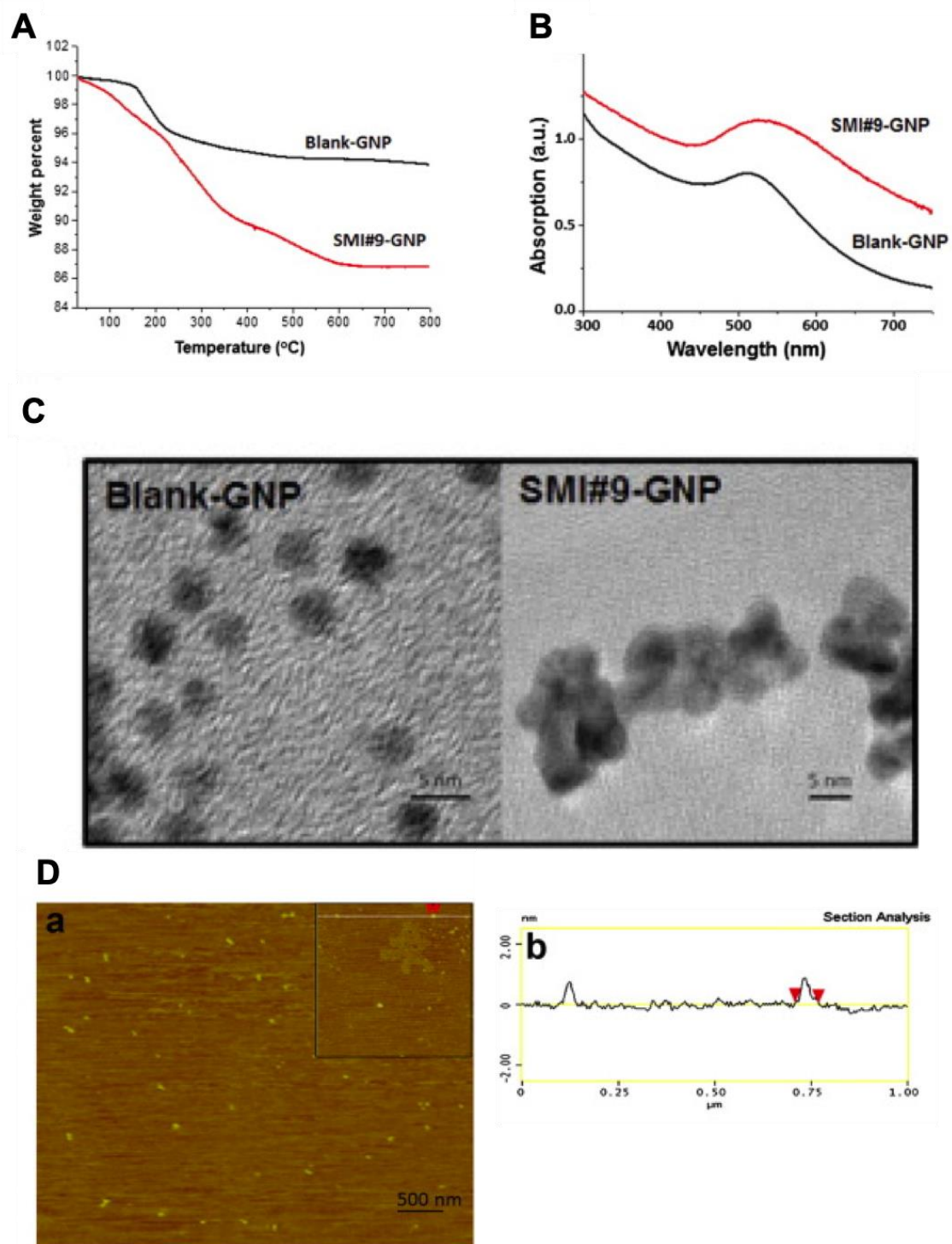


Figure 4-1 SMI#9-AuNP characterization. A) thermogravimetric analysis. B) UV-vis spectroscopy. C) Transmission electron microscopy. D) Atomic force microscopy (AFM). (a) AFM height of SMI#9-AuNP, Z-range = 5 nm. Inset in

panel D(a) shows a white line from where the AFM sectional height profile in panel D(b) was taken and shows 39 nm particle width (two arrows).

#### 4.3.2 Intracellular SMI#9-AuNP uptake and releases

To determine SMI#9-AuNP uptake and intracellular release of the conjugated SMI#9, MDA-MB-231 or SUM1315 cells were exposed to SMI#9-AuNP, blank-AuNP, SMI#9 or untreated, and cell lysates analyzed by FTIR or LC-MS/MS. Control cell lysates spiked with (parent) SMI#9 were included as reference controls. FTIR analysis of SMI#9 (**Figure 4.2A**), and lysates prepared from SMI#9-AuNP treated MDA-MB-231 cells or MDA-MB-231 control lysates spiked with SMI#9 showed characteristic nitro group banding at  $\sim 1550\text{ cm}^{-1}$ , indicative of SMI#9 presence (**Figure 4.2B**).

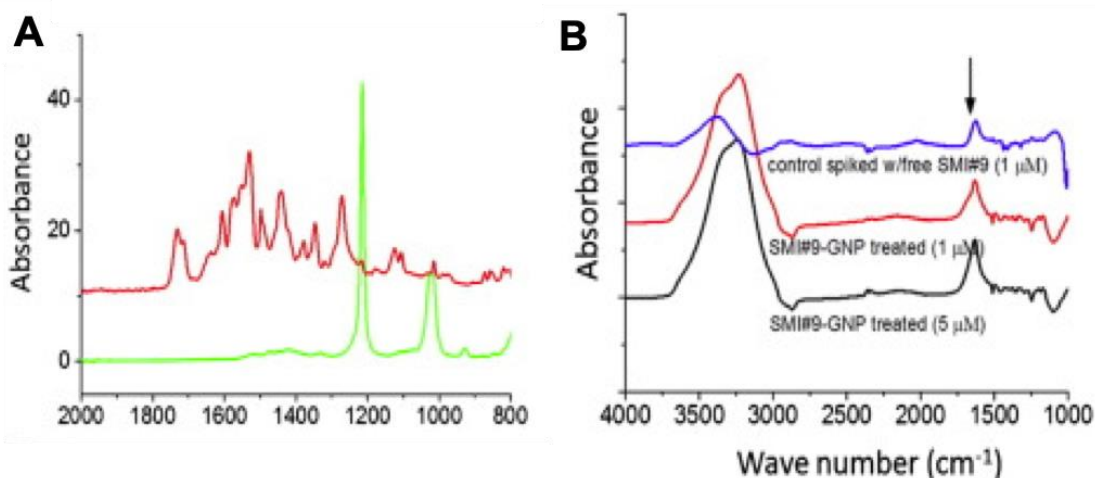


Figure 4-2 FTIR spectra of A) chloroform/methanol (11:1, v/v) without (green) and with SMI#9 (red). And of B) SMI#9-AuNP treated and control MDA-MB-231 lysates spiked with parent SMI#9. Arrow indicates nitro banding.

SMI#9 was modified to enable conjugation to AuNP via an ester bond (**Figure 4.3 A, a**). Intracellular hydrolysis would result in release of modified SMI#9 with the molecular weight of 396.3, which would theoretically produce parent ions at 397.3 ( $[M+H]^+$ ) and product ions at 150.1 (**Figure 4.3 A, b and c**). Although no peak was detected under the transition of 397.3 > 150.1 in SMI#9-AuNP treated cells, a strong peak was detected under  $m/z$  381.3 > 150.1 transition in SMI#9-AuNP treated cells (at both 8 and 24 h) but not in blank-AuNP or untreated control cultures (Figure 4.? C). Release of drug with 381.3 molecular mass could theoretically arise by dehydroxylation of hydroxymethylated SMI#9; however, the precise structure of intracellularly released drug and its metabolic processing is under investigation. The peak signals were stronger at 8 h as compared to 24 h, suggesting rapid intracellular processing. The positive control cells treated with free (parent) SMI#9 showed the expected peak under  $m/z$  366.69 > 150.1 transition. These results suggest efficient uptake and rapid intracellular processing of the chemically modified SMI#9-AuNP conjugates.

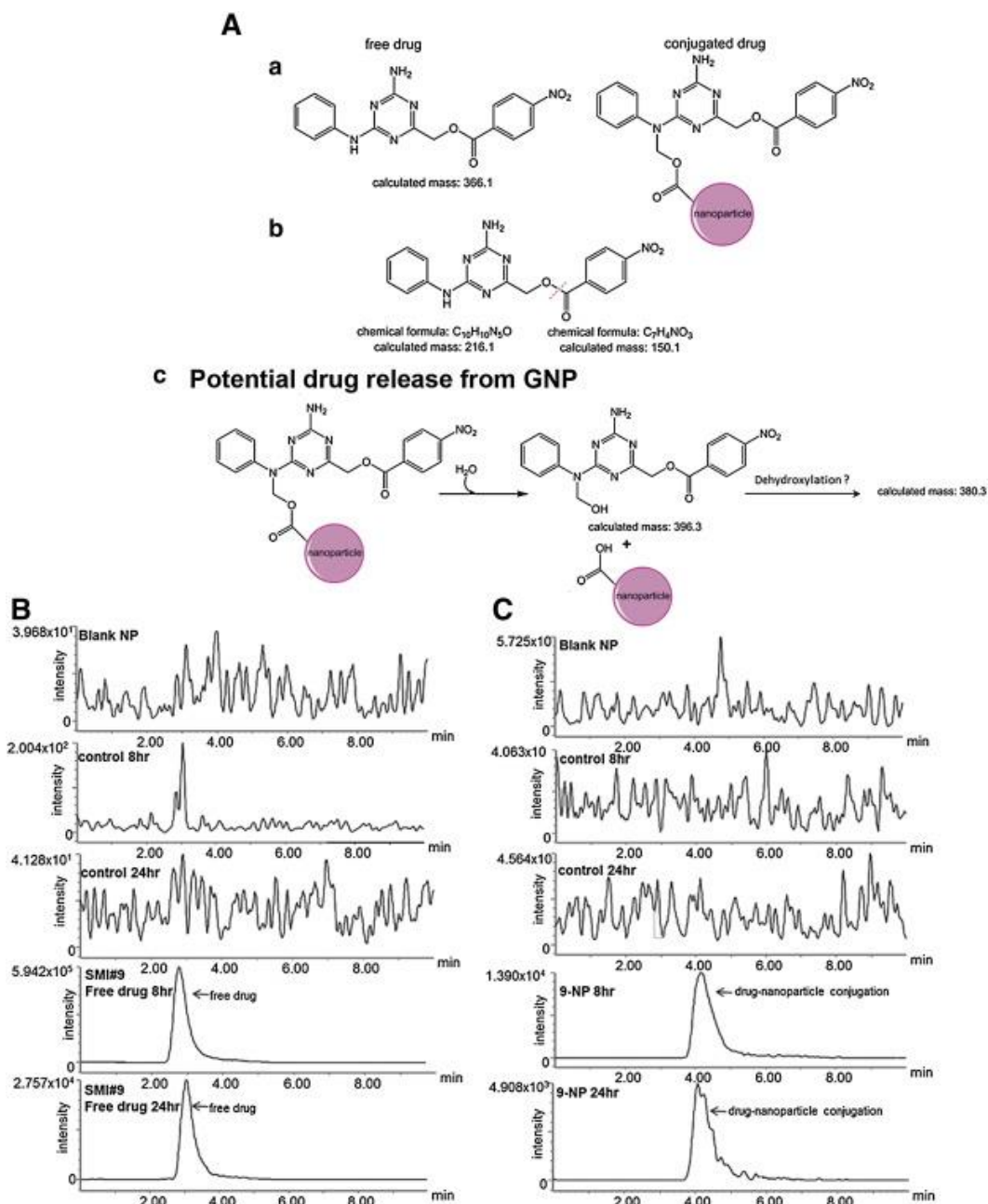


Figure 4-3 LC-MS/MS analysis of SMI#9 release. A) (a) Chemical structures of parent SMI#9 (MW = 366.1), and AuNP-conjugated hydroxymethylated SMI#9 (MW = 396.3). (b) Predicted fragmentation pathway of SMI#9 under the MS condition. (c) Proposed mechanism of SMI#9 release from AuNP conjugate. B) and C) Chromatograms of SUM1315 extracts prepared at 8 or 24 h from untreated (control), or cells treated with blank-AuNP (blank NP), 5  $\mu$ M SMI#9 (B), or 5  $\mu$ M SMI#9-AuNP (C, 9-NP). Samples were monitored at

m/z 366.69 → 150.1 for SMI#9 (B) or m/z 381.3 → 150.1 for SMI#9 released from AuNP (C).

#### 4.3.3 In vivo evaluation of SMI#9 and SMI#9-AuNP

SMI#9 concentrations in plasma were measured by LC-MS/MS at 5 min to 24 h after a single intravenous injection of SMI#9 or PEGylated SMI#9-AuNP. Following injection of the unconjugated drug, SMI#9 achieved maximum plasma concentration ( $C_{max}$ ) of ~74 nM at 5 min, and was rapidly cleared by 30 min (Figure 4.4A). In contrast, following injection of SMI#9-AuNP, SMI#9 was slowly released and achieved  $C_{max}$  of ~1200 nM at 8 h (Figure 4.4B). These data suggest that SMI#9 is not only released from the PEGylated SMI#9-AuNP conjugates but can also achieve higher systemic exposure as compared to the unconjugated SMI#9.

Post-synthesis surface modification of SMI#9-AuNP with PEG was performed as PEG improves colloidal stability and prevents aggregation (143, 144). Furthermore, PEG reduces adsorption of cellular proteins and increases the circulation time of nanoparticles. We first determined whether PEGylated SMI#9-AuNP similarly sensitizes TNBC cells as non-PEGylated SMI#9-AuNP. SUM1315 cells were treated with various concentrations of

SMI#9-AuNP or PEGylated SMI#9-AuNP (or blank-AuNP) and the responses measured by MTT assays. SUM1315 cells responded similarly to both formulations with GI50 values (based upon SMI#9 concentration) of  $\sim 0.75$ - $1 \mu\text{M}$ , verifying that tethering of PEG did not significantly affect the activity of SMI#9 payload (Figure 4.4C). To compare the in vivo effects of SMI#9 and PEGylated SMI#9-AuNP or blank-AuNP on TNBC xenografts, MDA-MB-468 or SUM1315 TNBC cells were orthotopically implanted in female nude mice. When the tumors reached  $\sim 150 \text{ mm}^3$ , mice were randomized and treated twice weekly with vehicle, SMI#9, PEGylated SMI#9-AuNP or blank-AuNP. To overcome SMI#9 solubility limitations and to facilitate easy tumor access, unconjugated SMI#9 (or vehicle) was administered intratumorally whereas blank-AuNP and SMI#9-AuNP were injected intraperitoneally to assess tumor accessibility and bioavailability. Animal body weights were measured twice weekly to monitor animal health. SMI#9 or SMI#9-AuNP treatments significantly inhibited growth of MDA-MB-468 and SUM1315 xenografts as compared to the corresponding vehicle or blank-AuNP control groups ( $P \leq 0.05$ ; Figure 4.4D and E). Compared to the control tumors that contained mitotic cells, H&E analysis of SMI#9 and SMI#9-AuNP treated MDA-MB-468

(Figure 4.4F) and SUM1315 (Figure 4.4G) tumors showed sparsely populated tumor tissues containing apoptotic cells (arrows in insets of Figure 4.4F and G). H&E staining showed lung tissues with normal architecture in both control and SMI#9 or SMI#9-AuNP treated groups (Figure 4.4H). The data in Figure 4.4I show that SMI#9 and SMI#9-AuNP treated mice maintain body weights comparable to vehicle or blank-AuNP controls suggesting drug tolerance without overt signs of toxicity.



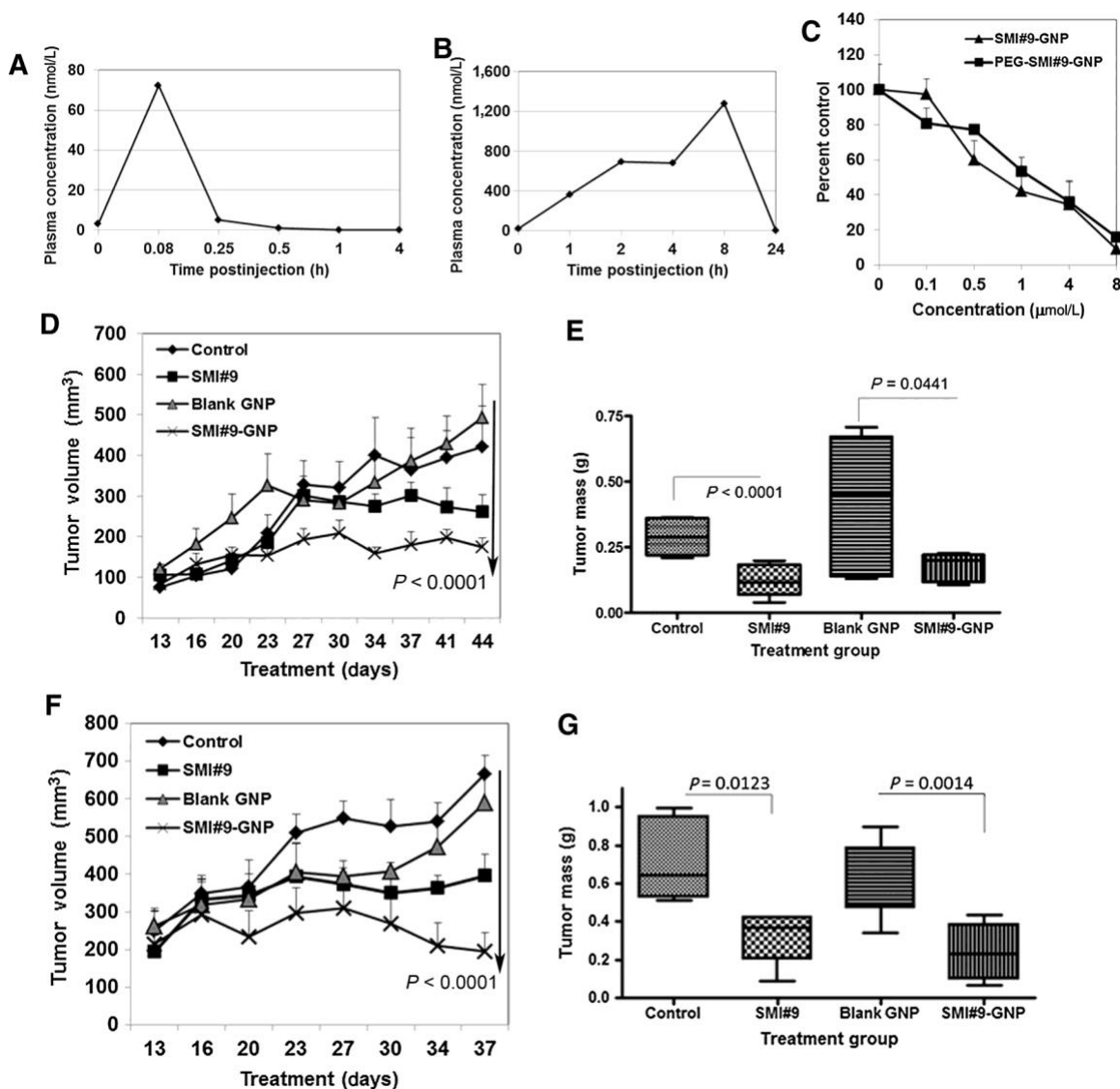


Figure 4-4 SMI#9-AuNP inhibits TNBC growth. Pharmacokinetic analysis of unconjugated SMI#9 (A) and PEGylated SMI#9-AuNP (B) administered intravenously at 5 mg/kg body weight. C) In vitro activities of SMI#9-AuNP and PEGylated SMI#9-AuNP on SUM1315 cell proliferation. Results are mean  $\pm$  SD of triplicates from two independent experiments. Tumor volumes (mean  $\pm$  SEM;  $n = 6$  mice/group) of MDA-MB-468 (D) or SUM1315 (F) xenografts treated with unconjugated SMI#9 (1.5 mg/kg body weight), PEGylated SMI#9-AuNP (0.85 mg/kg body weight), or controls.  $P < 0.0001$  by one-way ANOVA. Vertical scatter plots of excised tumor mass of MDA-MB-468 (E) and SUM1315 (G) xenografts.

#### 4.3.4 Biodistribution of SMI#9-AuNP

To verify whether the tumor growth inhibition in SMI#9-AuNP-treated mice resulted from SMI#9 release from the nanoconjugate, we quantitated SMI#9 levels in tumor fragments collected at sacrifice by LC/MS-MS. Compared with the control groups, measurable amounts of SMI#9 were detected in SUM1315 and MDA-MB-468 tumors treated with SMI#9 or SMI#9-AuNP (**Figure 4.5 A and B**). However, there was variability in the detected levels, which could have potentially resulted from tumor tissue samplings as tissue fragments rather than whole tumors were used for analysis or from loss of SMI#9 resulting from therapy-induced tumor cell death in the responsive tumors.

Next, we determined the biodistribution and retention of AuNPs in tumor and organ tissues collected at sacrifice (**Figure 4.5 C**) by ICP-MS. The injected dosage of gold was calculated on the basis of the TGA data: weight ratio of gold to SMI#9 equivalent to 1:0.083 in the nanoconjugate (143). Thus, a SMI#9 dosage of 0.85 mg/kg body weight corresponds to gold dosage of 10.24 mg. On the basis of 0.02 kg average weight of mouse, the gold dosage

per injection is 0.2 mg and the total gold injected is 1.8 mg after nine injections. Among the tissues analyzed, liver and tumors showed the highest accumulation of gold ranging from 0.19% to 0.4%; however, there were no significant differences in gold content between livers and tumors of blank AuNP and SMI#9-AuNP groups (**Figure 4.5 C**). Despite multiple injections, this accumulation was comparable with those reported for a single injection (145). AuNP bioaccumulation in liver and spleen are regulated by the reticuloendothelial system (RES; (146)). The low levels of AuNP accumulation in the spleen potentially reflect the low AuNP doses administered in our study and/or the time intervals between the injections. Furthermore, because the tissue samples were collected 3 days after the last AuNP injection, larger increases in gold depositions were perhaps not observed because of active renal clearance. The AuNPs used here are 5-nm particles with a hydrodynamic size of 41 nm following SMI#9 conjugation. Because the kidney filtration threshold is 6–8 nm (147), AuNPs that were stripped off their SMI#9 cargo would be small enough to be cleared by the kidneys leaving behind the non-biodegraded SMI#9-AuNPs. Because tumors contained higher levels of gold, it is likely that enhanced permeability and retention

(EPR) effects from leaky vasculature in the tumors contributed to accumulation of gold in the tumors (Figure 4.5 C).

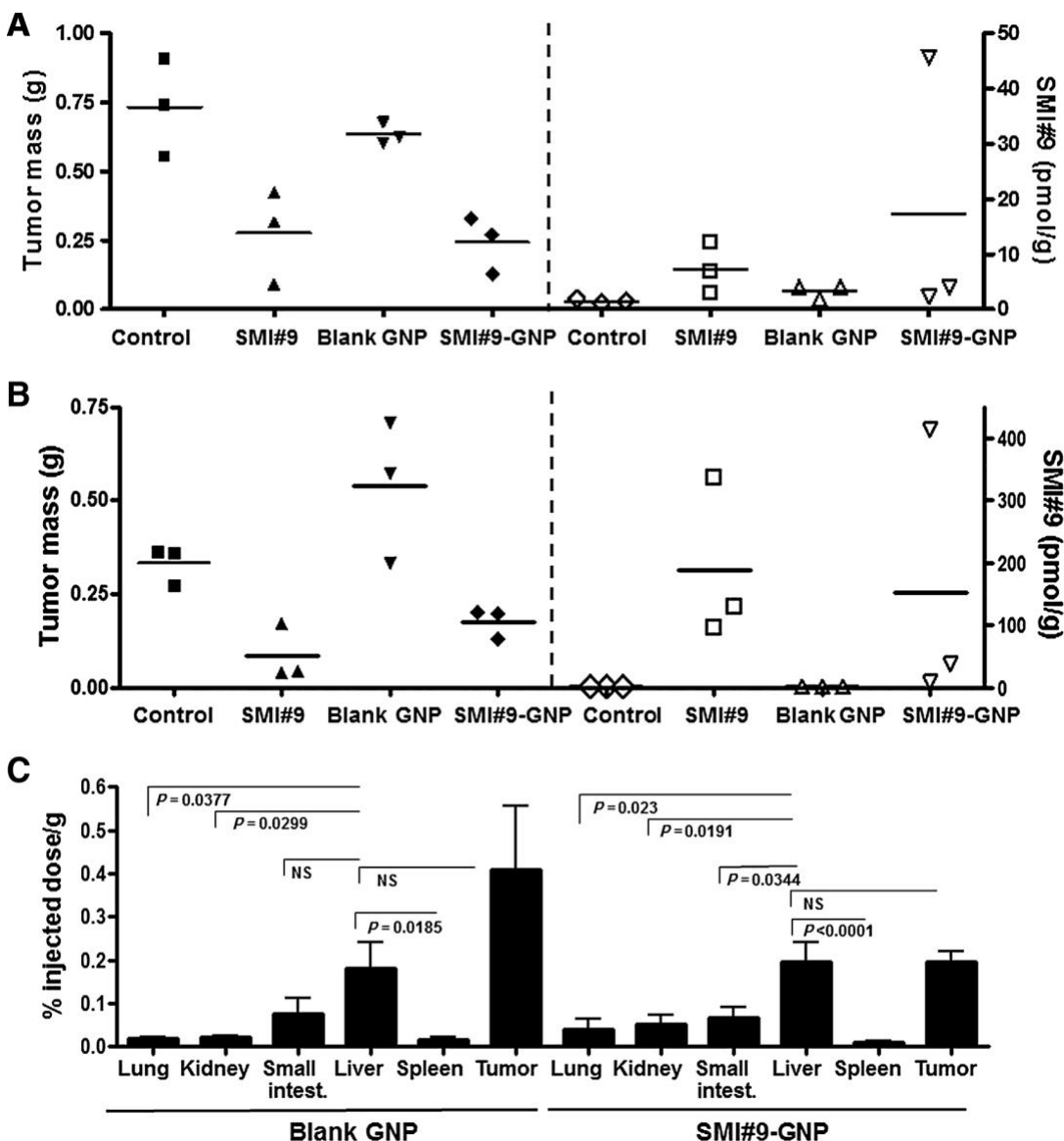


Figure 4-5 SMI#9 and gold biodistribution analysis. LC/MS-MS analysis of SMI#9 tumor levels and corresponding vertical scatter plots of SUM1315 (A) or MDA-MB-468 (B) excised tumor mass at sacrifice. C) ICP-MS analysis of accumulated gold in the indicated tissue. Data were analyzed by one-way ANOVA and two-tailed Student *t* test; NS, no significant difference.

#### 4.4 Discussions

Intratumoral injection of SMI#9, a clinically unsuitable mode of drug administration, was necessary because of its poor solubility and poor pharmacokinetic properties. Delivery of SMI#9 as a prodrug–AuNP conjugate not only greatly improved its circulation stability and drug exposure, but also allowed for a clinically acceptable mode, that is, systemic administration of the drug because of improved solubility. In this work we evaluated the toxicity, biodistribution, and therapeutic activity of systemically administered PEGylated SMI#9-conjugated AuNPs to assess their utility as a drug delivery platform for treatment of BRCA1 wild-type and BRCA1-mutant TNBCs.

Perrault and colleagues (148) tested AuNPs with size range of 10–100 nm and found that although AuNPs with hydrodynamic diameter of 60–100 nm with PEGylation efficiently utilize EPR effect for enhanced tumor accumulation, these larger AuNPs penetrated weakly into the tumors and localized in the perivascular regions. AuNPs are generally considered nontoxic when the size is larger than 2 nm, whereas ultrasmall nanoparticles

are found to be toxic (149). AuNPs of larger size (35–50 nm) were found to enter cells more efficiently without toxicity than small nanoparticles (1.4 nm; (150)). Consistent with these data, our results show that 41-nm SMI#9-AuNPs are taken up efficiently by tumor cells and display no apparent toxicity. Quantitative analysis of AuNP biodistribution by ICP-MS analysis showed higher accumulation of gold in tumors and liver as compared with other organs of SMI#9-AuNP and blank AuNP-treated mice. These data are in agreement with other studies that showed maximal accumulation of nanoparticles in the liver regardless of their size, shape, dosage, or composition (146, 151, 152). However, our data suggest that the AuNPs are actively cleared because the amounts of gold deposited in the liver and other tissues despite repeated injections resemble those in mice receiving a single dose. Because the AuNPs used in our study have a 5-nm core diameter and a hydrodynamic size of 41 nm for the SMI#9 nanoconjugate, our data suggest that the majority of AuNPs are stripped off their SMI#9 payload rendering them small enough for renal clearance (147). These data are consistent with those reported by Perrault and colleagues who showed rapid clearance of PEGylated 20-nm and 40-nm AuNPs from circulation without accumulation

in the spleen and liver (148). Regardless of the coating layer, nanoparticles always form a “protein corona” when encountering physiologic conditions (153, 154). This corona phenomenon potentially balances out any differences between blank AuNP and SMI#9-conjugated AuNP during circulation and may explain the similar patterns of biodistribution data. It is noteworthy that despite high accumulation of gold in the tumors of blank AuNP-treated mice, tumor growth was unaffected in these mice providing further support for SMI#9 therapeutic activity and the nontoxicity of AuNPs. Although tumor growth was robustly inhibited by SMI#9-AuNP, the treatment did not affect body weights or induce overt toxicity as determined by necropsy and histopathologic analysis of the major vital organs.

#### 4.5 Conclusions

In summary, the mechanistic data presented here show that AuNP is a suitable vehicle for delivering SMI#9 and that the chemically modified SMI#9 released from AuNP functions similarly as the free parent SMI#9. We demonstrated the therapeutic utility of an AuNP-based platform for delivering Rad6 inhibitor for treating *BRCA1* wild-type and *BRCA1*-mutant TNBCs, a breast cancer subtype with poor prognosis and no targeted

therapies. SMI#9 delivery as a prodrug–AuNP conjugate not only improved its pharmacokinetic properties but also allowed for a clinically acceptable (systemic) mode of drug administration that inhibited TNBC growth. There was no evidence of blank or SMI#9-AuNP–induced toxicity as measured by their impact on animal body weight and organ histopathology.

## **CHAPTER 5 SIZE-DEPENDENT TOXICITY OF GOLD NANOPARTICLES**

**This chapter is reproduced with permission from the Small, 12, no. 5 (2016): 631-646. Marie-Claude Senut, Yanhua Zhang, Fangchao Liu, Arko Sen, Douglas M. Ruden, Guangzhao Mao, “Size-dependent toxicity of gold nanoparticles on human embryonic stem cells and their neural derivatives”.**

### 5.1 Introduction

Nanotoxicology is an emerging discipline studying the interference of engineered nanomaterials with the functions of cellular and extracellular nanomachineries.(155) The accelated pace of clinical trials and commercialization of nanomaterials places increased demands on toxicological evaluations of engineered nanomaterials.(156) There is an urgent need to develop predictive and validated nanotoxicological



assessment methods for nanomaterials due to their unique size range, surface chemistry, and interactions with biological systems.(157) Nanomaterials have the potential to cross the placental and the blood-brain barriers(2, 158) or, in a few examples, be transported to the central nervous system (CNS) without crossing the blood-brain barrier.(159-162) Neurotoxicity of engineering nanomaterials will become more relevant with the development of CNS-targeting nanomedicine.

Because of the wide biomedical applications of AuNPs, human exposure to AuNPs will be increasingly likely, which warrants careful evaluation of their toxicological effects. AuNPs have been described by most studies as nontoxic,(139, 163-165) but some studies have found them to be toxic.(166-172) AuNPs with 1.4-1.5 nm in diameter have been found to be highly toxic to cells.(168, 173) A few in vitro and in vivo studies have shown that chronic exposure to AuNPs might interfere with brain function. For example, a decrease in glutamate decarboxylase 1, an enzyme that is involved in GABA synthesis and is associated with several neurological disorders,(174) was observed in human HeLa cells exposed to gold nanorods.(175) Exposure to high concentrations of 20 nm AuNPs was found

to increase the proliferation in human neurosphere-derived neural precursor/pregenerator cells (NPCs)(176) and induce oxidative stress in a mouse immortalized NPC line.(177) In rodent models, intraperitoneal injections of 17-20 nm AuNPs resulted in learning and memory deficits associated with elevated dopamine levels and decreased serotonin levels,(178) as well as increased brain expression levels of markers of oxidative stress, apoptosis, and inflammation.(179) More recently, cultured mouse hippocampal CA1 neurons were shown to be more excitable when exposed to 5-40 nm AuNPs.(180) Taken together, these data demonstrate that AuNPs as tools for neuromedicine should be carefully evaluated since they may adversely alter neuronal differentiation, synapse formation, and functional plasticity (which affect memory and learning) in a size-dependent manner.

Currently, there are no systematic methods to predict toxicological effects of AuNPs on human health. A majority of neurotoxicological assessments are conducted in vitro using immortalized cell lines with standard toxicological assays such as the MTT (measurement of mitochondrial enzymatic activity) and LDH (measurement of cell membrane

disruption) assays with short exposure time (usually limited to within 48 hours). One shortcoming of standard in vitro toxicity assays, however, is that the potential interference of nanoparticles with embryonic development cannot be clearly addressed. Furthermore, it is often difficult to correlate outcomes from animals to humans. Human embryonic stem cells (hESCs)(181) and their subsequent differentiation into NPCs and neurons have enabled researchers to establish pluripotent cell-based models to study developmental neurotoxicology. This process mimics aspects of the early stages of human brain development, giving us a unique opportunity to identify the effects of exposure to nanomaterials on neural specification. Some significant advantages in using hESCs compared to other (e.g., animal-derived) systems are that 1) they have unlimited self-renewal capabilities and can be grown indefinitely in the laboratory; 2) they can differentiate into a variety of specialized cell types, such as neurons; 3) they preclude species-specific differences, making them a better model to predict human response to toxins; and 4) subtle changes in cell functionality rather than cell death can be tested on nanomaterials of low toxicity such as AuNPs. Recently, mouse ESCs were used to evaluate the neurotoxicity of AuNPs.(182, 183)

This chapter describes the morphological and epigenetic effects of AuNPs of three core sizes (1.5 nm, 4.0 nm, and 14 nm) on the neuronal differentiation of hESCs. The 1.5 nm AuNP (AuNP1.5) was chosen because AuNPs of this size have been found to be highly toxic to cells.(168, 173) AuNP4 and AuNP14 are within the size range widely used for targeted drug delivery applications including those targeting the brain.(2, 3) The nanoparticle size and surface chemistry were characterized by UV-vis, AFM, TEM, and zetasizer. We show that AuNPs have size-dependent differential effects on the viability, pluripotency, and neuronal differentiation potentials of hESCs.

## 5.2 Experimental methods

### 5.2.1 Materials

Gold(III) chloride trihydrate ( $\text{HAuCl}_4 \cdot 3\text{H}_2\text{O}$ , 99% metal trace), chloro(triphenylphosphine)gold(I) ( $\text{AuCl}(\text{PPh}_3)$ , 97%), sodium citrate tribasic dehydrate ( $\geq 99\%$ ), MSA (97%), borane tert-butylamine complex (97%), sodium borohydride ( $\text{NaBH}_4$ ) (98%), polyamidoamine (PAMAM, ethylenediamine core) dendrimer G0.5 (powder) and G1.5 (methanol

solution), and bovine serum albumin (BSA, 98%) were all purchased from Sigma-Aldrich. Sodium hydroxide (98%) was purchased from Fisher Scientific.

### 5.2.2 AuNP Synthesis and Characterization

Thiolate-capped 1.5 nm ultrasmall AuNP (AuNP1.5) were synthesized by modifying a literature procedure.<sup>(184)</sup> The Au(I) precursor AuCl(PPh<sub>3</sub>) (0.375 mmol) was partially dissolved in 21 mL ethanol at room temperature under vigorous stirring (600–800 rpm). Tert-butylamine-borane (3.75 mmol) was used as a mild reducing agent, and 2 h after its addition, MSA (0.15 mmol) was added to control the particles size.<sup>(185)</sup> Mercapto-alkyl acids have been found to be effective in stabilizing ultrasmall AuNPs in aqueous solution. The final AuNP ethanol solution was washed and purified by ultracentrifugation using MW10000 Amicon centrifuge tubes in deionized water repeatedly.

MSA-capped 4 nm AuNP (AuNP4) were synthesized following a modified literature procedure.<sup>(16)</sup> A 500 mL aqueous solution containing  $0.25 \times 10^{-3}$  M of HAuCl<sub>4</sub>·3H<sub>2</sub>O and  $0.25 \times 10^{-3}$  M of trisodium citrate was prepared in an Erlenmeyer flask under vigorous stirring at room temperature. Then, 15 mL of ice cold 0.1 M NaBH<sub>4</sub> solution were added to the solution, resulting in a change of the color solution to pink, indicative of the AuNP formation. After

adjusting the pH of the solution to 11 with 0.1 M NaOH solution, 50 mg MSA was added and the solution was stirred for 12 h. The final solution was concentrated to 2.5 g (gold) L<sup>-1</sup> by ultracentrifugation using MW10000 Millipore Amicon centrifuging units and washed by deionized water several times.

Citrate-capped 14 nm AuNP (AuNP14) were synthesized using the Turkevich method.(186, 187) In a typical synthesis, a 500 mL aqueous solution containing 0.25 × 10<sup>-3</sup> M HAuCl<sub>4</sub>·3H<sub>2</sub>O was heated to boil and then 175 mg of sodium citrate dissolved 30 mL water solution was directly poured into the reaction mixture. The color of the reaction turned gray, pink, and finally wine-red. The final solution was concentrated to 2.5 g (gold) L<sup>-1</sup> by ultracentrifugation using MW10000 Millipore Amicon centrifuging units and washed by deionized water several times.

To apply the BSA coating, nanoparticle with concentration of 1 mg (gold) ml<sup>-1</sup> of deionized water was incubated overnight with 400 mg BSA.

Varian Cary 50 UV–vis absorption spectroscopy was used to determine AuNP sizes, based on the Beer–Lambert law, with a scan range of 200–800 nm.

TEM images of AuNPs were taken on JEOL JEM-2010. The samples were prepared by placing a droplet of the AuNP solution on a Formvar-coated copper TEM grid. Excess liquid was removed by a piece of filter paper under the grid and dried in the air. The working voltage was 200 keV and the current was 109 mA. At least 50 particles were measured on the same sample to yield an average particle size.

DLS and zeta potential were measured using a Malvern Nano-ZS. 1 mL solution was transferred to a 2.0 mL polystyrene cuvette. The Z-average hydrodynamic diameter (HD), polydispersity index (PDI), and zeta potential were measured at 25 °C. 15 scans were performed in each measurement.

### 5.2.3 Cell culturing and assay study

Human Embryonic Stem Cell Cultures: The NIH-approved and registered WA09 hESC line (passages 26–32; WiCell Research Institute, Madison, WI, USA)(188) was maintained in a humidified incubator at 37 °C with 5% CO<sub>2</sub> as previously described.(189) Briefly, cells were grown on a feeder layer of irradiated mouse embryonic fibroblasts (GlobalStem, Rockville, MD, USA) in hESC culture medium made of 20% knockout serum replacement,  $2 \times 10^{-3}$  M l-glutamine, 1% nonessential amino acids, 1%

penicillin/streptomycin (all products from Life Technologies Corporation, Carlsbad, CA), 4 ng mL<sup>-1</sup> human fibroblast growth factor basic (FGF2, Peprotech, Rocky Hill, NJ), and 0.1 × 10<sup>-6</sup> M 2-mercaptoethanol (Sigma-Aldrich, St Louis, MO) in DMEM/F12 (Life Technologies Corporation, Carlsbad, CA). The active ingredient within the serum replacement is lipid-rich albumin. hESCs were regularly passaged by mechanical dissection and their pluripotent state assessed by immunofluorescence detection for pluripotency markers, such as Oct4, Nanog, and Lin28.

Trypan Blue Exclusion Assay: At the end of exposure, control and AuNP-treated hESCs were harvested and stained with 0.4% Trypan blue (Life Technologies Corporation, Carlsbad, CA). Viable (unstained) and nonviable (dark-blue stained) cells were counted with a hemocytometer. The number of viable cells was determined by subtracting the number of nonviable cells from the total number of cells counted and expressed as a percentage relative to the total number of cells. Data were collected from three independent experiments.

MTT Assay: hESCs were cultured in phenol red-free culture medium and plated at a density of 100 000 cells per well of a 12-well plate. At the end



of AuNP exposure, the medium was supplemented with  $0.5 \text{ mg mL}^{-1}$  of MTT (Sigma-Aldrich, St Louis, MO) freshly prepared in PBS, and cells were incubated in the dark at  $37 \text{ }^{\circ}\text{C}$  for 3 h. MTT-formazan crystals were then solubilized for 15 min, at room temperature in dimethyl sulfoxide (DMSO). Absorbance was measured at 590 nm using a spectrophotometer, and cell survival was expressed as a percentage of absorbance relative to that of control samples. Data were obtained from three separate experiments.

**Uptakes Studies by TEM:** The cellular uptake of AuNPs was assessed on MEFs and undifferentiated WA09 cells (passage 32) exposed to vehicle or  $10 \text{ } \mu\text{g mL}^{-1}$  AuNP14 for 48 h. At the end of exposure, cells were washed and fixed in 2.5% glutaraldehyde (Electron Microscopy Sciences, Hatfield, PA) in PBS. Samples were processed at the MSU Center for Advanced microscopy where they were postfixed in 1% osmium tetroxide, rinsed in distilled water, dehydrated through a graded series of acetone, and embedded in epoxy resin. Ultrathin 70 nm sections were obtained and then analyzed and photographed using a JEOL 100CXII electron microscope.

**Pluripotency In Vitro Studies:** The effects of exposure to AuNPs on the in vitro pluripotency capabilities of hESCs were determined using

spontaneous differentiation of EBs.(190) Briefly, EBs were generated by mechanical dissociation of hESC colonies and cultured for two weeks in FGF2-free hESC medium in presence of vehicle,  $0.6 \mu\text{g mL}^{-1}$  AuNP1.5, or  $10 \mu\text{g mL}^{-1}$  of AuNP4 and AuNP14. At the end of exposure, total RNA was extracted from EBs using Qiazol (Qiagen, Valencia, CA) according to the manufacturer's protocol, quantified by optical density, and subjected to reverse transcription using Superscript II Reverse Transcriptase and random primers (Life Technologies Corporation, Carlsbad, CA) for 50 min at  $40^\circ\text{C}$  followed by 15 min at  $75^\circ\text{C}$ . Quantitative PCR analyses of the well-established lineage marker genes—endodermal (AFP and NODAL), ectodermal (NCAM and NESTIN), and mesodermal (BRACHYURY, PITX2, and LEFTY)—were performed using an ABI PRISM 7000 Sequence Detection System and its software (Applied Biosystems) with 10 ng cDNA,  $400 \times 10^{-9}$  M of each primers, and SYBR Green PCR Master Mix (Life Technologies Corporation, Carlsbad, CA). Resulting data were normalized against the expression of the internal control GAPDH gene. Data analysis was performed using the  $2^{-\Delta\Delta\text{Ct}}$  method (Livak and Schmittgen 2001) and standardized by log transformation,

mean centering, and autoscaling as previously described.(191) Data were collected from three separate experiments.

Differentiation of hESCs into NPCs: Generation of NPCs from hESCs was performed as previously described.(189, 192) Following mechanical dissociation of hESC colonies, EBs were cultured in suspension for 4 d in 1:1 hESC/N<sub>2</sub> medium (Life Technologies Corporation, Carlsbad, CA), followed by 4 d in N<sub>2</sub> medium supplemented with  $3 \times 10^{-6}$  M retinoic acid (RA; Sigma-Aldrich, St Louis, MO), and 3 d in N<sub>2</sub> medium added with 20 ng mL<sup>-1</sup> FGF2 (Peprotech, Rocky Hill, NJ). At this time, EBs were transferred to fibronectin-coated plates (20 μg mL<sup>-1</sup> fibronectin; Life Technologies Corporation, Carlsbad, CA) and cultured in N<sub>2</sub>/FGF2 medium for an additional 8 d to obtain neural rosettes. The latter were subsequently dissociated and plated in N<sub>2</sub>/FGF2 medium on 10 μg mL<sup>-1</sup> polyornithine/5 μg mL<sup>-1</sup> laminin-coated dishes. Cells were fixed in 4% paraformaldehyde and immunostained for the NPC marker Nestin (mouse anti-Nestin; 1:500; EMD Millipore Corporation, Billerica, MA) and mouse anti-Nestin (1:500, EMD Millipore Corporation, Billerica, MA).

Exposure of hESC-Derived NPCs to AuNPs: hESCs-derived NPCs were cultured on fibronectin-coated six-well dishes in  $N_2$ /FGF2 medium and chronically exposed to vehicle or the different sized AuNPs for 72 h, at which time cells were fixed and immunostained for Nestin and the DNA marker DAPI. The total number of Nestin-positive cells and DAPI-stained nuclei were counted in five fields per well in three separate experiments, by an observer blind to the experimental conditions. The number of cells harboring pyknotic nuclei was also calculated. Total numbers were expressed as a percentage of the total number of cells, as evaluated by DAPI or Hoescht staining.

Neuronal Differentiation of hESC-Derived NPCs: Neuronal differentiation of NPCs derived from control and AuNP-exposed hESCs was achieved as previously described.(189, 193) NPCs were cultured on polyornithine/laminin-coated 12-well dishes at a  $5105 \text{ cells cm}^{-2}$  density in  $N_2$  medium supplemented with  $10 \text{ ng mL}^{-1}$  brain-derived neurotrophic factor (BDNF),  $10 \text{ ng mL}^{-1}$  glial cell-derived neurotrophic factor (GDNF),  $10 \text{ ng mL}^{-1}$  insulin-like growth factor (IGF) (all factors from Peprtech, Rocky Hill, NJ),  $200 \text{ ng mL}^{-1}$  ascorbic acid (Sigma-Aldrich, St Louis, MO), and  $100 \text{ ng mL}^{-1}$  cAMP (Sigma-Aldrich, St Louis, MO). Cells were fixed and stained for the

neuronal marker microtubule-associated protein 2 (MAP2) (mouse antibody; 1:500, EMD Millipore Corporation, Billerica, MA).

Morphological Analysis of MAP2-Positive Cells: Determination of neuritic complexity of MAP2-positive cells derived from control and AuNP-exposed hESCs was performed using Sholl analysis, as previously described.<sup>(189)</sup> Neurons were randomly selected for which neurites could be clearly identified and distinguished from neighboring cells. For each experimental condition, analysis of 18–27 neurons were performed blindly to well treatment. For each neuron examined, the average sum of crossings, the average maximal neuritic distance, and the average total number of branchings were recorded.

Antibodies and Immunofluorescence Procedures: Immunofluorescence staining was performed as previously described.<sup>(194)</sup> Following fixation in 4% paraformaldehyde, cells were rinsed in PBS, blocked in 3% donkey serum (Sigma-Aldrich, St Louis, MO) in 0.3% Triton-X-100 (NDST3%), and incubated overnight at 4 °C with the primary antibodies diluted in NDST1%. After several rinses in NDST1%, cells were incubated for 2 h in the dark with secondary anti-mouse antibodies conjugated to Alexa 488 (1:1000,

Life Technologies Corporation, Carlsbad, CA). Following rinses, cells were stained with the nuclear marker DAPI (Sigma-Aldrich, St Louis, MO). Specificity of the immunostainings was assessed by replacing the primary antibodies with normal serum, and by omitting one immunoreagent of the immunostaining protocol.

**Statistical Analysis:** Statistical significance between experimental groups was determined by Student's *t*-test or one-way analysis of variance (ANOVA) followed by a post hoc Holm–Sidak test when *F* value was significant, or Kruskal–Wallis one-way ANOVA on ranks followed by Dunn's test using the SigmaPlot 12 software (SYSTAT Software Inc., San Jose, CA). Statistical significance was defined at  $p \leq 0.05$ . Data are expressed as the mean  $\pm$  SEM.

**Immunoprecipitation Based Colometric Assays:** Global DNA methylation status of exposed and control hESCs were determined using MethylFlash Methylated DNA Quantification Kit (Catalogue No. P-1034) and MethylFlash Hydroxymethylated DNA Quantification Kit (Catalogue No. P-1036) from Epigentek. Briefly, 200 ng of DNA was bound to the bottom of pretreated wells and 5 hmc DNA was detected using sequential treatment

with capture antibody and detection antibody. The final colorimetric signal was normalized to the standard input DNA to estimate the overall methylation percentage.

## 5.3 Results

### 5.3.1 AuNP characterization

All nanoparticles were synthesized following the methods described previously. The sizes of as synthesized AuNPs were confirmed with TEM and DLS (**Figure 5.1**). The diameters of AuNP core were determined to be  $1.5 \pm 0.1$  nm for AuNP1.5,  $4.2 \pm 0.5$  nm for AuNP4, and  $13.6 \pm 0.4$  nm for AuNP14, respectively (**Figure 5.1 A**). In order to prevent aggregation of AuNPs after addition of culture medium, AuNPs were incubated with bovine serum albumin (BSA) prior to the addition as BSA has been proved to be effective in restraining nanoparticle aggregation.(33, 195) An increase in particle hydrodynamic size of 4-6 nm was observed for AuNP4 and AuNP14 (**Figure 5.1 C**), which indicates the formation of protein corona. The core size of both AuNP4 and AuNP14 remained unchanged according to UV-Vis spectrum, which shows no shift of absorption peak after incubating with BSA. (Results now included here).

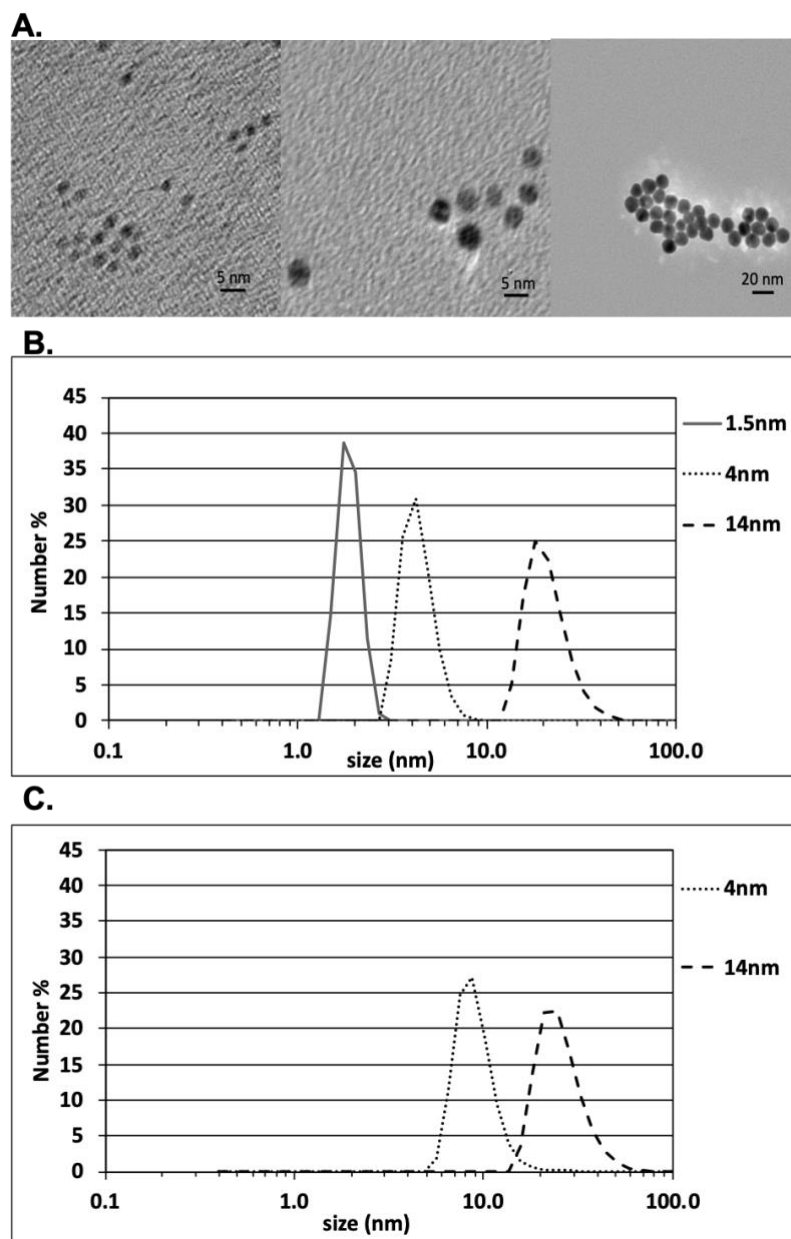


Figure 5-1 A) TEM images of AuNPs of average core diameters 1.5, 4, and 14 nm; B) DLS measurements of AuNP1.5, AuNP4, and AuNP14 in deionized water; and C) AuNP4 and AuNP14 after incubated with BSA in PBS buffer for 24 hours.



### 5.3.2 AuNP size effect on hESC viability

To identify the potential AuNP toxicity, hESC were exposed to  $10 \mu\text{g mL}^{-1}$  AuNPs, largely above the nontoxic range(37) for 24 hours. No remarkable differences in the growth and morphology of hESC colonies were observed with exposure of AuNP4 and AuNP14 at the end of the experiment compared to control cultures. In contrast, cells treated with AuNP1.5 exhibited loss of cohesiveness, rounding up, and detachment, suggesting ongoing cell death, shown as **Figure 5.2 A**. Similar time-course and severity of AuNP1.5-induced cell loss were observed when hESCs were cultured on gelatin-coated plates instead of MEFs, suggesting a direct toxic effect of AuNP1.5 on hESCs (data not shown). Trypan blue assays, which stain dead cells, at the end of the 24 h treatment revealed statistically significant differences in the viability of hESCs between the different experimental groups ( $p < 0.001$ ) (**Figure 5.2 B**). Thus, whereas no change in viability was observed among control, AuNP4- ( $p = 0.79$ ), and AuNP14- ( $p = 0.89$ ) treated cultures, a statistically significant 88% decrease in the number of viable hESCs was observed following treatment with AuNP1.5 ( $p < 0.001$ ). Assessment of hESC viability using the MTT viability assay, a measure of

mitochondrial function, provided comparable results with a statistically significant 85% decrease ( $p= 0.028$ ) in cell viability in AuNP1.5-treated hESCs compared to controls (**Figure 5.2 C**).

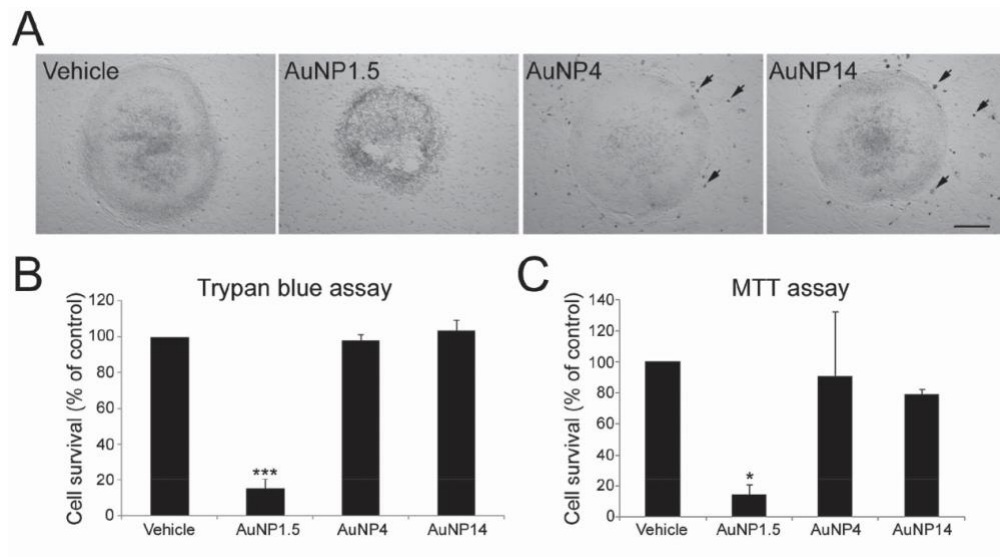


Figure 5-2 Exposure of hESC to AuNPs. A) WA09 hESC cell colonies on MEF feeder layer following 24 h exposure to vehicle, or  $10 \mu\text{g mL}^{-1}$  of AuNP1.5, AuNP4, and AuNP14. Only colonies exposed to AuNP1.5 exhibited altered morphology suggestive of cell death. Arrows indicate MEFs with visible intracellular uptake of AuNPs in the case of AuNP4 and AuNP14. AuNP1.5 was too small to be seen. The scale bar is  $160 \mu\text{m}$  in the bright field microscopic images; B) Cell viability analysis of hESCs exposed for 24 h to  $10 \mu\text{g mL}^{-1}$  of the different sized AuNPs using Trypan blue assay; C) Measurement of mitochondrial activity in hESCs exposed for 24 h to  $10 \mu\text{g mL}^{-1}$  of the different sized AuNPs by the MTT assay.

In order to determine the dosage dependent toxicity of AuNP1.5, hESCs were treated for 4 d with six different sublethal concentrations

ranging from 0.001 to 10  $\mu\text{g mL}^{-1}$ . The Trypan blue exclusion assay revealed an  $\text{IC}_{50}$  value (the concentration necessary to kill 50% of the cells) of 1.45  $\mu\text{g mL}^{-1}$  in this 4 d exposure experiment.

### 5.3.3 AuNP cell uptake by hESC

Cells are known to uptake nanoparticles mainly through endocytosis, and this process is dependent upon the size, shape, and surface chemistry of nanoparticles.(150, 163) As shown in **Figure 5.2 A**, intracellular accumulation of AuNP4 and AuNP14 could clearly be detected by optical microscopy in cultures of hESCs grown on MEFs after a 24 h exposure to 10  $\mu\text{g mL}^{-1}$  concentration. Using DAPI staining to visualize the differences in nuclear chromatin patterns that exist between MEFs and hESCs,(196, 197) we observed that the nuclei of AuNP-positive cells displayed the bright fluorescent heterochromatin foci, characteristic of proliferating and senescent MEFs(197) (**Figure 5.3 A**). In MEFs, AuNPs appeared as black dots that distributed throughout the cellular cytoplasm, preferentially aggregating around the nucleus (**Figure 5.3 B, 5.3 C**). Because no clear uptake of AuNP1.5 could be observed in the cultures, we used the GoldEnhance<sup>TM</sup> (Nanoprobes) amplification method which revealed the presence of labeled

MEFs (**Figure 5.3 D**). In contrast, no accumulation of the AuNP1.5 observed in hESCs, even after the GoldEnhance™ treatment (data not shown). Based on this result, we observed no visible intracellular entry of AuNP1.5 at sublethal dosages.

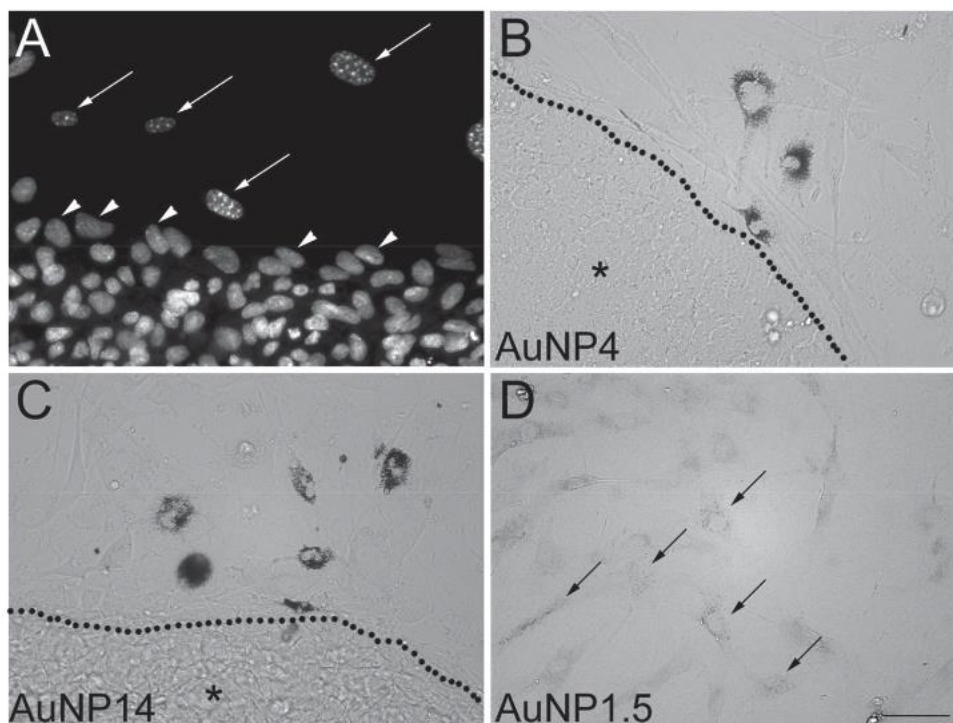


Figure 5-3 Uptake of AuNPs by MEFs but not hESCs. A) Cell cultures stained with the nuclear marker DAPI showing the bright heterochromatin foci characteristic of MEFs (long arrows), which allow to distinguish them from hESCs (arrowheads). Uptake of B) AuNP4 and C) AuNP14 was clearly visible in MEFs, but not in hESC colonies (region marked by \*) delineated by dotted lines. D) Uptake of AuNP1.5 by MEFs was only visible following intensification with GoldEnhance™ (arrows). The scale bar length in (D) valid for (A)–(C) is 50  $\mu\text{m}$ .

#### 5.3.4 AuNP effect on hESC pluripotency and differentiation

The pluripotency of hESCs enables them to differentiate into multiple tissue types. Here we determined the effects of AuNP exposure towards the capabilities of hESCs to generate ectodermal, mesodermal, and endodermal derivatives. To this end, we passively differentiated hESC-derived embryoid bodies (EBs) for 2 weeks in basic fibroblast growth factor (bFGF)-free stem cell medium, while exposing them to either AuNPs or vehicle. The concentration for AuNP4 and AuNP14 was  $10 \mu\text{g mL}^{-1}$  while a sublethal dosage of  $0.6 \mu\text{g mL}^{-1}$  was used for AuNP1.5. As shown in **Figure 5.4**, quantification of marker mRNAs indicated that there were no statistically significant differences in the expression levels of NCAM (**Figure 5.4 A**), NESTIN (**Figure 5.4 B**), BRACHYURY (**Figure 5.4 C**), PITX2 (**Figure 5.4 D**), LEFTY (**Figure 5.4 E**), NODAL (**Figure 5.4 F**) and AFP (**Figure 5.4 G**). These gene expression results suggest that, at the concentrations tested, exposure to AuNPs did not markedly alter the in vitro differentiation potentials of hESCs.

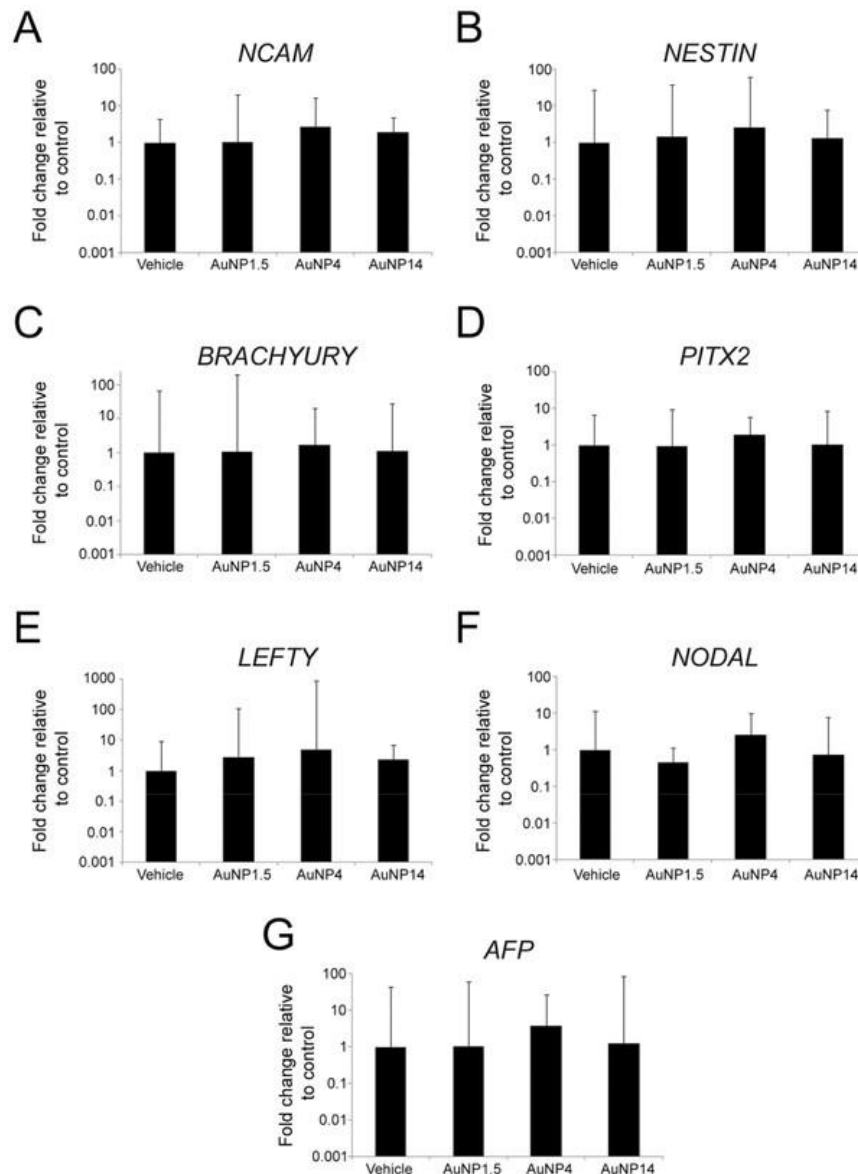


Figure 5- 4 Characterization of the effects that 14 d exposure to AuNP1.5 ( $0.6 \mu\text{g mL}^{-1}$ ), AuNP4 ( $10 \mu\text{g mL}^{-1}$ ), and AuNP14 ( $10 \mu\text{g mL}^{-1}$ ) has on the capability of hESCs to passively differentiate into cells of the three germ layers.

To examine the effects of exposure to various sized AuNP on the neural differentiation of hESCs, we generated EBs and maintained them

throughout the entire neural differentiation protocol (19 days) in presence of vehicle or  $10 \mu\text{g mL}^{-1}$  AuNP1.5, AuNP4, and AuNP14. The presence of AuNP4 and AuNP14 in the medium did not prevent the formation of EBs, which appeared morphologically similar to those generated from vehicle-exposed EBs (**Figure 5.5**). In contrast, AuNP1.5-exposed hESCs did not form EBs but rather rapidly disintegrated into single cells within 48 hours of treatment, so that by day 3, no EBs survived (**Figure 5.5**). Therefore, following experiments were carried out using a  $0.6 \mu\text{g mL}^{-1}$  (EC30) concentration for AuNP1.5, which allowed the formation of EBs. During neural differentiation, both control and AuNP1.5-treated EBs were able to generate neural rosettes (**Figure 5.5**). However, the neural rosettes formed by AuNP1.5-exposed EBs were small, exhibiting a dark aspect (**Figure 5.5**), and did not survive. The data suggest that even at sublethal dosage AuNP1.5 causes adverse effect on neuronal differentiation of hESCs.

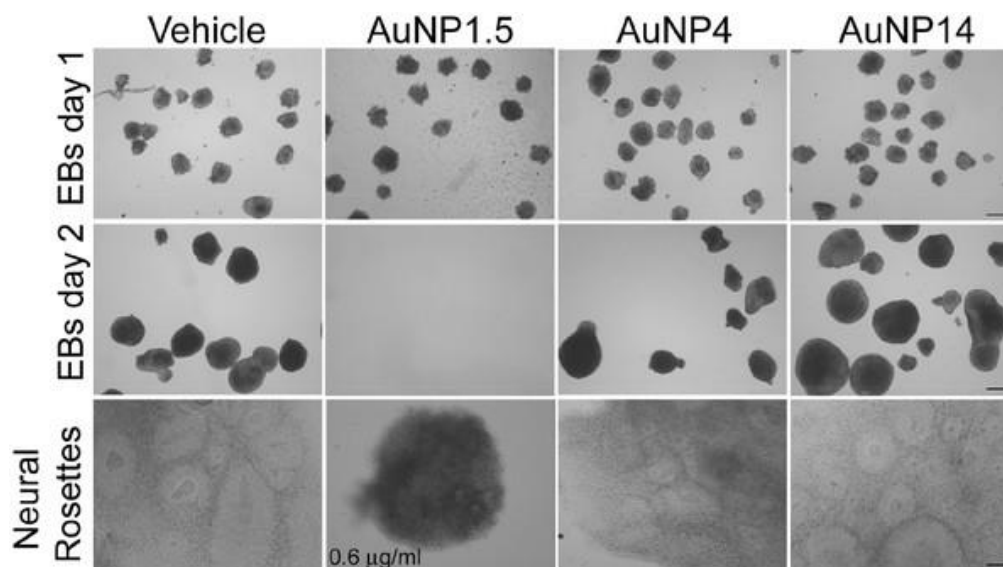


Figure 5 5 Formation of embryoid bodies and neural rosettes by control and AuNP-exposed hESCs.

#### 5.4 Discussions

Our data show that thiolate-capped AuNP4 and citrate-capped AuNP14 are nontoxic to hESCs and do not affect hESC pluripotency or neuronal differentiation into NPCs. Our data also show that thiolate-capped AuNP1.5 is toxic to hESCs with an  $IC_{50}$  value measured during 4-day exposure of  $1.45 \mu\text{g mL}^{-1}$  (or  $0.0706 \mu\text{M}$ ). At first glance, our results appear to be consistent with other reports, in particular, the one on size-dependent cytotoxicity of AuNPs.(198) The paper showed that AuNPs of 15 nm in size are nontoxic while AuNPs of 1-2 nm in size are highly toxic to a variety of cell



lines (SK-Mel-28 human melanoma, HeLa human cervix carcinoma, L929 mouse fibroblasts, and J774A1 mouse macrophages). However, a closer examination points to major differences between the current study and the previous studies. In a previous report, Au<sub>55</sub> cluster with a diameter of 1.4 nm capped by triphenylphosphine monosulfonate (TPPMS), denoted as Au1.4MS, was found highly toxic to a number of human cancer and healthy cell lines.(168) The IC<sub>50</sub> value of Au<sub>55</sub> was determined to be 0.62 μM for fibroblast cells measured at 24 h.(168) Au1.4MS was found to cause necrosis by oxidative stress and mitochondrial damage.(173) A subsequent study showed that when the phosphine ligand was replaced with a thiol ligand, glutathione (GSH), Au<sub>55</sub> cytotoxicity was greatly reduced.(173) The authors attributed the toxicity of Au1.4MS to weak phosphine/metal binding that allows surface gold atoms to interact directly with biological targets. However, in our study, we found that even thiolate-capped Au<sub>55</sub> is toxic to MEFs and hESCs. In addition, the IC<sub>50</sub> of hESCs is much less than the values of fibroblast and cancer cells, which indicates that hESCs are more sensitive to nanoparticle perturbations. The other major finding of this study is that AuNP1.5 imposes adverse effects on hESC survival and neuronal

differentiation without obvious intracellular uptake. This observation argues for the AuNP1.5 interactions with the cell membrane as the cause of its cytotoxicity.

In the literature, several mechanisms of AuNP cytotoxicity have been proposed. One is the size match between Au<sub>55</sub> and the DNA major groove and Au<sub>55</sub> irreversible coordination to DNA.(168) The second is the induction of reactive oxygen species (ROS) formation due to Au<sub>55</sub>'s electronic/catalytic properties (it excites O<sub>2</sub> but is not oxidized itself). Transition metals such as gold are capable of one-electron reduction of oxygen and production of reactive oxygen species such as superoxide radicals, hydrogen peroxide, and hydroxyl radicals, which then can cause oxidation of biomolecules.(199, 200) The third mechanism is Au<sub>55</sub>'s capability to block membrane ion channel.(201) In another study of AuNP surface functionalities on zebrafish embryonic gene expression, 2-mercaptoethanesulfonic acid (MES)-capped 1.5 nm AuNPs were found to affect ion channel transport mechanism signaled by misregulated gene expression.(202) It has been suggested that such gold clusters could be used for cancer treatment if toxicity to normal cells can be

controlled.(155, 203) Our data are more consistent with the third mechanism of AuNP1.5 interfering with membrane ion channel functions.

## 5.5 Conclusions

This work described effect of AuNPs with core size of 1.5, 4, and 14 nm on hESC viability, cell uptake, pluripotency, and differentiations. AuNPs were used as model nanoparticles due to their versatile surface chemistry, ease of imaging, and tunability for targeted drug/imaging agent delivery. We found that hESC colonies exposed to 1.5 nm MSA-capped AuNPs exhibited loss of cohesiveness, rounding up, and detachment suggesting ongoing cell death. The hESCs exposed to 1.5 nm AuNPs did not form EBs but rather rapidly disintegrated into single cells within 48 h of treatment. Cell death caused by 1.5 nm AuNPs also occurred in the treatment with hESC-derived neural precursor/progenitor cells. None of the other nanoparticles exhibited toxicity to the hSECs or their derivatives in experiments lasting as long as 19d. In contrast to some reports, we found that Au<sub>55</sub> capped by the strongly binding thiolate could still be toxic to cells. Our data suggest that hESC uptake of nanoparticles may be different from other cell types as we did not observe

significant amount of AuNPs inside the hESCs while AuNPs were clearly present inside the MEF feeder cells.

## **CHAPTER 6 CONCLUSIONS**

This dissertation described a novel way to achieve targeted delivery of a type of neural therapeutic drug, which could bypass blood-brain barrier, without introducing noticeable side effect. The method is obtained by engineering the surface of gold nanoparticles followed by conjugation with drug and targeting protein. The stability of the nanoconjugates has been characterized, potency was tested on established animal model and recovery was detected. The releasing kinetics was also undergoing further research.

This dissertation also described a nontoxic way to increase solubility and bio-accessibility of anti-cancer drug by conjugating the drug with surface-modified gold nanoparticle. The decrease of tumor size was observed after administration of the nanoconjugate, and the biodistribution study was conducted.

In conclusion, a careful engineering of the gold nanoparticle gives a good opportunity to improve performance of neural therapeutic drugs and anti-cancer drugs after a designed chemical conjugation. Especially given

that gold nanoparticle with size larger than 2 nm in diameter is nontoxic, which is also discussed in this dissertation. The engineering of gold nanoparticle to achieve biocompatible nanoconjugates has a great potential in bio-medical area.

## REFERENCES

1. Dykman L, Khlebtsov N. Gold nanoparticles in biomedical applications: recent advances and perspectives. *Chem Soc Rev.* 2012;41(6):2256-82.
2. Khlebtsov N, Dykman L. Biodistribution and toxicity of engineered gold nanoparticles: a review of in vitro and in vivo studies. *Chemical Society reviews.* 2011;40(3):1647-71.
3. Arvizo RR, Bhattacharyya S, Kudgus RA, Giri K, Bhattacharya R, Mukherjee P. Intrinsic therapeutic applications of noble metal nanoparticles: past, present and future. *Chemical Society reviews.* 2012;41(7):2943-70.
4. Webb JA, Bardhan R. Emerging advances in nanomedicine with engineered gold nanostructures. *Nanoscale.* 2014;6(5):2502-30.
5. Kogan MJ, Bastus NG, Amigo R, Grillo-Bosch D, Araya E, Turiel A, et al. Nanoparticle-mediated local and remote manipulation of protein aggregation. *Nano letters.* 2006;6(1):110-5.
6. Olmedo I, Araya E, Sanz F, Medina E, Arbiol J, Toledo P, et al. How changes in the sequence of the peptide CLPFFD-NH<sub>2</sub> can modify the conjugation and stability of gold nanoparticles and their affinity for beta-amyloid fibrils. *Bioconjugate chemistry.* 2008;19(6):1154-63.

7. Brambilla D, Le Droumaguet B, Nicolas J, Hashemi SH, Wu LP, Moghimi SM, et al. Nanotechnologies for Alzheimer's disease: diagnosis, therapy, and safety issues. *Nanomed-Nanotechnol.* 2011;7(5):521-40.
8. Gao N, Sun HJ, Dong K, Ren JS, Qu XG. Gold-Nanoparticle-Based Multifunctional Amyloid-beta Inhibitor against Alzheimer's Disease. *Chem-Eur J.* 2015;21(2):829-35.
9. Khlebtsov NG. Optics and biophotonics of nanoparticles with a plasmon resonance. *Quantum Electronics.* 2008;38(6):504-29.
10. Faraday M. The Bakerian lecture: experimental relations of gold (and other metals) to light. *Philosophical Transactions of the Royal Society of London.* 1857;147:145-81.
11. Dreaden EC, Alkilany AM, Huang X, Murphy CJ, El-Sayed MA. The golden age: gold nanoparticles for biomedicine. *Chem Soc Rev.* 2012;41(7):2740-79.
12. Baschong W, Lucocq J, Roth J. "Thiocyanate gold": small (2–3 nm) colloidal gold for affinity cytochemical labeling in electron microscopy. *Histochemistry.* 1985;83(5):409-11.
13. Frens G. Controlled nucleation for the regulation of the particle size in monodisperse gold suspensions. *Nature.* 1973;241(105):20-2.
14. Khlebtsov NG, Bogatyrev VA, Dykman LA, Melnikov AG. Spectral extinction of colloidal gold and its biospecific conjugates. *Journal of colloid and interface science.* 1996;180(2):436-45.

15. Turkevich J, Garton G, Stevenson P. The color of colloidal gold. *Journal of colloid Science*. 1954;9:26-35.
16. Jana NR, Gearheart L, Murphy CJ. Wet chemical synthesis of high aspect ratio cylindrical gold nanorods. *The Journal of Physical Chemistry B*. 2001;105(19):4065-7.
17. Nikoobakht B, El-Sayed MA. Preparation and growth mechanism of gold nanorods (NRs) using seed-mediated growth method. *Chemistry of Materials*. 2003;15(10):1957-62.
18. Mukherjee P, Ahmad A, Mandal D, Senapati S, Sainkar SR, Khan MI, et al. Bioreduction of AuCl<sub>4</sub><sup>-</sup> ions by the fungus, *Verticillium* sp. and surface trapping of the gold nanoparticles formed. *Angewandte Chemie International Edition*. 2001;40(19):3585-8.
19. Brust M, Walker M, Bethell D, Schiffrin DJ, Whyman R. Synthesis of thiol-derivatised gold nanoparticles in a two-phase liquid-liquid system. *J Chem Soc, Chem Commun*. 1994(7):801-2.
20. Hou W, Dasog M, Scott RW. Probing the relative stability of thiolate- and dithiolate-protected Au monolayer-protected clusters. *Langmuir*. 2009;25(22):12954-61.
21. Daniel M-C, Astruc D. Gold nanoparticles: assembly, supramolecular chemistry, quantum-size-related properties, and applications toward biology, catalysis, and nanotechnology. *Chemical reviews*. 2004;104(1):293-346.



22. Sapsford KE, Algar WR, Berti L, Gemmill KB, Casey BJ, Oh E, et al. Functionalizing nanoparticles with biological molecules: developing chemistries that facilitate nanotechnology. *Chemical reviews*. 2013;113(3):1904-2074.
23. Baptista P, Pereira E, Eaton P, Doria G, Miranda A, Gomes I, et al. Gold nanoparticles for the development of clinical diagnosis methods. *Analytical and bioanalytical chemistry*. 2008;391(3):943-50.
24. Radwan SH, Azzazy HM. Gold nanoparticles for molecular diagnostics. *Expert review of molecular diagnostics*. 2009;9(5):511-24.
25. Uehara N. Polymer-functionalized gold nanoparticles as versatile sensing materials. *Analytical Sciences*. 2010;26(12):1219-28.
26. Häkkinen H. The gold-sulfur interface at the nanoscale. *Nature chemistry*. 2012;4(6):443-55.
27. Hostetler MJ, Green SJ, Stokes JJ, Murray RW. Monolayers in three dimensions: synthesis and electrochemistry of  $\omega$ -functionalized alkanethiolate-stabilized gold cluster compounds. *Journal of the American Chemical Society*. 1996;118(17):4212-3.
28. Buining PA, Humbel BM, Philipse AP, Verkleij AJ. Preparation of functional silane-stabilized gold colloids in the (sub) nanometer size range. *Langmuir*. 1997;13(15):3921-6.
29. Ingram RS, Hostetler MJ, Murray RW. Poly-hetero- $\omega$ -functionalized alkanethiolate-stabilized gold cluster compounds. *Journal of the American Chemical Society*. 1997;119(39):9175-8.

30. Johnson S, Evans S, Mahon S, Ulman A. Alkanethiol molecules containing an aromatic moiety self-assembled onto gold clusters. *Langmuir*. 1997;13(1):51-7.
31. Chen S, Kimura K. Synthesis and characterization of carboxylate-modified gold nanoparticle powders dispersible in water. *Langmuir*. 1999;15(4):1075-82.
32. Casals E, Pfaller T, Duschl A, Oostingh GJ, Puntès V. Time evolution of the nanoparticle protein corona. *Acs Nano*. 2010;4(7):3623-32.
33. Dominguez-Medina S, Blankenburg J, Olson J, Landes CF, Link S. Adsorption of a Protein Monolayer via Hydrophobic Interactions Prevents Nanoparticle Aggregation under Harsh Environmental Conditions. *ACS Sustainable Chemistry & Engineering*. 2013;1(7):833-42.
34. Alkilany AM, Nagaria PK, Hexel CR, Shaw TJ, Murphy CJ, Wyatt MD. Cellular uptake and cytotoxicity of gold nanorods: molecular origin of cytotoxicity and surface effects. *small*. 2009;5(6):701-8.
35. Haynes B, Zhang Y, Liu F, Li J, Petit S, Kothayer H, et al. Gold nanoparticle conjugated Rad6 inhibitor induces cell death in triple negative breast cancer cells by inducing mitochondrial dysfunction and PARP-1 hyperactivation: Synthesis and characterization. *Nanomedicine: Nanotechnology, Biology and Medicine*. 2015.
36. Senut MC, Zhang Y, Liu F, Sen A, Ruden DM, Mao G. Size-Dependent Toxicity of Gold Nanoparticles on Human Embryonic Stem Cells and Their Neural Derivatives. *Small*. 2015.

37. Khlebtsov N, Dykman L. Biodistribution and toxicity of engineered gold nanoparticles: a review of in vitro and in vivo studies. *Chem Soc Rev.* 2011;40(3):1647-71.
38. Zhu Z-J, Tang R, Yeh Y-C, Miranda OR, Rotello VM, Vachet RW. Determination of the intracellular stability of gold nanoparticle monolayers using mass spectrometry. *Analytical chemistry.* 2012;84(10):4321-6.
39. Demers LM, Mirkin CA, Mucic RC, Reynolds RA, Letsinger RL, Elghanian R, et al. A fluorescence-based method for determining the surface coverage and hybridization efficiency of thiol-capped oligonucleotides bound to gold thin films and nanoparticles. *Analytical chemistry.* 2000;72(22):5535-41.
40. Maeda H. The enhanced permeability and retention (EPR) effect in tumor vasculature: the key role of tumor-selective macromolecular drug targeting. *Advances in Enzyme Regulation.* 2001;41(1):189-207.
41. Kennedy LC, Bickford LR, Lewinski NA, Coughlin AJ, Hu Y, Day ES, et al. A New Era for Cancer Treatment: Gold-Nanoparticle-Mediated Thermal Therapies. *Small.* 2011;7(2):169-83.
42. Minton JP, Moody CD, Dearman JR, McKnight WB, Ketcham AS. An Evaluation of the Physical Response of Malignant Tumor Implants to Pulsed Laser Radiation. *Surg Gynecol Obstet.* 1965;121:538-44.
43. Tuchin VV. Handbook of Photonics for Biomedical Science Preface. *Ser Med Phys Biomed.* 2010:Xix-Xxiii.

44. Lakowicz JR, Ray K, Chowdhury M, Szymanski H, Fu Y, Zhang J, et al. Plasmon-controlled fluorescence: a new paradigm in fluorescence spectroscopy. *Analyst*. 2008;133(10):1308-46.
45. Dykman L, Khlebtsov N. Gold nanoparticles in biomedical applications: recent advances and perspectives. *Chem Soc Rev*. 2012;41(6):2256-82.
46. Page Faulk W, Malcolm Taylor G. Communication to the editors. *Immunochemistry*. 1971;8(11):1081-3.
47. Sokolov K, Follen M, Aaron J, Pavlova I, Malpica A, Lotan R, et al. Real-time vital optical imaging of precancer using anti-epidermal growth factor receptor antibodies conjugated to gold nanoparticles. *Cancer Res*. 2003;63(9):1999-2004.
48. Kho KW, Kah JCY, Lee CGL, Sheppard CJR, Shen ZX, Soo KC, et al. Applications of Gold Nanoparticles in the Early Detection of Cancer. *Journal of Mechanics in Medicine and Biology*. 2007;07(01):19-35.
49. Tsai S-W, Chen Y-Y, Liaw J-W. Compound Cellular Imaging of Laser Scanning Confocal Microscopy by Using Gold Nanoparticles and Dyes. *Sensors*. 2008;8(4):2306-16.
50. Park J, Estrada A, Sharp K, Sang K, Schwartz JA, Smith DK, et al. Two-photon-induced photoluminescence imaging of tumors using near-infrared excited gold nanoshells. *Optics Express*. 2008;16(3).
51. Durr NJ, Larson T, Smith DK, Korgel BA, Sokolov K, Ben-Yakar A. Two-Photon Luminescence Imaging of Cancer Cells Using Molecularly Targeted Gold Nanorods. *Nano Lett*. 2007;7(4):941-5.

52. Wang H, Huff TB, Zweifel DA, He W, Low PS, Wei A, et al. In vitro and in vivo two-photon luminescence imaging of single gold nanorods. *Proceedings of the National Academy of Sciences*. 2005;102(44):15752-6.
53. Hu M, Novo C, Funston A, Wang H, Staleva H, Zou S, et al. Dark-field microscopy studies of single metal nanoparticles: understanding the factors that influence the linewidth of the localized surface plasmon resonance. *Journal of Materials Chemistry*. 2008;18(17).
54. El-Sayed IH, Huang X, El-Sayed MA. Surface Plasmon Resonance Scattering and Absorption of anti-EGFR Antibody Conjugated Gold Nanoparticles in Cancer Diagnostics: Applications in Oral Cancer. *Nano Lett*. 2005;5(5):829-34.
55. Llevot A, Astruc D. Applications of vectorized gold nanoparticles to the diagnosis and therapy of cancer. *Chem Soc Rev*. 2012;41(1):242-57.
56. Miller AD. Human gene therapy comes of age. *Nature*. 1992;357(6378):455-60.
57. Lee J-S, Green JJ, Love KT, Sunshine J, Langer R, Anderson DG. Gold, Poly( $\beta$ -amino ester) Nanoparticles for Small Interfering RNA Delivery. *Nano Lett*. 2009;9(6):2402-6.
58. Noh SM, Kim W-K, Kim SJ, Kim JM, Baek K-H, Oh Y-K. Enhanced cellular delivery and transfection efficiency of plasmid DNA using positively charged biocompatible colloidal gold nanoparticles. *Biochimica et Biophysica Acta (BBA) - General Subjects*. 2007;1770(5):747-52.

59. Oishi M, Nakaogami J, Ishii T, Nagasaki Y. Smart PEGylated Gold Nanoparticles for the Cytoplasmic Delivery of siRNA to Induce Enhanced Gene Silencing. *Chemistry Letters*. 2006;35(9):1046-7.
60. Tsai D-H, DelRio FW, MacCuspie RI, Cho TJ, Zachariah MR, Hackley VA. Competitive Adsorption of Thiolated Polyethylene Glycol and Mercaptopropionic Acid on Gold Nanoparticles Measured by Physical Characterization Methods. *Langmuir*. 2010;26(12):10325-33.
61. Lee H, Choi SH, Park TG. Direct Visualization of Hyaluronic Acid Polymer Chain by Self-Assembled One-Dimensional Array of Gold Nanoparticles. *Macromolecules*. 2006;39(1):23-5.
62. Ruan C, Wang W, Gu B. Surface-enhanced Raman scattering for perchlorate detection using cystamine-modified gold nanoparticles. *Analytica Chimica Acta*. 2006;567(1):114-20.
63. Gao J, Huang X, Liu H, Zan F, Ren J. Colloidal Stability of Gold Nanoparticles Modified with Thiol Compounds: Bioconjugation and Application in Cancer Cell Imaging. *Langmuir*. 2012;28(9):4464-71.
64. Kumar A, Zhang X, Liang X-J. Gold nanoparticles: emerging paradigm for targeted drug delivery system. *Biotechnology advances*. 2013;31(5):593-606.
65. Kogan MJ, Bastus NG, Amigo R, Grillo-Bosch D, Araya E, Turiel A, et al. Nanoparticle-mediated local and remote manipulation of protein aggregation. *Nano Lett*. 2006;6(1):110-5.

66. Olmedo I, Araya E, Sanz F, Medina E, Arbiol J, Toledo P, et al. How changes in the sequence of the peptide CLPFFD-NH<sub>2</sub> can modify the conjugation and stability of gold nanoparticles and their affinity for  $\beta$ -amyloid fibrils. *Bioconjugate chemistry*. 2008;19(6):1154-63.
67. Brambilla D, Le Droumaguet B, Nicolas J, Hashemi SH, Wu L-P, Moghimi SM, et al. Nanotechnologies for Alzheimer's disease: diagnosis, therapy, and safety issues. *Nanomedicine: Nanotechnology, Biology and Medicine*. 2011;7(5):521-40.
68. Andersen ME, Krewski D. The vision of toxicity testing in the 21st century: moving from discussion to action. *Toxicol Sci*. 2010:kfq188.
69. Vanparys P, Corvi R, Aardema MJ, Gribaldo L, Hayashi M, Hoffmann S, et al. Application of in vitro cell transformation assays in regulatory toxicology for pharmaceuticals, chemicals, food products and cosmetics. *Mutation Research/Genetic Toxicology and Environmental Mutagenesis*. 2012;744(1):111-6.
70. Berridge MV, Herst PM, Tan AS. Tetrazolium dyes as tools in cell biology: new insights into their cellular reduction. *Biotechnology annual review*. 2005;11:127-52.
71. Vichai V, Kirtikara K. Sulforhodamine B colorimetric assay for cytotoxicity screening. *Nature protocols*. 2006;1(3):1112-6.
72. Strober W. Trypan blue exclusion test of cell viability. *Current protocols in immunology*. 2001:A3. B. 1-A3. B. .
73. Louis KS, Siegel AC. Cell viability analysis using trypan blue: manual and automated methods. *Mammalian cell viability: methods and protocols*. 2011:7-12.

74. Fotakis G, Timbrell JA. In vitro cytotoxicity assays: comparison of LDH, neutral red, MTT and protein assay in hepatoma cell lines following exposure to cadmium chloride. *Toxicology letters*. 2006;160(2):171-7.
75. Weyermann J, Lochmann D, Zimmer A. A practical note on the use of cytotoxicity assays. *Int J Pharm*. 2005;288(2):369-76.
76. Zanger UM, Schwab M. Cytochrome P450 enzymes in drug metabolism: regulation of gene expression, enzyme activities, and impact of genetic variation. *Pharmacology & therapeutics*. 2013;138(1):103-41.
77. Holliday R. Epigenetics: a historical overview. *Epigenetics*. 2006;1(2):76-80.
78. Amsterdam A, Nissen RM, Sun Z, Swindell EC, Farrington S, Hopkins N. Identification of 315 genes essential for early zebrafish development. *Proceedings of the National Academy of Sciences of the United States of America*. 2004;101(35):12792-7.
79. Goodman CM, McCusker CD, Yilmaz T, Rotello VM. Toxicity of gold nanoparticles functionalized with cationic and anionic side chains. *Bioconjugate chemistry*. 2004;15(4):897-900.
80. Tsoli M, Kuhn H, Brandau W, Esche H, Schmid G. Cellular uptake and toxicity of Au55 clusters. *Small*. 2005;1(8-9):841-4.
81. Pan Y, Leifert A, Ruau D, Neuss S, Bornemann J, Schmid G, et al. Gold nanoparticles of diameter 1.4 nm trigger necrosis by oxidative stress and mitochondrial damage. *Small*. 2009;5(18):2067-76.



82. Pan Y, Neuss S, Leifert A, Fischler M, Wen F, Simon U, et al. Size-dependent cytotoxicity of gold nanoparticles. *Small*. 2007;3(11):1941-9.
83. Pan Y, Leifert A, Graf M, Schiefer F, Thoröe-Boveleth S, Broda J, et al. High-Sensitivity Real-Time Analysis of Nanoparticle Toxicity in Green Fluorescent Protein-Expressing Zebrafish. *Small*. 2013;9(6):863-9.
84. Leifert A, Pan Y, Kinkeldey A, Schiefer F, Setzler J, Scheel O, et al. Differential hERG ion channel activity of ultras-small gold nanoparticles. *Proceedings of the National Academy of Sciences*. 2013;110(20):8004-9.
85. Di Guglielmo C, Lopez DR, De Lapuente J, Mallafre JM, Suarez MB. Embryotoxicity of cobalt ferrite and gold nanoparticles: a first in vitro approach. *Reprod Toxicol*. 2010;30(2):271-6.
86. Campagnolo L, Fenoglio I, Massimiani M, Magrini A, Pietroiusti A. Screening of nanoparticle embryotoxicity using embryonic stem cells. *Methods Mol Biol*. 2013;1058:49-60.
87. Barnes PJ. Theophylline. *Am J Resp Crit Care*. 2013;188(8):901-6.
88. de Boer AG, Gaillard PJ. Drug targeting to the brain. *Annu Rev Pharmacol Toxicol*. 2007;47:323-55.
89. Pardridge WM. The blood-brain barrier: bottleneck in brain drug development. *NeuroRx*. 2005;2(1):3-14.
90. Fabian RH, Coulter JD. Transneuronal transport of lectins. *Brain Res*. 1985;344(1):41-8.

91. Robertson B. Wheat germ agglutinin binding in rat primary sensory neurons: a histochemical study. *Histochemistry*. 1990;94(1):81-5.
92. Gao X, Wu B, Zhang Q, Chen J, Zhu J, Zhang W, et al. Brain delivery of vasoactive intestinal peptide enhanced with the nanoparticles conjugated with wheat germ agglutinin following intranasal administration. *J Control Release*. 2007;121(3):156-67.
93. Thorne RG, Emory CR, Ala TA, Frey WH, 2nd. Quantitative analysis of the olfactory pathway for drug delivery to the brain. *Brain Res*. 1995;692(1-2):278-82.
94. Moreno DE, Yu XJ, Goshgarian HG. Identification of the axon pathways which mediate functional recovery of a paralyzed hemidiaphragm following spinal cord hemisection in the adult rat. *Exp Neurol*. 1992;116(3):219-28.
95. Buttry JL, Goshgarian HG. Injection of WGA-Alexa 488 into the ipsilateral hemidiaphragm of acutely and chronically C2 hemisected rats reveals activity-dependent synaptic plasticity in the respiratory motor pathways. *Exp Neurol*. 2014;261:440-50.
96. Moro S, Gao ZG, Jacobson KA, Spalluto G. Progress in the pursuit of therapeutic adenosine receptor antagonists. *Med Res Rev*. 2006;26(2):131-59.
97. Nantwi KD, El-Bohy A, Goshgarian HG. Actions of systemic theophylline on hemidiaphragmatic recovery in rats following cervical spinal cord hemisection. *Exp Neurol*. 1996;140(1):53-9.

98. Nantwi KD, Goshgarian HG. Actions of specific adenosine receptor A1 and A2 agonists and antagonists in recovery of phrenic motor output following upper cervical spinal cord injury in adult rats. *Clin Exp Pharmacol Physiol*. 2002;29(10):915-23.
99. Barnes PJ. Theophylline. *Am J Respir Crit Care Med*. 2013;188(8):901-6.
100. Tzelepis GE, Bascom AT, Safwan Badr M, Goshgarian HG. Effects of theophylline on pulmonary function in patients with traumatic tetraplegia. *J Spinal Cord Med*. 2006;29(3):227-33.
101. Dreaden EC, Mackey MA, Huang X, Kang B, El-Sayed MA. Beating cancer in multiple ways using nanogold. *Chem Soc Rev*. 2011;40(7):3391-404.
102. Mieszawska AJ, Mulder WJ, Fayad ZA, Cormode DP. Multifunctional gold nanoparticles for diagnosis and therapy of disease. *Mol Pharm*. 2013;10(3):831-47.
103. Zhang Y, Walker JB, Minic Z, Liu F, Goshgarian H, Mao G. Transporter protein and drug-conjugated gold nanoparticles capable of bypassing the blood-brain barrier. *Sci Rep*. 2016;6:25794.
104. Sloan KB, Bodor N. Hydroxymethyl and Acyloxymethyl Prodrugs of Theophylline - Enhanced Delivery of Polar Drugs through Skin. *Int J Pharm*. 1982;12(4):299-313.
105. Neises B, Steglich W. 4-Dialkylaminopyridines as Acylation Catalysts .5. Simple Method for Esterification of Carboxylic-Acids. *Angew Chem Int Edit*. 1978;17(7):522-4.
106. Hermanson GT. *Bioconjugate Techniques*, 2nd Edition. Bioconjugate Techniques, 2nd Edition. 2008:1-1202.

107. Golder FJ, Reier PJ, Davenport PW, Bolser DC. Cervical spinal cord injury alters the pattern of breathing in anesthetized rats. *J Appl Physiol.* 2001;91(6):2451-8.
108. Minic Z, Zhang Y, Mao G, Goshgarian HG. Transporter Protein-Coupled DPCPX Nanoconjugates Induce Diaphragmatic Recovery after SCI by Blocking Adenosine A1 Receptors. *J Neurosci.* 2016;36(12):3441-52.
109. Kajana S, Goshgarian HG. Administration of phosphodiesterase inhibitors and an adenosine A1 receptor antagonist induces phrenic nerve recovery in high cervical spinal cord injured rats. *Experimental Neurology.* 2008;210(2):671-80.
110. Bianchi CP. The Effect of Caffeine on Radiocalcium Movement in Frog Sartorius. *J Gen Physiol.* 1961;44(5):845-58.
111. Creed KE, Ishikawa S, Ito Y. Electrical and mechanical activity recorded from rabbit urinary bladder in response to nerve stimulation. *J Physiol.* 1983;338:149-64.
112. Isaacson A, Sandow A. Quinine and Caffeine Effects on <sup>45</sup>Ca Movements in Frog Sartorius Muscle. *Journal of General Physiology.* 1967;50(8):2109-&.
113. Jones DA, Howell S, Roussos C, Edwards RHT. Low-Frequency Fatigue in Isolated Skeletal-Muscles and the Effects of Methylxanthines. *Clin Sci.* 1982;63(2):161-7.
114. Kentera D, Varagic VM. Effects of Cyclic N-2-O-Dibutyryl-Adenosine 3',5'-Monophosphate, Adrenaline and Aminophylline on Isometric Contractility of Isolated Hemidiaphragm of Rat. *Brit J Pharmacol.* 1975;54(3):375-81.
115. Supinski GS, Deal EC, Kelsen SG. The Effects of Caffeine and Theophylline on Diaphragm Contractility. *Am Rev Respir Dis.* 1984;130(3):429-33.

116. Baker-Herman TL, Mitchell GS. Phrenic long-term facilitation requires spinal serotonin receptor activation and protein synthesis. *J Neurosci.* 2002;22(14):6239-46.
117. Golder FJ, Fuller DD, Davenport PW, Johnson RD, Reier PJ, Bolser DC. Respiratory motor recovery after unilateral spinal cord injury: Eliminating crossed phrenic activity decreases tidal volume and increases contralateral respiratory motor output. *Journal of Neuroscience.* 2003;23(6):2494-501.
118. Lalley PM, Mifflin SW. Opposing effects on the phrenic motor pathway attributed to dopamine-D1 and -D3/D2 receptor activation. *Respir Physiol Neurobiol.* 2012;181(2):183-93.
119. Nantwi KD, Goshgarian HG. Actions of specific adenosine receptor A(1) and A(2) agonists and antagonists in recovery of phrenic motor output following upper cervical spinal cord injury in adult rats. *Clin Exp Pharmacol P.* 2002;29(10):915-23.
120. Wong PT, Choi SK. Mechanisms of drug release in nanotherapeutic delivery systems. *Chem Rev.* 2015;115(9):3388-432.
121. Zong H, Thomas TP, Lee KH, Desai AM, Li MH, Kotlyar A, et al. Bifunctional PAMAM dendrimer conjugates of folic acid and methotrexate with defined ratio. *Biomacromolecules.* 2012;13(4):982-91.
122. Vijayalakshmi N, Ray A, Malugin A, Ghandehari H. Carboxyl-terminated PAMAM-SN38 conjugates: synthesis, characterization, and in vitro evaluation. *Bioconjug Chem.* 2010;21(10):1804-10.

123. Yura H, Yoshimura N, Hamashima T, Akamatsu K, Nishikawa M, Takakura Y, et al. Synthesis and pharmacokinetics of a novel macromolecular prodrug of Tacrolimus (FK506), FK506-dextran conjugate. *J Control Release*. 1999;57(1):87-99.
124. Giroux MC, Helie P, Burns P, Vachon P. Anesthetic and pathological changes following high doses of ketamine and xylazine in Sprague Dawley rats. *Exp Anim Tokyo*. 2015;64(3):253-60.
125. Nantwi KD, Goshgarian HG. Alkylxanthine-induced recovery of respiratory function following cervical spinal cord injury in adult rats. *Exp Neurol*. 2001;168(1):123-34.
126. Duncan R, Gaspar R. Nanomedicine(s) under the Microscope. *Mol Pharmaceut*. 2011;8(6):2101-41.
127. Koken MHM, Smit EME, Jaspers-Dekker I, Oostra BA, Hagemeyer A, Bootsma D, et al. Localization of two human homologs, HHR6A and HHR6B, of the yeast DNA repair gene RAD6 to chromosomes Xq24–q25 and 5q23–q31. *Genomics*. 1992;12(3):447-53.
128. Koken MH, Reynolds P, Jaspers-Dekker I, Prakash L, Prakash S, Bootsma D, et al. Structural and functional conservation of two human homologs of the yeast DNA repair gene RAD6. *Proceedings of the National Academy of Sciences*. 1991;88(20):8865-9.
129. Lawrence CW. Mutagenesis in *Saccharomyces Cerevisiae*. *Advances in Genetics* 1982. p. 173-254.
130. Jentsch S, McGrath JP, Varshavsky A. The yeast DNA repair gene RAD6 encodes a ubiquitin-conjugating enzyme. *Nature*. 1987;329(6135):131-4.

131. Sung P, Prakash S, Prakash L. Stable ester conjugate between the *Saccharomyces cerevisiae* RAD6 protein and ubiquitin has no biological activity. *Journal of Molecular Biology*. 1991;221(3):745-9.
132. Shekhar MP, Lyakhovich A, Visscher DW, Heng H, Kondrat N. Rad6 overexpression induces multinucleation, centrosome amplification, abnormal mitosis, aneuploidy, and transformation. *Cancer Res*. 2002;62(7):2115-24.
133. Shekhar MPV, Biernat LA, Pernick N, Tait L, Abrams J, Visscher DW. Utility of DNA postreplication repair protein Rad6B in neoadjuvant chemotherapy response. *Medical Oncology*. 2009;27(2):466-73.
134. Gerard B, Sanders MA, Visscher DW, Tait L, Shekhar MPV. Lysine 394 is a novel Rad6B-induced ubiquitination site on beta-catenin. *Bba-Mol Cell Res*. 2012;1823(10):1686-96.
135. Lyakhovich A, Shekhar MPV. RAD6B overexpression confers chemoresistance: RAD6 expression during cell cycle and its redistribution to chromatin during DNA damage-induced response. *Oncogene*. 2004;23(17):3097-106.
136. Lyakhovich A, Shekhar MPV. Supramolecular Complex Formation between Rad6 and Proteins of the p53 Pathway during DNA Damage-Induced Response. *Molecular and Cellular Biology*. 2003;23(7):2463-75.
137. Sanders MA, Brahehi G, Nangia-Makker P, Balan V, Morelli M, Kothayer H, et al. Novel Inhibitors of Rad6 Ubiquitin Conjugating Enzyme: Design, Synthesis, Identification, and Functional Characterization. *Molecular Cancer Therapeutics*. 2013;12(4):373-83.

138. Eck W, Craig G, Sigdel A, Ritter G, Old LJ, Tang L, et al. PEGylated Gold Nanoparticles Conjugated to Monoclonal F19 Antibodies as Targeted Labeling Agents for Human Pancreatic Carcinoma Tissue. *ACS Nano*. 2008;2(11):2263-72.
139. Connor EE, Mwamuka J, Gole A, Murphy CJ, Wyatt MD. Gold Nanoparticles Are Taken Up by Human Cells but Do Not Cause Acute Cytotoxicity. *Small*. 2005;1(3):325-7.
140. Klassen NV, Kedrov VV, Ossipyan YA, Shmurak SZ, Shmyt Ko IM, Krivko OA, et al. Nanoscintillators for microscopic diagnostics of biological and medical objects and medical therapy. *IEEE Trans Nanobioscience*. 2009;8(1):20-32.
141. Vigderman L, Zubarev ER. Therapeutic platforms based on gold nanoparticles and their covalent conjugates with drug molecules. *Adv Drug Deliver Rev*. 2013;65(5):663-76.
142. Chavez KJ, Garimella SV, Lipkowitz S. Triple negative breast cancer cell lines: one tool in the search for better treatment of triple negative breast cancer. *Breast Dis*. 2010;32(1-2):35-48.
143. Haynes B, Zhang Y, Liu F, Li J, Petit S, Kothayer H, et al. Gold nanoparticle conjugated Rad6 inhibitor induces cell death in triple negative breast cancer cells by inducing mitochondrial dysfunction and PARP-1 hyperactivation: Synthesis and characterization. *Nanomedicine: Nanotechnology, Biology and Medicine*. 2016;12(3):745-57.



144. Manson J, Kumar D, Meenan BJ, Dixon D. Polyethylene glycol functionalized gold nanoparticles: the influence of capping density on stability in various media. *Gold Bulletin*. 2011;44(2):99-105.
145. De Jong WH, Hagens WI, Krystek P, Burger MC, Sips AJAM, Geertsma RE. Particle size-dependent organ distribution of gold nanoparticles after intravenous administration. *Biomaterials*. 2008;29(12):1912-9.
146. Sadauskas E, Wallin H, Stoltenberg M, Vogel U, Doering P, Larsen A, et al. Kupffer cells are central in the removal of nanoparticles from the organism. *Particle and Fibre Toxicology*. 2007;4(1).
147. Ohlson M, Sörensson J, Haraldsson B. A gel-membrane model of glomerular charge and size selectivity in series. *American Journal of Physiology-Renal Physiology*. 2001;280(3):F396-F405.
148. Perrault SD, Walkey C, Jennings T, Fischer HC, Chan WCW. Mediating Tumor Targeting Efficiency of Nanoparticles Through Design. *Nano Lett*. 2009;9(5):1909-15.
149. Senut M-C, Zhang Y, Liu F, Sen A, Ruden DM, Mao G. Size-Dependent Toxicity of Gold Nanoparticles on Human Embryonic Stem Cells and Their Neural Derivatives. *Small*. 2016;12(5):631-46.
150. Chithrani BD, Ghazani AA, Chan WCW. Determining the Size and Shape Dependence of Gold Nanoparticle Uptake into Mammalian Cells. *Nano Lett*. 2006;6(4):662-8.

151. Sadauskas E, Danscher G, Stoltenberg M, Vogel U, Larsen A, Wallin H. Protracted elimination of gold nanoparticles from mouse liver. *Nanomedicine: Nanotechnology, Biology and Medicine*. 2009;5(2):162-9.
152. Zhang G, Yang Z, Lu W, Zhang R, Huang Q, Tian M, et al. Influence of anchoring ligands and particle size on the colloidal stability and in vivo biodistribution of polyethylene glycol-coated gold nanoparticles in tumor-xenografted mice. *Biomaterials*. 2009;30(10):1928-36.
153. Herrwerth S, Eck W, Reinhardt S, Grunze M. Factors that Determine the Protein Resistance of Oligoether Self-Assembled Monolayers – Internal Hydrophilicity, Terminal Hydrophilicity, and Lateral Packing Density. *Journal of the American Chemical Society*. 2003;125(31):9359-66.
154. Heuberger M, Drobek T, Spencer ND. Interaction Forces and Morphology of a Protein-Resistant Poly(ethylene glycol) Layer. *Biophysical Journal*. 2005;88(1):495-504.
155. Shvedova AA, Kagan VE, Fadeel B. Close Encounters of the Small Kind: Adverse Effects of Man-Made Materials Interfacing with the Nano-Cosmos of Biological Systems. *Annu Rev Pharmacol*. 2010;50:63-88.
156. Xia T, Li N, Nel AE. Potential Health Impact of Nanoparticles. *Annu Rev Publ Health*. 2009;30:137-50.
157. Maynard AD, Aitken RJ, Butz T, Colvin V, Donaldson K, Oberdorster G, et al. Safe handling of nanotechnology. *Nature*. 2006;444(7117):267-9.

158. De Jong WH, Hagens WI, Krystek P, Burger MC, Sips AJ, Geertsma RE. Particle size-dependent organ distribution of gold nanoparticles after intravenous administration. *Biomaterials*. 2008;29(12):1912-9.
159. Oberdorster G, Stone V, Donaldson K. Toxicology of nanoparticles: A historical perspective. *Nanotoxicology*. 2007;1(1):2-25.
160. Oberdorster G, Sharp Z, Atudorei V, Elder A, Gelein R, Kreyling W, et al. Translocation of inhaled ultrafine particles to the brain. *Inhal Toxicol*. 2004;16(6-7):437-45.
161. Adams RJ, Bray D. Rapid-Transport of Foreign Particles Microinjected into Crab Axons. *Nature*. 1983;303(5919):718-20.
162. Katz LC, Burkhalter A, Dreyer WJ. Fluorescent Latex Microspheres as a Retrograde Neuronal Marker for Invivo and Invitro Studies of Visual-Cortex. *Nature*. 1984;310(5977):498-500.
163. Shukla R, Bansal V, Chaudhary M, Basu A, Bhonde RR, Sastry M. Biocompatibility of Gold Nanoparticles and Their Endocytotic Fate Inside the Cellular Compartment: A Microscopic Overview. *Langmuir*. 2005;21(23):10644-54.
164. Rosi NL, Giljohann DA, Thaxton CS, Lytton-Jean AK, Han MS, Mirkin CA. Oligonucleotide-modified gold nanoparticles for intracellular gene regulation. *Science (New York, NY)*. 2006;312(5776):1027-30.

165. Trickler WJ, Lantz SM, Murdock RC, Schrand AM, Robinson BL, Newport GD, et al. Brain microvessel endothelial cells responses to gold nanoparticles: In vitro pro-inflammatory mediators and permeability. *Nanotoxicology*. 2011;5(4):479-92.
166. Goodman CM, McCusker CD, Yilmaz T, Rotello VM. Toxicity of gold nanoparticles functionalized with cationic and anionic side chains. *Bioconjugate chemistry*. 2004;15(4):897-900.
167. Pernodet N, Fang XH, Sun Y, Bakhtina A, Ramakrishnan A, Sokolov J, et al. Adverse effects of citrate/gold nanoparticles on human dermal fibroblasts. *Small* (Weinheim an der Bergstrasse, Germany). 2006;2(6):766-73.
168. Tsoli M, Kuhn H, Brandau W, Esche H, Schmid G. Cellular uptake and toxicity of AU(55) clusters. *Small* (Weinheim an der Bergstrasse, Germany). 2005;1(8-9):841-4.
169. Nelson BC, Petersen EJ, Marquis BJ, Atha DH, Elliott JT, Cleveland D, et al. NIST gold nanoparticle reference materials do not induce oxidative DNA damage. *Nanotoxicology*. 2013;7(1):21-9.
170. Cho WS, Cho MJ, Jeong J, Choi M, Cho HY, Han BS, et al. Acute toxicity and pharmacokinetics of 13 nm-sized PEG-coated gold nanoparticles. *Toxicol Appl Pharm*. 2009;236(1):16-24.
171. Truong L, Saili KS, Miller JM, Hutchison JE, Tanguay RL. Persistent adult zebrafish behavioral deficits results from acute embryonic exposure to gold nanoparticles. *Comp Biochem Phys C*. 2012;155(2):269-74.

172. Kim KT, Zaikova T, Hutchison JE, Tanguay RL. Gold Nanoparticles Disrupt Zebrafish Eye Development and Pigmentation. *Toxicol Sci.* 2013;133(2):275-88.
173. Pan Y, Leifert A, Ruau D, Neuss S, Bornemann J, Schmid G, et al. Gold nanoparticles of diameter 1.4 nm trigger necrosis by oxidative stress and mitochondrial damage. *Small (Weinheim an der Bergstrasse, Germany).* 2009;5(18):2067-76.
174. Hyde TM, Lipska BK, Ali T, Mathew SV, Law AJ, Metitiri OE, et al. Expression of GABA signaling molecules KCC2, NKCC1, and GAD1 in cortical development and schizophrenia. *The Journal of neuroscience : the official journal of the Society for Neuroscience.* 31. United States. p. 11088-95.
175. Hauck TS, Ghazani AA, Chan WC. Assessing the effect of surface chemistry on gold nanorod uptake, toxicity, and gene expression in mammalian cells. *Small (Weinheim an der Bergstrasse, Germany).* 2008;4(1):153-9.
176. Soderstjerna E, Johansson F, Klefbohm B, Englund Johansson U. Gold- and silver nanoparticles affect the growth characteristics of human embryonic neural precursor cells. *PloS one.* 2013;8(3):e58211.
177. Soenen SJ, Manshian B, Montenegro JM, Amin F, Meermann B, Thiron T, et al. Cytotoxic effects of gold nanoparticles: a multiparametric study. *AcS Nano.* 2012;6(7):5767-83.
178. Chen YS, Hung YC, Lin LW, Liao I, Hong MY, Huang GS. Size-dependent impairment of cognition in mice caused by the injection of gold nanoparticles. *Nanotechnology.* 21. England. p. 485102.

179. Siddiqi NJ, Abdelhalim MA, El-Ansary AK, Alhomida AS, Ong WY. Identification of potential biomarkers of gold nanoparticle toxicity in rat brains. *J Neuroinflammation*. 9. England. p. 123.
180. Jung S, Bang M, Kim BS, Lee S, Kotov NA, Kim B, et al. Intracellular Gold Nanoparticles Increase Neuronal Excitability and Aggravate Seizure Activity in the Mouse Brain. *PloS one*. 2014;9(3).
181. Thomson JA, Itskovitz-Eldor J, Shapiro SS, Waknitz MA, Swiergiel JJ, Marshall VS, et al. Embryonic stem cell lines derived from human blastocysts. *Science (New York, NY)*. 1998;282(5391):1145-7.
182. Campagnolo L, Fenoglio I, Massimiani M, Magrini A, Pietroiusti A. Screening of Nanoparticle Embryotoxicity Using Embryonic Stem Cells. *Methods Mol Biol*. 2013;1058:49-60.
183. Di Guglielmo C, Lopez DR, De Lapuente J, Mallafre JML, Suarez MB. Embryotoxicity of cobalt ferrite and gold nanoparticles: A first in vitro approach. *Reprod Toxicol*. 2010;30(2):271-6.
184. Li Y, Liu S, Yao T, Sun Z, Jiang Z, Huang Y, et al. Controllable synthesis of gold nanoparticles with ultrasmall size and high monodispersity via continuous supplement of precursor. *Dalton Trans*. 2012;41(38):11725-30.
185. Woehrle GH, Brown LO, Hutchison JE. Thiol-Functionalized, 1.5-nm Gold Nanoparticles through Ligand Exchange Reactions: Scope and Mechanism of Ligand Exchange. *Journal of the American Chemical Society*. 2005;127(7):2172-83.

186. Turkevich J, Stevenson PC, Hillier J. A Study of the Nucleation and Growth Processes in the Synthesis of Colloidal Gold. *Discuss Faraday Soc.* 1951(11):55-&.
187. Kimling J, Maier M, Okenve B, Kotaidis V, Ballot H, Plech A. Turkevich Method for Gold Nanoparticle Synthesis Revisited. *The Journal of Physical Chemistry B.* 2006;110(32):15700-7.
188. Thomson JA. Embryonic Stem Cell Lines Derived from Human Blastocysts. *Science.* 1998;282(5391):1145-7.
189. Senut MC, Sen A, Cingolani P, Shaik A, Land SJ, Ruden DM. Lead Exposure Disrupts Global DNA Methylation in Human Embryonic Stem Cells and Alters Their Neuronal Differentiation. *Toxicol Sci.* 2014;139(1):142-61.
190. Ross PJ, Suhr ST, Rodriguez RM, Chang E-A, Wang K, Siripattarapivat K, et al. Human-Induced Pluripotent Stem Cells Produced Under Xeno-Free Conditions. *Stem Cells and Development.* 2010;19(8):1221-9.
191. Willems E, Leyns L, Vandesompele J. Standardization of real-time PCR gene expression data from independent biological replicates. *Analytical Biochemistry.* 2008;379(1):127-9.
192. Zhang S-C, Wernig M, Duncan ID, Brüstle O, Thomson JA. In vitro differentiation of transplantable neural precursors from human embryonic stem cells. *Nature Biotechnology.* 2001;19(12):1129-33.

193. Hu B-Y, Zhang S-C. Directed Differentiation of Neural-stem cells and Subtype-Specific Neurons from hESCs. Cellular Programming and Reprogramming. Methods in Molecular Biology 2010. p. 123-37.
194. Senut MC, Suhr ST, Kaspar B, Gage FH. Intraneuronal aggregate formation and cell death after viral expression of expanded polyglutamine tracts in the adult rat brain. J Neurosci. 2000;20(1):219-29.
195. Casals E, Pfaller T, Duschl A, Oostingh GJ, Puntès V. Time evolution of the nanoparticle protein corona. ACS Nano. 2010;4(7):3623-32.
196. Bartova E, Galiova G, Krejci J, Harnicarova A, Strasak L, Kozubek S. Epigenome and Chromatin Structure in Human Embryonic Stem Cells Undergoing Differentiation. Dev Dynam. 2008;237(12):3690-702.
197. Kennedy AL, McBryan T, Enders GH, Johnson FB, Zhang RG, Adams PD. Senescent mouse cells fail to overtly regulate the HIRA histone chaperone and do not form robust Senescence Associated Heterochromatin Foci. Cell Div. 2010;5.
198. Pan Y, Neuss S, Leifert A, Fischler M, Wen F, Simon U, et al. Size-dependent cytotoxicity of gold nanoparticles. Small (Weinheim an der Bergstrasse, Germany). 2007;3(11):1941-9.
199. Mehta R, Templeton DM, O'Brien PJ. Mitochondrial involvement in genetically determined transition metal toxicity II. Copper toxicity. Chem-Biol Interact. 2006;163(1-2):77-85.



200. Huang XP, O'Brien PJ, Templeton DM. Mitochondrial involvement in genetically determined transition metal toxicity I. Iron toxicity. *Chem-Biol Interact.* 2006;163(1-2):68-76.
201. Leifert A, Pan Y, Kinkeldey A, Schiefer F, Setzler J, Scheel O, et al. Differential hERG ion channel activity of ultrasmall gold nanoparticles. *P Natl Acad Sci USA.* 2013;110(20):8004-9.
202. Truong L, Tilton SC, Zaikova T, Richman E, Waters KM, Hutchison JE, et al. Surface functionalities of gold nanoparticles impact embryonic gene expression responses. *Nanotoxicology.* 2013;7(2):192-201.
203. Soenen SJ, Demeester J, De Smedt SC, Braeckmans K. Turning a frown upside down: Exploiting nanoparticle toxicity for anticancer therapy. *Nano Today.* 2013;8(2):121-5.

**ABSTRACT****ENGINEERING OF GOLD NANOPARTICLES FOR TARGETED DRUG DELIVERY**

by

**FANGCHAO LIU****AUGUST 2019****Advisor:** Dr. Guangzhao Mao**Major:** Materials Science and Engineering**Degree:** Doctor of Philosophy

Due to their ease of synthesis, versatile surface chemistry, ease of imaging, and biocompatibility, gold nanoparticles (AuNPs) are employed as drug delivery devices in the treatment of respiratory problems associated with spinal cord injury (SCI). We have developed a method for the synthesis of a tripartite nanoconjugate comprised of an AuNP drug carrier chemically conjugated to a transporter protein (wheat germ agglutinin coupled to horseradish peroxidase or WGA-HRP) and to potent SCI drugs. The therapeutic efficacy and biodistribution were studied in a validated animal model. Our results show that a single administration of the nanoconjugate improved diaphragmatic activity at a much lower dosage than the effective

systemic drug dosage and restored the respiratory drive. The effects lasted for 4 weeks. A biodistribution study using inductively coupled plasma mass spectrometry on the same animal model shows that the nanoconjugate was successful in targeting the respiratory neurons in the medulla by detecting the presence of gold in the medulla and spinal cord. The AuNPs are also applied in triple negative breast cancer treatment. By conjugating the surface modified AuNPs with a non-soluble drug, the solubility has been increased and introduced cancer cell death after administration. The nanoconjugate structure was determined by UV-vis spectroscopy, transmission electron microscopy, dynamic light scattering, thermogravimetric analysis, and mass spectrometry.

## **AUTOBIOGRAPHICAL STATEMENT**

**Fangchao Liu**

### **EDUCATION**

- 2012-2019, Ph.D., Materials Science and Engineering, Wayne State University, Detroit, Michigan, US.
- 2008-2012, B.S., Applied Chemistry, Beijing Institute of Tech, Beijing, China.

### **EXPERIENCE**

- 2012-2019, Graduate Teaching Assistant, Graduate Research Assistant, Wayne State University, Detroit, Michigan, US.